Title
Coevolution of Supermassive Black Holes and Their Host Galaxies

Author
Hiner, Kyle Devon

Publication Date
2012

UNIVERSITY OF CALIFORNIA
RIVERSIDE

Coevolution of Supermassive Black Holes and Their Host Galaxies

A Dissertation submitted in partial satisfaction
of the requirements for the degree of

Doctor of Philosophy

in

Physics

by

Kyle Devon Hiner

September 2012

Dissertation Committee:

Dr. Gabriela Canalizo, Chairperson
Dr. Gillian Wilson
Dr. Bahram Mobasher

The Dissertation of Kyle Devon Hiner is approved:

Committee Chairperson

University of California, Riverside

Acknowledgments

Gracias sobre todo a mi profesora, Gaby, without whom I would have drowned in the deep, menacing sea of graduate school long ago.

I also wish to thank my cohort, for providing camaraderie and inspiration in these onerous times, especially Mariana Lazarova, for blazing the way forward with me one day at a time.

A special thank you goes to Sabrina Cales, for collaboration and companionship, and for being my support in the final weeks of work. :)

Professional thanks go to all the astronomers who taught me along the way, especially Margrethe Wold, Mike Brotherton, and Mark Lacy. I would like to thank the support astronomers and telescope operators at Lick Observatory on Mt. Hamilton, California and the W.M. Keck Observatory in Waimea and on Mauna Kea, Hawaii. Thanks to M. Vestergaard for providing the Fe II template used in this work. Thanks also to J.H. Woo for insightful discussions.

During my time as a graduate student I was often financially supported by my advisor, which freed me from the burden of TA labors. I am eternally grateful for this. The entrance to and exit from graduate school was provided by the UCR Graduate Division, who sponsored me with fellowships during my first and final years of study. I am thankful for the Dean's Dissertation Research Grant, which allowed me to travel to the W.M. Keck Observatory headquarters in Hawaii in order to collect data for my thesis. I also greatly appreciate the financial and logistical assistance provided by the

Dark Cosmology Centre, at the Niels Bohr Institute, University of Copenhagen, which facilitated a research visit and collaboration.

The text of this dissertation, in part, is a reprint of the material as it appears in Hiner et al. (2012b, 2009) by permission of the American Astronomical Society. The co-author Gabriela Canalizo listed in those publications directed and supervised the research which forms the basis for this dissertation. The co-authors Margrethe Wold, Michael S Brotherton, Sabrina L Cales, Mark Lacy, Anna Sajina, Lee Armus, Susan Ridgway, and Lisa Storrie-Lombardi provided technical expertise to the publications.

You are that vast thing that you see far, far off with great telescopes.
Alan Watts

ABSTRACT OF THE DISSERTATION

Coevolution of Supermassive Black Holes and Their Host Galaxies

by

Kyle Devon Hiner

Doctor of Philosophy, Graduate Program in Physics
University of California, Riverside, September 2012
Dr. Gabriela Canalizo, Chairperson

The role of black holes in galaxy evolution has come under intense scrutiny since it was discovered that every galaxy in the local universe contains a supermassive black hole (SMBH) at its nucleus. The existence of scaling relations between the SMBH and its host galaxy show that their presence is not coincidental, but rather that SMBHs and their hosts have a shared evolution. The nature of this coevolution is still debated with some proposing it to be a natural result of hierarchical merging models, while others invoke SMBH feedback mechanisms that couple BH growth with that of the host galaxy. In this dissertation, I examine different regimes of SMBH activity and host galaxy properties. I investigate a sample of post-starburst galaxies to gain insight into the morphological and spectrophotometric evolution of galaxies through galaxy interactions and mergers. I plot detailed comparisons of the galaxy kinematics as measured from different stellar populations. I also investigate post-starburst galaxies that simultaneously host an AGN. I develop a technique to study the properties of both the host galaxy and the SMBH in these objects, directly investigating the scaling relation between the two. I describe analysis performed on red quasars in another study that directly probes the scaling relations in the non-local universe. Lastly, I conduct SED fitting of quasars to illuminate the differences between two major spectral types, and investigate host galaxy properties including star formation. All of these projects focus on the relationship between the SMBH and host galaxy. I show that a range of galaxy interactions can lead to black hole growth and are part of galaxy evolution over cosmic time.

Contents

List of Figures **xii**

List of Tables **xiv**

1 Introduction **1**

- 1.1 Background 1
- 1.2 Breakthroughs 3
- 1.3 Galaxy Evolution and Mergers 5
- 1.4 Outline of the Dissertation 6

2 Kinematics of Stellar Populations in Post-Starburst Galaxies **8**

- 2.1 Introduction 8
- 2.2 Sample and Observations 11
- 2.3 Spectral Fitting 13
  - 2.3.1 Stellar Population Templates 15
  - 2.3.2 Balmer region 16
  - 2.3.3 Mg Ib region 16
  - 2.3.4 Ca Triplet 17
  - 2.3.5 Uncertainties 18
- 2.4 Results 19
  - 2.4.1 Velocity Dispersions 19
  - 2.4.2 Faber-Jackson Relations 29

2.5 A Case Study of $2337-1058$ 36

2.6 Discussion 40

3 Black Hole - Bulge Relationship of Post-Starburst Quasars at $z \sim 0.3$ 46

3.1 Introduction 46

3.2 Sample and Observations 50

3.3 Stellar Velocity Dispersion 55

3.3.1 Fitting Code 55

3.3.2 Templates 56

3.3.3 Fitting Procedure 58

3.4 Black Hole Mass 62

3.4.1 Hα 64

3.4.2 Mg II 66

3.4.3 Continuum Luminosities 70

3.5 Results 73

3.5.1 The $\mathrm{M_{BH}} - \sigma_*$ Relation 74

3.5.2 The $\mathrm{M_{BH}}-\mathrm{L_{bulge}}$ Relation 79

3.5.3 The Faber-Jackson Relation 82

3.6 Discussion 86

4 Red Quasars 91

4.1 Introduction 91

4.2 Measuring the FWHM$_{H\alpha}$ 93

4.3 Galaxy Morphologies 95

4.4 Discussion 99

5 An Infrared Comparison of Type-1 and Type-2 Quasars 105

5.1 Introduction 105

5.2 Sample Selection 108

5.3 Observations and Data Reduction 109

5.3.1 Photometry 110

5.3.2 Spectra 111

5.4 Analysis and Results 114

5.4.1 Modeling 114

5.4.2 Star Formation Rates 121

5.5 Summary and Discussion 126

6 Conclusions **131**

Appendix A Spectra of post-starburst quasars at $z \sim 0.3$ **143**

Appendix B Spectra of red quasars at $z > 0.4$ **145**

List of Figures

2.1 Images of the post-starburst galaxy sample 14

2.2 Spectral fitting of the Balmer region 22

2.3 Spectral fitting of the Mg Ib region 22

2.4 Spectral fitting of the Ca T region 23

2.5 Fitted components a 24

2.6 Fitted components b 25

2.7 Fitted components c 26

2.8 Velocity dispersion comparison Balmer region 30

2.9 Velocity dispersion comparison Balmer region population templates and K+A stars 30

2.10 Velocity dispersion comparison Mg Ib region 30

2.11 Velocity dispersion comparison Mg Ib region population templates and K+A stars 31

2.12 Velocity dispersion comparison Balmer region with Mg Ib region 31

2.13 Faber-Jackson relation M_g 37

2.14 Faber-Jackson relation M_r 37

2.15 Faber-Jackson relation young components 38

2.16 Faber-Jackson relation old components 38

2.17 Internal kinematics of $2337-1058$ 41

3.1 HST images of PSQs 60

3.2 Spectral fitting results for PSQs 61

3.3 Mg Ib region 63

3.4 Hα region decomposition 67

3.5 Mg II region Fe template fitting 71

3.6 $\mathrm{M_{BH}} - \sigma_*$ relation 77

3.7 $\mathrm{M_{BH}} - \sigma_*$ offset dependence with redshift 80

3.8 $\mathrm{M_{BH}} - \mathrm{L_{bulge}}$relation 83

3.9 Faber-Jackson relation with PSQs 90

4.1 Red quasar Hα measurements 96

4.2 Image deconvolution of red quasars A 100

4.3 Image deconvolution of red quasars B 101

4.4 Image deconvolution of red quasars C 102

5.1 *Spitzer* IRS spectra 113

5.2 SEDs of type-1 quasars 117

5.3 SEDs of type-2 quasars 118

5.4 Average AGN SED comparison 120

5.5 Integrated PAH luminosity vs. far-IR luminosity 123

A.1 LRIS Spectra of PSQs 144

B.1 LRIS spectra of red quasars 146

List of Tables

2.1 Observations 14
2.2 Template Proportions 20
2.3 Velocity Dispersions 21
2.4 K+A tests 21
2.5 Kinematics of $2337-1058$ 45

3.1 Observations 52
3.2 Template Stars 54
3.3 Best Fit Parameters 60
3.4 Line Widths and Monochromatic Luminosities 75
3.5 Black Hole Masses 75

4.1 Red quasar Hα measurements 102
4.2 Results of Modeling the QSO Host Galaxies Using GALFIT 103

5.1 Targets and their Fluxes in mJy 113
5.2 Additional Photometry Used in Modeling Procedure 122
5.3 Luminosities and Star Formation Rates 127

Chapter 1

Introduction

1.1. Background

The study of Active Galactic Nuclei (AGN) has a long and interesting history dating back to the 1940s when Carl Seyfert reported on nuclear emission in six spiral galaxies (Seyfert 1943). Developments in the field were slow coming until others began reporting optical counterparts to radio sources (*e.g.,* Matthews & Sandage 1963; Schmidt 1963; Sandage & Wyndham 1965). Because the objects were bright in the radio, but appeared as point-sources in the optical, they became known as quasi-stellar radio sources (quasars). Spectroscopy of the sources (*e.g.,* Schmidt 1963) indicated that the quasars were at cosmological distances. If true, the intrinsic luminosities were shown to be astoundingly large. However, many objects exhibited spectra that were similar to quasars in the optical, but were radio quiet, prompting Sandage (1965) to declare "quasi-stellar galaxies" a "major new constituent of the universe". Sandage estimated the space density of quasi-stellar galaxies to be rare compared to normal galaxies, but approximately 500 times more numerous than the radio loud population.

The discovery of quasi-stellar sources refocused attention on other galaxies with nuclei that behaved strangely, including the population of Seyfert galaxies. The AGN umbrella grew to encompass a great many types of galaxies. The taxonomy of AGN became quite convoluted, with classifications of galaxies depending on morphology, radio loudness, and optical spectral type. The luminosity criterion divides objects into low-luminosity "Seyferts" and higher luminosity quasars or quasi-stellar objects (QSOs). Though QSOs often appear point-like in shallow exposures, deep images can reveal their host galaxies. The term quasar is now commonly used to refer to high luminosity sources despite its origins to describe radio loudness.

AGN are roughly divided into two spectral types regardless of their luminosity. The main features of the spectra include the continuum, narrow emission lines, and broad emission lines. Objects that exhibit all three of these features are known as type-1 AGN. The continuum of a type-1 AGN is typically blue with spectral slope $\alpha_\nu \approx -0.5$ (Richards et al. 2006; Vanden Berk et al. 2001) where $f_\nu \propto \nu^\alpha$; note also $f_\lambda \propto c^{\alpha+1}/\lambda^{\alpha-2}$. Narrow emission lines appear in high ionization forbidden transitions such as [O II] λ3727, [O III] λ5007, [N II] $\lambda\lambda$ 6548, 6583, and [S II] $\lambda\lambda$ 6716, 6730. The emission line ratios are different from those of star forming regions and can be used to distinguish AGN from star forming galaxies (Baldwin et al. 1981). Broad emission lines appear in low ionization species, most prominently the Balmer series, Mg II $\lambda\lambda 2796, 2802$, C III, C IV, and Ly$\alpha$. The broad emission lines can have widths on the order of thousands of km s^{-1}, indicating very high velocities. Type-2 AGN show the narrow lines with similar ratios as the type-1 objects, but the continuum and broad emission lines are not present in the spectra. Other, more peculiar objects, such as blazars, broad absorption line (BAL) quasars, and ULRIGs, are also included in the AGN zoo.

1.2. Breakthroughs

Among the many developments in the study of AGN phenomena, there are three major breakthroughs. First and foremost is the determination of the power source of the AGN phenomena. The spectra of AGN show variability on timescales that are proportional to the object luminosity. Reverberation mapping (Blandford & McKee 1982) is a technique used to determine a physical link between the continuum source and the broad-line-emitting gas. The technique essentially relies on the delay between fluctuations in continuum and emission line luminosities. The time delay is interpreted as the light crossing time between continuum ionizing source and the clouds being ionized. It is then possible to determine a characteristic size of the broad line region (BLR). This information, combined with the velocities of the broad line gas, implies that the central source is extraordinarily massive and compact. The power source behind galactic nuclear activity is a supermassive black hole (SMBH).

The second major breakthrough is the development of a physical model that explains the various types of AGN (Antonucci 1993; Sanders et al. 1988). The key piece of evidence that unites type-1 and type-2 AGN is the existence of polarized broad emission lines in type-2 AGN (*e.g.,* Antonucci & Miller 1985). The hidden broad lines are viewed from light scattered off free electrons or small dust grains that surround the nucleus, a mechanism that naturally polarizes the light. Maps of polarized light show a structure that points to the nucleus as the location of the continuum source, consistent with a single AGN. The physical interpretation of polarized broad lines is that the type-2 AGN contains a type-1 AGN within, but that the continuum and broad lines are obscured by some optically thick column along our line of sight. It is posited that along another line of sight, the type-2 would appear as a type-1, exhibiting the signature strong blue continuum and broad emission lines. The unification models invoked either geometric effects of dusty tori surrounding the AGN, or evolutionary effects of dusty cocoons that are shed over time transforming a type-2 into a type-1 AGN.

A third major breakthrough in the study of AGN is the realization that all galaxies in the universe, active and quiescent, contain a supermassive black hole at the nucleus (Magorrian et al. 1998). The findings by Magorrian *et al.* suggest the SMBH is proportional to that of the host, $\mathrm{M_{BH}} \approx 0.006\mathrm{M_{bulge}}$. Since then this relationship has been described as a power-law (*e.g.,* Häring & Rix 2004). Not long after, Ferrarese & Merritt (2000) and Gebhardt et al. (2000) each showed that the mass of the central black hole is correlated with the velocity dispersion of the host galaxy. Furthermore, the scatter in this relationship is small (~ 0.3 dex, but since revised upward). Not only does there exist a supermassive black hole at the center of any given galaxy, but its mass is predicted by the properties of the host galaxy. This result is most interesting, because the host galaxy is orders of magnitude larger in size than the sphere of influence of the SMBH. It implies that the galaxy and BH have had a shared history, and that there exists some mechanism of BH-galaxy evolution that determines both the host properties and the BH mass.

1.3. Galaxy Evolution and Mergers

A longstanding question in extragalactic astronomy has been if and how galaxies move along the Hubble morphological classification sequence (E - S0 - S/SB). Early type galaxies appear elliptical in shape, are gas-poor, and have little, if any star formation. The later type galaxies divide into two branches of spiral galaxies with and without bars and with varying bulge to disk ratios. Spiral galaxies tend to have ongoing star formation and high gas masses. It is difficult to reconcile these differences in stellar populations and gas fractions under the hypothesis that galaxies evolve from early types (ellipticals) to late-types (spirals) through some monolithic collapse mechanism. Confounding the Hubble sequence are the pesky irregular galaxies that defy morphological classification.

Post-starburst galaxies are interesting cases where star formation occurred on a massive scale and was quickly suppressed. This is indicated in the spectra by the presence of early spectral types (A and F stars), but little or no ongoing star formation as measured by the [O II] $\lambda3727$ and/or Hα emission lines (Dressler & Gunn 1983; Zabludoff et al. 1996; Balogh et al. 2005; Goto 2007). Initial investigations into the "E+A" galaxies were intended to determine if the elliptical and disk galaxies shared an evolutionary connection. Could gas-rich disk galaxies evolve into gas-poor passively evolving ellipticals? Disturbed morphologies including tidal tails in E+As found by Zabludoff et al. (1996) were consistent with simulations of merging disk galaxies (*e.g.,* Toomre & Toomre 1972). The presence of early type stars in E+A galaxies, combined with a lack of current star formation, indicated that these galaxies underwent a strong phase of star formation within the last ~ 1 Gyr.

The possibility of galaxy mergers as a mechanism for galaxy evolution between morphological types is also a possibility for fueling AGN and connecting the central SMBH with its host. Stockton (1982) suggested that galaxy mergers could funnel gas and dust to the nucleus after associating companion objects with QSOs. This has largely been accepted as a mechanism for fueling AGN through the work of simulations (*e.g.,* Di Matteo et al. 2005; Hopkins & Quataert 2010), and observations (*e.g.,* Canalizo & Stockton 2001; Bennert et al. 2008). Galaxy mergers could on their own produce a mechanism for establishing the local BH-host galaxy scaling relations (*e.g.,* $\mathrm{M}_{\mathrm{BH}} - \sigma_*$).

1.4. Outline of the Dissertation

In this dissertation I will show aspects of BH-host galaxy co-evolution. It is becoming more clear that the two are intrinsically linked over cosmic time. I will show work from four regimes: post-starburst galaxies, post-starburst quasars, dust-reddened quasars, and high luminosity quasars.

I will begin by describing work on post-starburst galaxies. I will compare velocity dispersions measured from different populations in the galaxy. I will also compare results determined by using a population model or K and A star average spectra.

I will then discuss a unique set of objects that may bridge the gap between active and quiescent galaxies. Post-starburst quasars (PSQs) show both active nucleus features, and a post-starburst stellar population. This combination of features makes them useful for the study of the $\mathrm{M_{BH}} - \sigma_*$ relation in the non-local universe. I will show that these galaxies may fall above the locally-defined relation, with caveats.

I will then discuss quasars that have a slightly obscured nucleus. The obscuration is enough to redden the active nucleus at wavelengths near $\lesssim 5500$ Å. However, the Hα broad line is still observable in these objects. I will discuss how this allows us to measure both host galaxy stellar velocity dispersions (σ_*) and black hole masses ($\mathrm{M_{BH}}$) from single-epoch spectra of these sources.

Lastly, I will discuss a comparison of type-1 and type-2 quasar spectral energy distributions (SEDs). This comparison looks for differences between high-luminosity objects that might indicate an evolutionary sequence between the types of quasars.

The chapters of this dissertation have or will appear in the Astrophysical Journal. Chapter 2 will be submitted presently. Chapter 3 has been accepted (Hiner et al. 2012b), and chapter 5 has previously been published in ApJ (Hiner et al. 2009). Much of chapter 4 has been included in a paper submitted to ApJ (Canalizo et al. 2012). Each of the chapters have a section introducing the specific material in regards to that chapter's contents. The final chapter of the dissertation summarizes the major results.

Chapter 2

Kinematics of Stellar Populations in Post-Starburst Galaxies

2.1. Introduction

Post-starburst galaxies (also known as “E+A” or “K+A” galaxies) have been an interesting case since their discovery by Dressler & Gunn (1983). The physical interpretation of these systems that has emerged since then invokes a scenario where two or more progenitor galaxies have interacted or merged. This merger triggers a large burst of star formation which was extinguished within the last < 1 Gyr.

Evidence for the merger-driven origin of post-starbursts has grown steadily over the years. Zabludoff et al. (1996) found tidal features in the morphologies of post-starburst galaxies in the field consistent with galaxy merger simulations (*e.g.,* Toomre & Toomre 1972), establishing that the post-starburst phenomenon was not limited to cluster environments or cluster-specific mechanisms. Several studies have shown that the young population of post-starburst galaxies is centrally concentrated (Swinbank et al. 2012; Yang et al. 2006; Norton et al. 2001), which would naturally arise from a merger scenario where dissipative star-forming gas is driven deep into the potential well. However, there appears to be a large diversity of post-starburst galaxies, with some merger remnants transforming to early type ellipticals, but others remaining in an S0 morphology.

Bekki et al. (2005) combine numerical simulations with stellar population synthesis code in simulations of merging galaxies to study post-starburst galaxies. They found that a range of galaxy interactions can produce spectra consistent with post-starburst galaxies. Furthermore, the initial parameters of the interactions tend to have an effect on the resulting kinematics. Bekki *et al.* predict that post-starbursts in elliptical galaxies are likely to have young populations that are more strongly rotating and have lower central velocity dispersions than the respective older population.

One open question regarding the origin and evolution post-starburst galaxies is the role of feedback processes. Something must shut down the star formation on a relatively fast timescale, because we see no ongoing star formation. Such a cessation could be caused by supernova or AGN driven winds. Some post-starburst galaxies have been connected with AGN (Brotherton et al. 1999; Goto 2006; Cales et al. 2011), and could prove to be an important link in the coevolution of black holes and their hosts. AGN feedback is an attractive solution for the quenching of star formation in these systems, as it might also provide a physical mechanism for the establishment of BH-host galaxy scaling relations (Ferrarese & Merritt 2000; Gebhardt et al. 2000; Häring & Rix 2004). However, so far only little evidence has been provided in support of this scenario (Tremonti et al. 2007; Cano-Díaz et al. 2012).

Hiner et al. (2012b) have measured stellar velocity dispersions, σ_*, and black hole masses in "post-starburst quasars" (Brotherton et al. 2012, in preparation). They investigate the $\mathrm{M}_{\mathrm{BH}} - \sigma_*$, $\mathrm{M}_{\mathrm{BH}}{-}\mathrm{L}_{\mathrm{bulge}}$, and Faber-Jackson relations using these objects and found that some of the systems could be dynamically peculiar. Several of the objects showed some offset from the Faber-Jackson relation. This is consistent with findings by other authors who place quiescent post-starburst galaxies on the Faber-Jackson relation (Swinbank et al. 2012; Norton et al. 2001). However, it is unclear what drives any observed offset. While Norton et al. (2001) found no significant correlation between the host luminosity and the young population σ_*, the older population was correlated with host luminosity but offset from the Faber-Jackson relation.

The main purpose of this paper is to demonstrate if and how post-starburst populations can be distinguished and if they share similar kinematics. The results can help contextualize studies of post-starbursts that also host AGN. We investigate three separate spectral regions that are typically used to measure stellar velocity dispersions: the Balmer region (including the Balmer series, Ca H+K lines, and the G band), the Mg Ib region (including Hβ), and the Ca Triplet region. In the Balmer region and the Mg Ib region, we model the young and old populations with separate templates.

In the following section we describe our sample and data reduction. In Section 2.3 we describe the direct fitting method used on the three spectral regions. In Section

2.4 we describe the results, comparing the velocity dispersions as measured by different spectral regions and by different population templates. We also investigate the location of the objects in the σ_*-luminosity plane to see if they conform to the Faber-Jackson relation. In Section 2.5 we present a case study of the internal kinematics of one object in our sample that we observed with the longslit along the major axis of the galaxy. Finally, we discuss our results in Section 2.6.

2.2. Sample and Observations

The catalogue of post-starburst galaxies presented by Goto contains 564 local galaxies selected from the SDSS DR5 (Adelman-McCarthy et al. 2007) with the following criteria: Hδ EW > 5 Å, Hα EW < -3.0 Å, and [OII] EW < -2.5 Å. We observed nine objects from the catalogue along with several stars (to form host galaxy templates) with the Low Resolution Imaging Spectrograph (LRIS) on Keck 1 during the night of 25 September 2011. Weather conditions were excellent and seeing was $\sim 0.6\,''$. Table 2.1 shows the objects' redshifts, SDSS g band magnitudes, position angles of the slit during the observation, and the aperture extraction widths. Figure 2.1 shows the SDSS g band image of each object with the slit position angle over-plotted and slit width equal to $1''$.

We reduced the data using standard procedures in IRAF. Bias levels and structure were subtracted using the overscan region. Flat field frames were observed using internal halogen lamps. We removed cosmic rays from the 2D spectra using the L.A. Cosmic routine van Dokkum (2001). We derived a wavelength solution using Hg, Ne, Cd, Ar, and Zn arc lamps. The dichroic of LRIS cuts off at wavelength 5600 Å. Because of the redshift of the observed galaxies, the fitted Mg Ib region (rest frame $4600 - 5600$ Å) was divided between the blue and red side chips. However, the Mg Ib region of the template stars at redshift zero fell solely on the blue side of the instrument. Wavelength calibration errors in the Mg Ib region between the template stars and the galaxies were corrected in the fitting routine using a low-order Legendre polynomial.

Noise in the images is dominated by the sky level. We measured the sky level from the wavelength calibrated 2-D frames and assumed Poisson statistics for the generated noise. These measurements were consistent with the RMS measured from the sky-subtracted frames. The spectra we obtained have signal-to-noise ranging from 50 - 300, depending on the individual object's brightness and exposure time.

After removal of background sky levels, we extracted spectra of the central components of the galaxy using aperture sizes set to the de Vaucouleurs radius as measured by the SDSS DR8 (Aihara et al. 2011). In all cases, the SDSS DR8 reports that de Vaucouleurs profiles were better fits than the exponential profiles, indicating that the bulge component of the post-starburst galaxies is dominant over any potential disk component. Furthermore, all objects have sizes larger than our seeing limit.

We performed flux calibration using four spectrophotometric standards observed throughout the night. Galactic extinction was minimal. Nevertheless, we corrected for it using the maps of Schlegel et al. (1998) and the extinction function of Cardelli et al. (1989).

We ensured the blue and red side spectra were on the same resolution by broadening the red side spectra with a Gaussian until it matched the lower resolution of the blue side spectrum. This was only necessary for fitting the Mg Ib region (4600 – 5600 Å), which is split between the blue and red side spectrographs. The Ca triplet region is covered by the red side spectrograph for both the template stars and the galaxies. Thus, there was no need to match the resolution of these spectra to that of the blue side.

2.3. Spectral Fitting

The direct fitting method has been used extensively in the past (*e.g.,* Barth et al. 2002). We previously employed the method to measure the velocity dispersions of post-starburst galaxies hosting AGN (Hiner et al. 2012b).

The post-starburst galaxies that we are examining here do not contain an active nucleus, so we exclude a contribution from a featureless continuum. Further, we are interested in the line-of-sight velocities (line centroids) and velocity dispersions (second moment) of two individual stellar populations. Our overall model is composed of two templates that are each allotted a unique velocity offset and velocity dispersion. The velocity dispersion is modeled through a convolution of the template with a Gaussian. We sum the two broadened templates and multiply the result with a low-order Legendre polynomial as follows:

$$M(x) = [T^y(x) \otimes G^y(x) + T^o(x) \otimes G^o(x)] \times P(x) \tag{2.1}$$

where the superscripts y and o delineate the “young” and “old” templates, respectively, and $x = log(\lambda)$. The low-order Legendre polynomial accounts for differences between

Table 2.1: Observations

N	RA	DEC	z	r [mag]	exptime (s)	PA (deg)	aperture ($''$)
1	011942.10	+010750.8	0.0899	17.30	600	17	1.95
2	022427.02	−093739.1	0.0883	17.69	600	-9	0.83
3	030319.22	−083619.0	0.0757	17.63	600	-21	1.57
4	032801.61	+004502.0	0.2020	18.46	600	-35	1.98
5	204132.52	−051334.0	0.0621	17.43	1200	-22	1.48
6	210258.78	+103259.8	0.0928	16.12	1200	115	4.75
7	230743.41	+152558.1	0.0697	17.44	1200	-72	2.13
8	232806.02	+144625.2	0.0690	17.87	1200	-69	3.55
9	233712.71	−105800.3	0.0783	16.01	1200	39	6.82

Note. — We observed nine post-starburst galaxies from the sample of Goto (2007) on the night of 25 September 2011 using LRIS on Keck 1. Objects that were observed for 1200 seconds on the blue side had two exposures on the red side to capture two spectral regions for 600 seconds each.

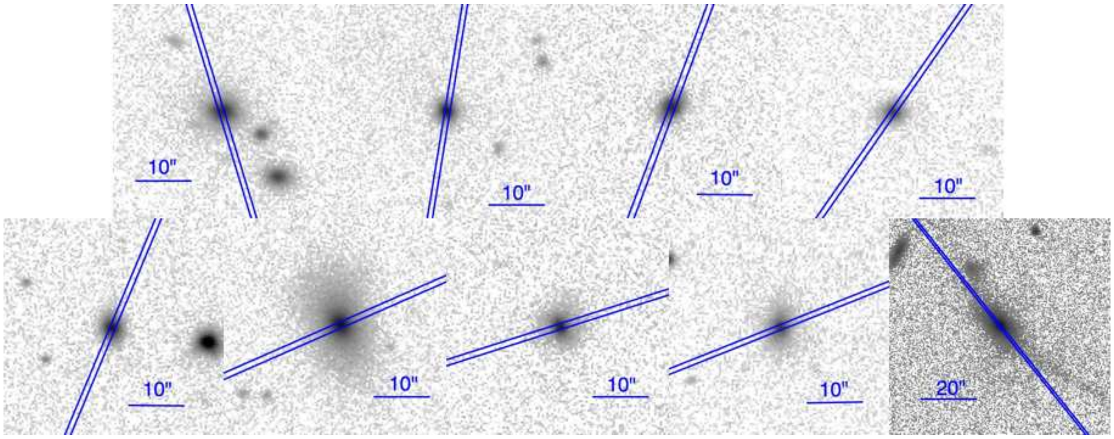

Fig. 2.1.— SDSS g band images of the post-starburst galaxies. The slit used during the LRIS observation is over-plotted in blue and oriented along the observed PA. The order of the objects is *top*: $0119+0107$,$0224-0937$,$0303-0836$,$0328+0045$, *bottom*: $2041-0513$,$2102+1032$,$2307+1525$,$2328+1446$, and $2337-1058$. All objects are displayed with a log brightness scale. The brightness of object $2337-1058$ has been modified to display a faint surface brightness tidal tail.

the continuum of the templates and the observed galaxy. Such differences can arise from reddening or from non-stellar emission. The χ^2 function is minimized through the amoeba routine from Numerical Recipes (written for IDL by W. Thompson).

The χ^2 function requires a measurement of the errors on each datum. As discussed in the previous section, we calculated errors based on the sky level using Poisson statistics. In order to block a particular region from the fit, we artificially set the error bars on those data to be several orders of magnitude higher than the unblocked region. This essentially eliminates the contribution to the χ^2 function from these data. This was only done to block the Mg Ib absorption line (see below) and additionally for two objects that had emission lines in the Mg Ib region.

2.3.1. Stellar Population Templates

We created galaxy templates by mimicking stellar populations of varying ages. We observed template stars with LRIS during previous observing runs in May and September 2010 (see Hiner et al. 2012b, for details). We created seven stellar population templates by combining the template stars with varying proportions. The templates approximate stellar populations of varying ages by comparison with models from Charlot & Bruzual (2007, private communication). The youngest template was created using a single A0 star. The other templates were created using combinations of all spectral types. In order to model "older" stellar populations, we removed contribution from early type stars (A and F). The templates approximate stellar populations of ages 202, 286, 453, 508, 718 Myr, 1.015, and 10.0 Gyr. Table 2.2 shows the proportions of each spectral type used in creating the model stellar populations.

2.3.2. Balmer region

We fit the 3500 – 4500 Å region of the galaxies. This includes the entire Balmer series beginning with Hγ, the Ca H+K lines, the G-band, and other smaller spectral features. While this region is dominated by the Balmer series, the smaller spectral features are clear in the high signal-to-noise data. These smaller features can be easily attributed to the later type stars, and are dominant in the older spectral template. Thus, when we fit this region, the young stars are best constrained by the Balmer series, and the old stars are best constrained by the smaller features, the G-band, and the Ca lines.

In the case of object $2307+1525$, we adopt a model that did not produce the lowest χ^2. The model that produced the lowest χ^2 value did not match a the Ca K feature and also had zero contribution from the older template. This being unrealistic, we refit the object using the youngest aged template. This better matched both the Ca K feature and maintained a contribution from the older population.

2.3.3. Mg Ib region

We fit the 4600 – 5600 Å region of the spectra. This includes the Hβ absorption line, the Mg Ib line, and other stellar features. The Mg Ib region is typically dominated by the older population. In order to place a strong constraint on the young population contribution, we included the Balmer line in this region. While many have focused on the Mg Ib region alone ($\lambda > 5000$Å), including the Hβ line is not unprecedented. Bender & Nieto (1990) use a similar region in the study of dwarf spheroidals and compact elliptical galaxies.

In Fig. 2.5 and 2.6, we show the best fit models of the Balmer region and the Mg Ib region simultaneously. There is good agreement between the two regions, with the exception of two objects. Objects 2102 and 2337 were each fit best by the 286 Myr young template in the Balmer region, but in the Mg Ib region they were each best fit with the 202 Myr template. All other objects were fit by the same aged templates between the two regions.

2.3.4. Ca Triplet

The Ca T region is dominated by light from late type stars, and has been used in the past as a way of measuring velocity dispersions in a variety of galaxy morphological types (*e.g.,* Dressler 1984). We observed four spectral types to create templates of the Ca T region: a G0, G5, K0, and K5 star. We created three templates. The first consisted of all four stars with weights favoring the G stars. The second had no contribution from the G0 star, and the third consisted solely of the K stars. We fit each galaxy with the three templates and each of the individual stars for a total of seven different galaxy templates. Many of the fits were comparable, but we chose the "best-fit" as the one which produced the minimum χ^2.

2.3.5. Uncertainties

The uncertainty on the fits is dominated by the template mis-match. We performed monte-carlo simulations to determine the error contributed from the noise in the spectra. Recall that the signal-to-noise is high, so we do not expect this to be a large factor. We added randomized Poisson noise determined from the sky level to the best-fit models as a basis to create a set of synthetic spectra. Fits of the spectra then reproduce the best-fit model with variations in the parameters that are due to sky noise. We recovered the "best-fit" velocity dispersions of the galaxy with errors of only a few km s^{-1}.

In order to better understand the uncertainties in each wavelength region contributed by template mis-match, we examine the difference in velocity dispersion between the fitted templates. We calculate the standard deviation of velocity dispersions fitted using the various templates. Uncertainty on the old population due to template mismatch tends to be larger than on the young population, especially when measured in the Balmer region. This is most likely because as the stellar populations age, the spectra become more degenerate with the old population. Our templates include more contribution from later type stars when we artificially age them. Thus, when testing the older population templates, a degeneracy arises between the young and old population. The young population is still additionally constrained by the Balmer series, but the older population σ_* parameter is free to adjust to any inaccuracies generated by including later type stars which are assigned the younger population σ_*.

We also fit each spectrum by adding a single K to a single A star. The K star template is an average of our observed stars that have K spectral types (K0, K2, K5, and K7). Similarly the A star template is an average of our observed A2 and A5 stars. We note that the A0 star had different absorption line ratios. In particular, the Ca K line was significantly smaller in this spectrum compared to the A3 and A5 stars, so we left it out of the A star average and tested it separately. We present the results of these fits in Table 2.4, and we discuss the differences between the single star measurements and the population template measurements in the following section.

2.4. Results

In this section we compare the σ_* values from the young and old populations in the different wavelength regions. The kinematics of the young population have primarily been determined by the Balmer series. However, the young population templates include contributions from a range of stellar spectral types (A, F, G, and K).

2.4.1. Velocity Dispersions

As discussed above, we have fit both young and old populations with individual velocity dispersions in three different wavelength regions: the Balmer region, the Mg Ib region, and the Ca T region. Here we show the differences in velocity dispersions as measured from the different regions and populations. In order to determine if measurements are consistent with each other, for example between measurements of the same population from different wavelength regions, we calculate a parameter, δ, as follows:

Table 2.2: Template Proportions

Age (Myr)	A0	A3	A5	F0	F5	F8	G0	G5	G8	K0	K2	K5	K7	M0	M8
202	1	0	0	0	0	0	0	0	0	0	0	0	0	0	0
286	0.166	0.152	0.136	0.121	0.106	0.091	0.076	0.061	0.045	0.030	0.015	0.0	0.0	0.0	0.0
453	0.0	0.163	0.148	0.133	0.118	0.103	0.088	0.073	0.057	0.042	0.027	0.012	0.012	0.012	0.012
508	0.0	0.0	0.161	0.146	0.131	0.115	0.100	0.085	0.070	0.055	0.040	0.024	0.024	0.024	0.024
718	0.0	0.0	0.0	0.159	0.144	0.129	0.114	0.098	0.083	0.068	0.053	0.038	0.038	0.038	0.038
1015	0.0	0.0	0.0	0.0	0.158	0.143	0.128	0.113	0.098	0.083	0.067	0.052	0.052	0.052	0.052
10000	0.0	0.0	0.0	0.0	0.0	0.0	0.0	0.167	0.151	0.136	0.121	0.106	0.106	0.106	0.106

Table 2.3: Velocity Dispersions

N	RA	DEC	Balmer		Mg Ib		Ca T
			Young	Old	Young	Old	Old
1	011942.10	+010750.8	132 ±11	163 ±68	115 ±27	206 ±14	⋯
2	022427.02	−093739.1	81 ±7	76 ±41	88 ±9	109 ±70	⋯
3	030319.22	−083619.0	101 ±6	112 ±22	93 ±13	114 ±19	⋯
4	032801.61	+004502.0	157 ±12	183 ±71	179 ±3	157 ±21	⋯
5	204132.52	−051334.0	74 ±11	83 ±31	211 ±43	72 ±9	109^{+24}_{-22}
6	210258.78	+103259.8	195 ±15	174 ±35	89 ±12	227 ±10	248^{+42}_{-55}
7	230743.41	+152558.1	86 ±19	111 ±65	137 ±14	103 ±28	101^{+23}_{-21}
8	232806.02	+144625.2	75 ±15	33 ±32	150 ±19	61 ±24	81^{+19}_{-17}
9	233712.71	−105800.3	150 ±9	167 ±53	224 ±22	189 ±8	206^{+44}_{-42}

Note. — Best fit velocity dispersions for the young and old components of each galaxy. Balmer Young templates all objects: - 286 Myr with the exceptions of 0119 (- 202 Myr).

Table 2.4: K+A tests

N	RA	DEC	Balmer A	Balmer K	Mg Ib A	Mg Ib K
1	011942.10	+010750.8	135	176	132	223
2	022427.02	−093739.1	105	103	123	101
3	030319.22	−083619.0	132	121	140	103
4	032801.61	+004502.0	183	195	236	163
5	204132.52	−051334.0	102	97	248	81
6	210258.78	+103259.8	220	191	113	240
7	230743.41	+152558.1	133	88	155	75
8	232806.02	+144625.2	113	46	166	66
9	233712.71	−105800.3	179	170	213	183

Note. — Best fit velocity dispersions for the using K+A templates. The K star is an average of K0, K2, K5, and K7 stars. The A star is an average of an A3 and A5 star. Balmer: $0119 + 0107$ was better fit with an A0 star instead of the A star average. Mg Ib: $0119 + 0107$ was best fit by a single A0 star in our previous fitting, so we adopted that fit over the A35 fit.

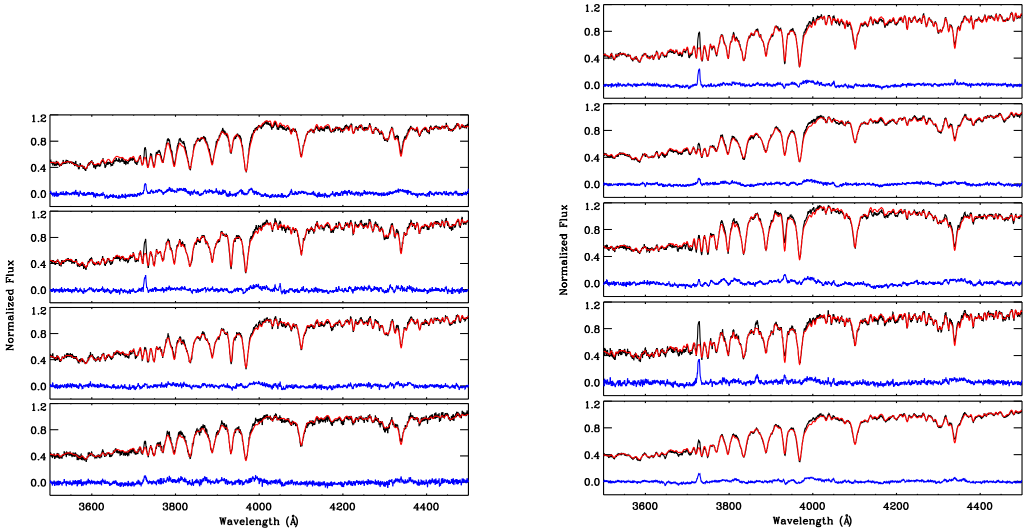

Fig. 2.2.— Fits of the Balmer region. Objects are listed in order of increasing RA as presented in Table 2.1. The black line depicts the LRIS spectrum in the rest frame. The best fit model is over-plotted in red. The residuals are plotted in blue.

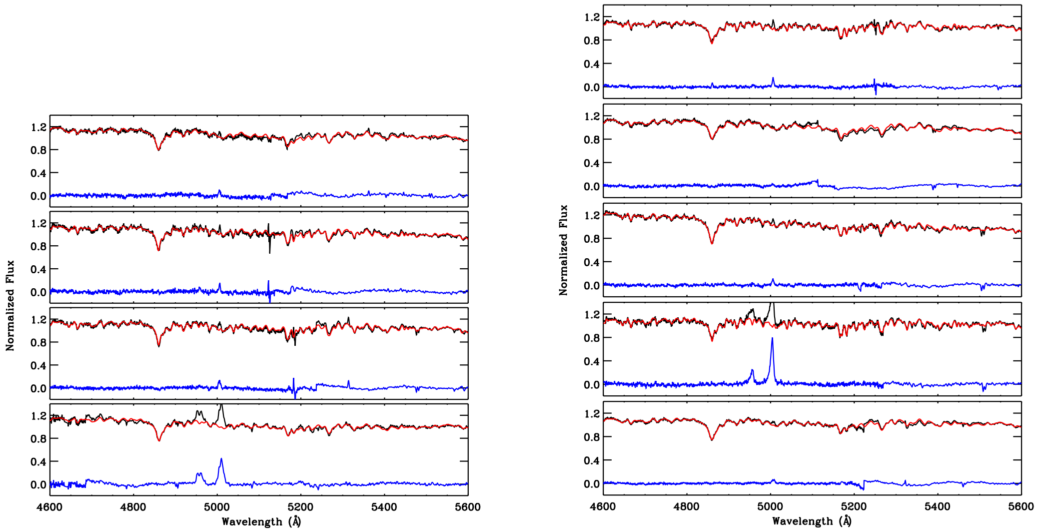

Fig. 2.3.— Fits of the Mg Ib region. Object order and plotted colors are the same as Fig. 2.2

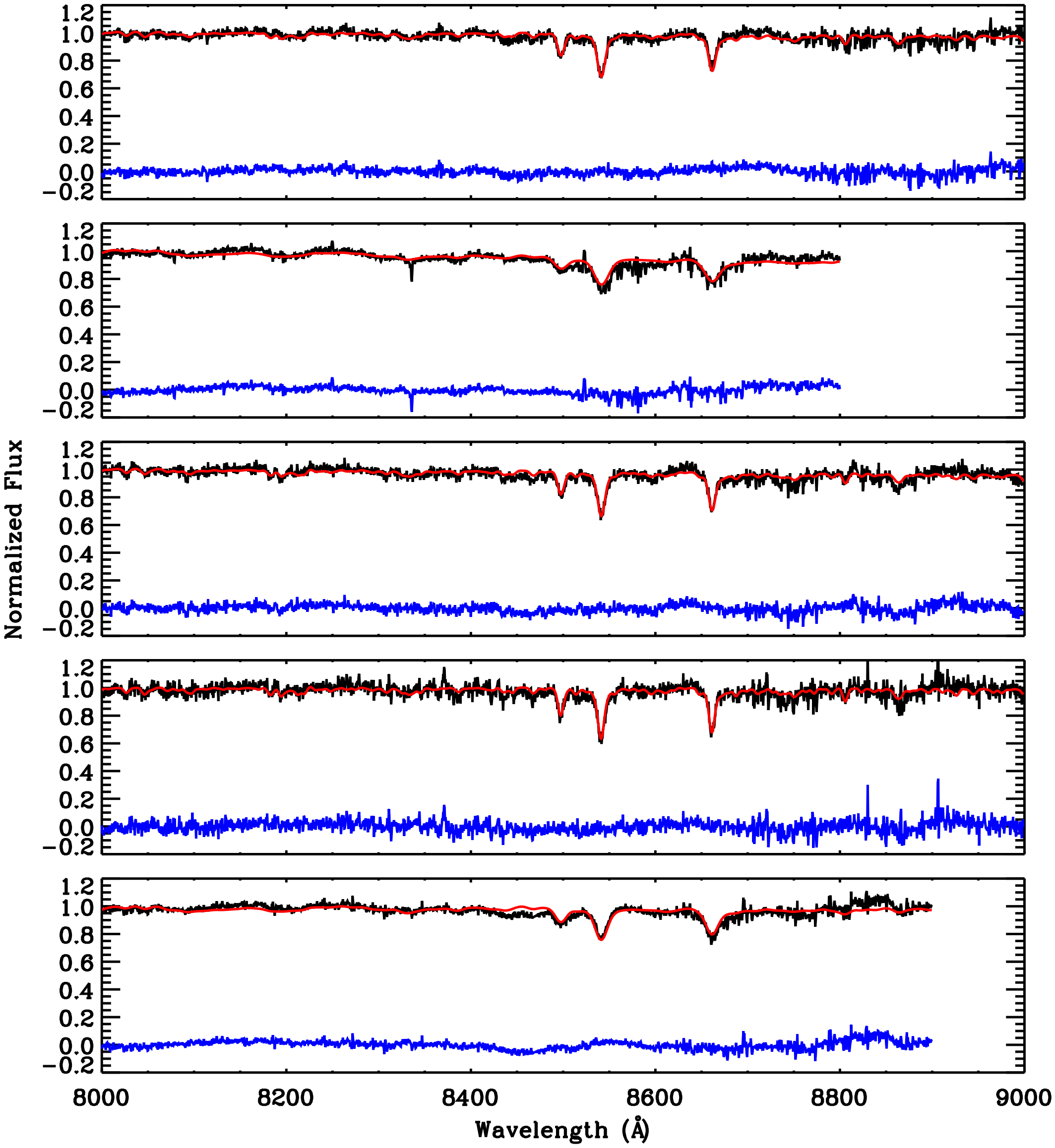

Fig. 2.4.— Fits of the Ca triplet region. The plotted colors are the same as Fig. 2.2. The order of the objects is $2041-0513$, $2102+1032$, $2307+1525$, $2328+1446$, $2337-1058$.

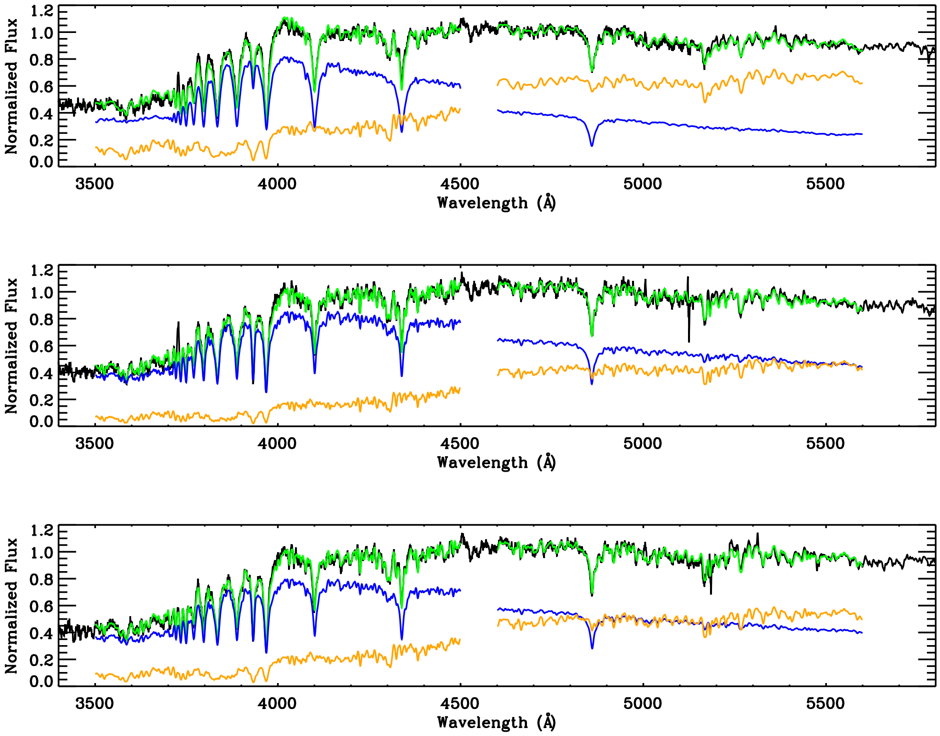

Fig. 2.5.— Fits of the Balmer and Mg Ib regions with components shown. The data are plotted in black and the best fit models over-plotted in green. The relative young and old components are shown in blue and orange, respectively. Objects shown are $0119 + 0107$, $0224 - 0937$, and $0303 - 0836$.

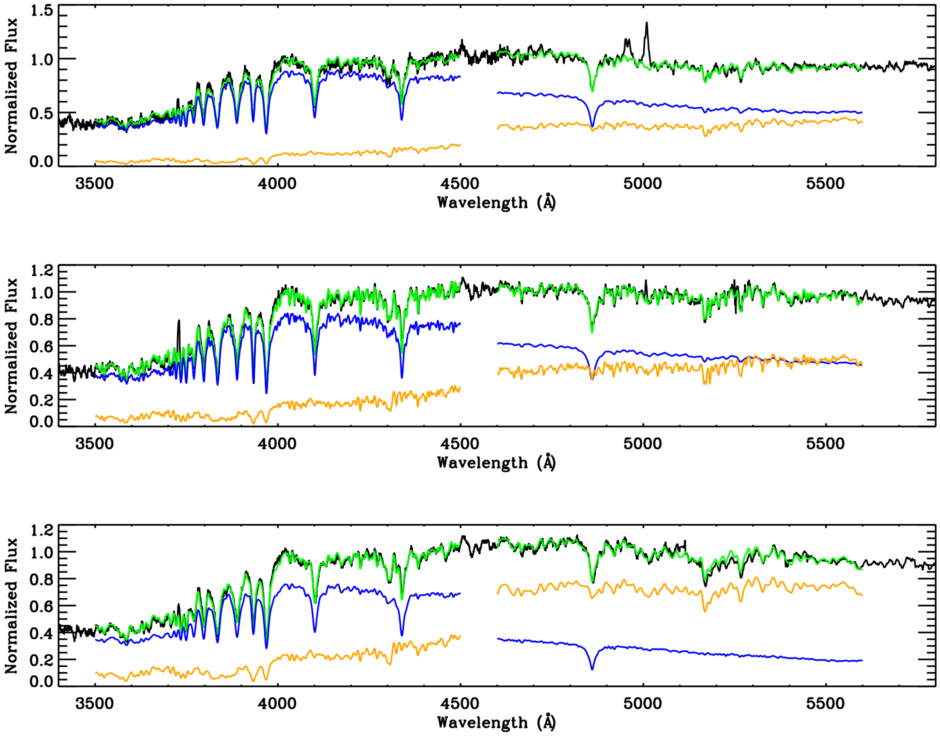

Fig. 2.6.— Same as Fig. 2.5. Objects shown are 0328+0045, 2041−0513, and 2102+1032.

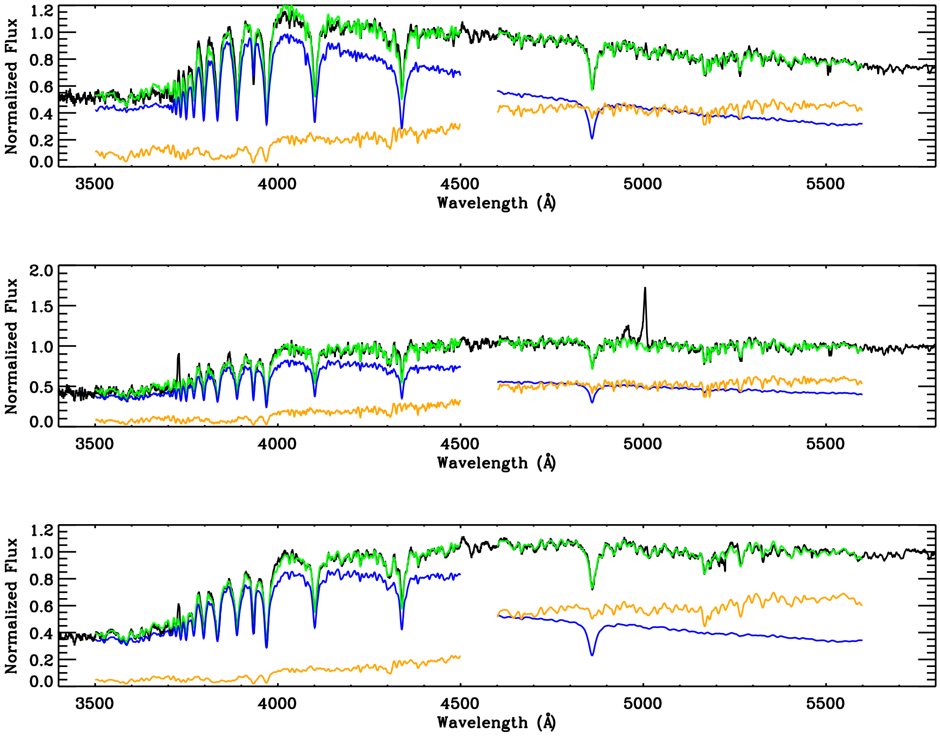

Fig. 2.7.— Same as Fig. 2.5.Objects shown are 2307+1525, 2328+1446, and 2337−1058.

$$\delta = \frac{Y - X}{\sqrt{\sigma_Y^2 + \sigma_X^2}} \tag{2.2}$$

where Y represents the ordinate and X the abscissa values, and the σ values are the respective errors. If this value falls within the range -1 to 1, the Y measurement is considered consistent with the X measurement within the error.

Figure 2.8 shows the velocity dispersions of the young components compared to the old components as measured in the Balmer region. The dashed line is a one-to-one correlation. The objects are correlated and roughly match the one-to-one line with some scatter. The solid line is a linear fit to the data, which shows a slope that is close to unity (0.96). This slope is likely dependent on the number of included points and would be more robustly determined with more measured objects. With the exception of one object, all of the young σ_* are consistent with the old σ_* within the estimated error bars. On the surface, this may indicate the that the kinematics of the young and old populations are determined by the same potential.

The right panel of the figure compares the old velocity dispersion from the Balmer region with the velocity dispersion measured from the Ca T region. The G-band and smaller stellar absorption lines in the Balmer region should be produced by the same population that produces the Ca T absorptions. We might expect the velocity dispersions to be the same within the measurement error. Indeed the two are correlated (with a linear slope of 1.1), but it appears that the Ca T dispersions are systematically offset from the Balmer region dispersions by approximately 26 km s^{-1}.

Figure 2.9 compares the fits of the Balmer region using our stellar population models with the simpler method of using a K+A star model. Again the dashed line shows a one-to-one correlation. The left panel shows the young component compared to the single A star model. In all cases but one the A star over estimates the velocity dispersion by approximately 30 km s^{-1}. The fitted correlation has slope of 0.97. The single point where the A star velocity dispersion is the same as the stellar population represents object $0119 + 0107$. The population that best fit this object was simulated with a single A0 star, so in fact the two templates use the same spectrum to model the young component. The right panel of the Fig. 2.9 compares the old component population model measured in the Balmer region with the single K star model. Here we find that the correlation is close to one-to-one with a slope of 0.94 and an offset of only 8 km s^{-1}. Every object has a σ_* value measured from the old population that is consistent with that of the K star average.

Figure 2.10 compares the measurements from the Mg Ib region, analagous to Fig. 2.8 for the Balmer region. The left panel shows the comparison between the σ_* measured for the young population and that of the old population. However, unlike in the case of the Balmer region, we find no correlation between these two measurements. The right panel of the figure shows that the σ_* value of the old population is consistent with those values measured in the Ca T region, but the correlation has an average offset of 23 km s^{-1}. The Mg Ib region is dominated by weak stellar features that are primarily attributed to the older stellar population. The only strong line constraining the young population is the Hβ absorption line. It seems likely that because the young population is not well constrained here, the σ_* measurements of that component are not trustworthy.

Figure 2.11 shows the comparison between the K+A templates and the population models for the Mg Ib region, analagous to Fig. 2.9 for the Balmer region. We find that the σ_* of the young population is again overestimated by a single A star compared to using a population model. This result is similar to that of the Balmer region. Furthermore, the measurements of σ_* for the old population are very consistent between the K star template and the old population template.

Figure 2.12 compares the σ_* measurements of the young population as measured in the Balmer and Mg Ib regions in the left, and those of the old population in the right panel. In the left panel there is no apparent correlation between the dispersions of the young populations as measured in the two regions. This casts further doubt on the young population σ_* of the Mg Ib region. The Balmer region contains many more absorption lines to constrain the fit for the young population, so it is more trustworthy. We do see a correlation between the measurements of the older population. The linear fit shows that on average measurements of the older population σ_* in the Mg Ib region show a larger values than in the Balmer region by ~ 15 km s^{-1}.

2.4.2. Faber-Jackson Relations

The Faber-Jackson relation is well established for dynamically stable passively evolving galaxies (Faber & Jackson 1976; Desroches et al. 2007; Nigoche-Netro et al. 2010). The relation is a projection of the fundamental plane and is a result of the

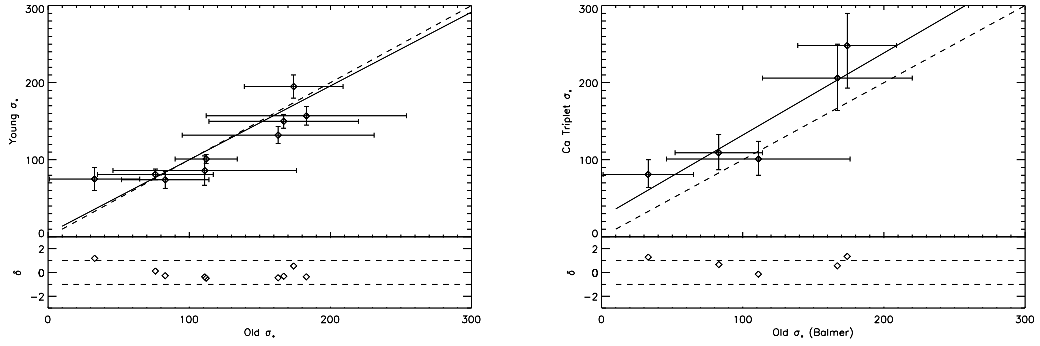

Fig. 2.8.— *Left*: velocity dispersions of the young and old stellar populations as measured in the Balmer region. *Right*: velocity dispersions of the old stellar population in the Balmer region compared to that of the Ca T region.

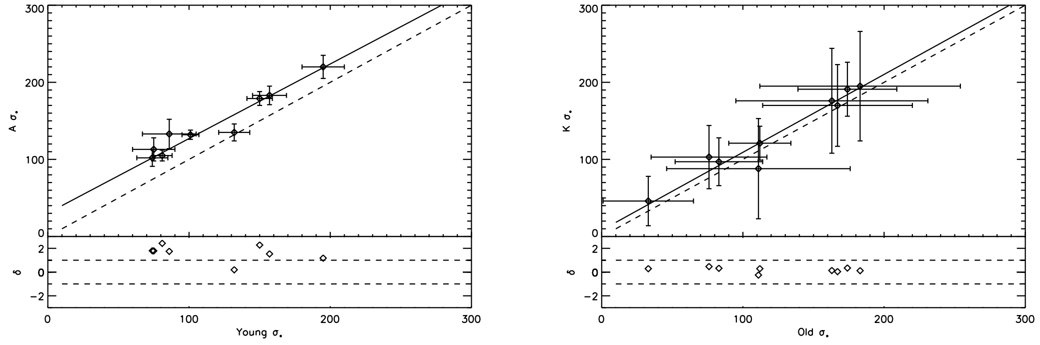

Fig. 2.9.— *Left*: velocity dispersions of the young stellar population as measured in the Balmer region using a population compared to using an average A star. *Right*: velocity dispersions of the old stellar population in the Balmer region compared to using an average K star.

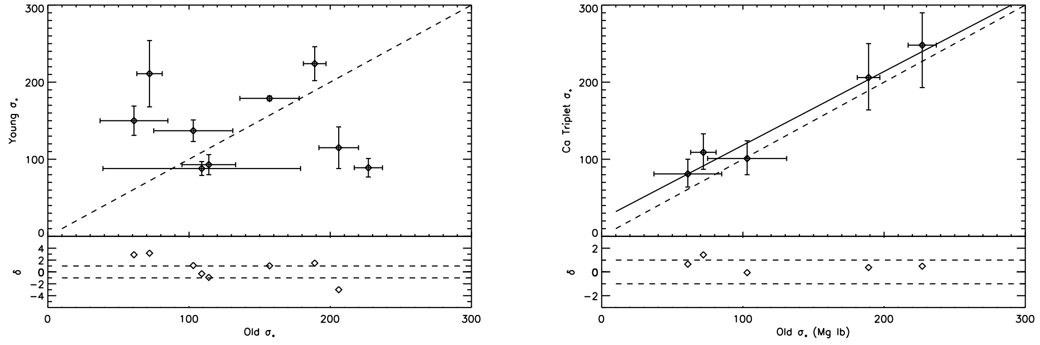

Fig. 2.10.— *Left*: velocity dispersions of the young and old stellar populations as measured in the Mg Ib region. *Right*: velocity dispersions of the old stellar population in the Mg Ib region compared to that of the Ca T region.

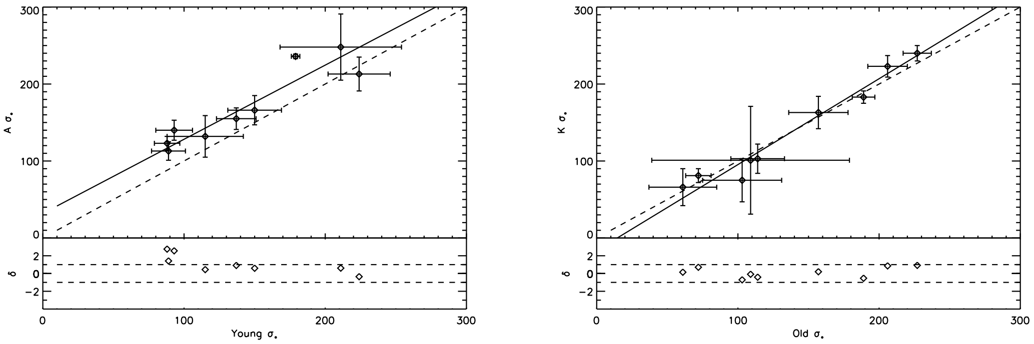

Fig. 2.11.— *Left*: velocity dispersions of the young stellar population as measured in the Mg Ib region using a population compared to using an average A star. *Right*: velocity dispersions of the old stellar population in the Mg Ib region compared to using an average K star.

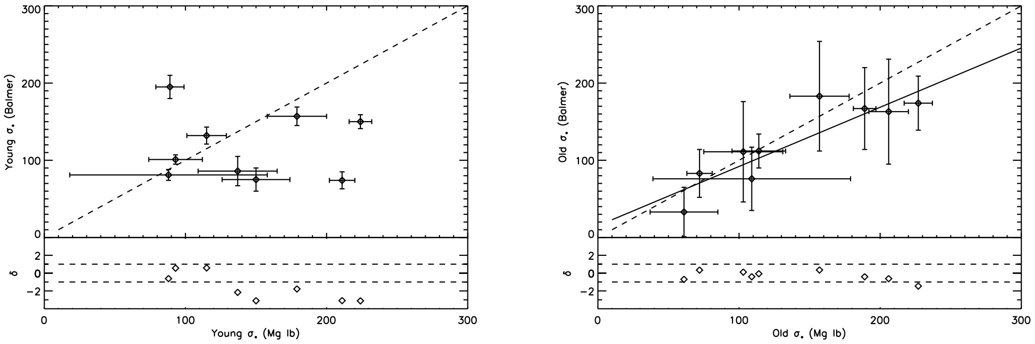

Fig. 2.12.— *Left*: velocity dispersions of the young populations compared between the Balmer region and the Mg Ib region. *Right*: velocity dispersions of the old stellar populations compared between the Balmer region and the Mg Ib region.

virial theorem and the mass-to-luminosity ratio of stars and galaxies. We can use the Faber-Jackson relation to investigate if the objects are in dynamical equilibrium, or if the kinematics are peculiar compared to bulges that are in dynamical equilibrium. Norton et al. (2001) plot their post-starburst galaxies on the $\mathrm{M_R}-\sigma_*$ plane and find that the young population of their sample did not follow the established Faber-Jackson relation. The older population followed a similar trend as the Faber-Jackson relation, but was offset in magnitude toward lower σ_* or brighter luminosities. Similarly, Swinbank et al. (2012) plot their sample on the $\mathrm{M_K}-\sigma_*$ plane. While many of their objects are consistent with the relation, several show an offset toward lower σ_* values or higher luminosities.

In comparing our results with those from Norton et al. (2001), it is important to note the differences in method of measuring σ_*. Norton *et al.* fit two small spectral regions from 4100 – 4500 Å and 4800 – 5250 Å. The first region contains Hδ, Hγ, and the G-band, while the second contains the Hβ and Mg Ib lines. Furthermore, they only use the following spectral types: A2, A3, G4, G8, K0, and K3. We have compared the differences of using an average A star with a simulated population template and found that the single spectral type tends to predict larger values of σ_* than the population template. However, this is only significant for the young population. Were Norton *et al.* to have used stellar population templates, they may have measured smaller σ_* than they did for the young population. In terms of the Faber-Jackson relation, this would shift their objects to smaller σ_* and perhaps create a systematic offset from the observed relation for the young population in addition to the old population. Swinbank et al.

(2012) use a shorter wavelength region from $\sim 3800 - 4290$ Å, which covers Ca H+K and several Balmer lines, but do not separate the young and old populations.

We used the SDSS magnitudes along width our measured redshifts, K-corrections (Chilingarian et al. 2010), and passive evolution corrections (van Dokkum & Franx 2001) to derive absolute magnitudes in the g and r bands. The K-corrections account for differences in measured luminosities due to redshift and spectral color. We used the online calculator[1] described by Chilingarian et al. (2010) and input the SDSS measured magnitudes and colors to derive K-corrections.

Passive evolution corrections account for the fading of stellar populations as they evolve between the observed redshift and $z = 0$. We used the online calculator[2] of van Dokkum & Franx (2001). The redshifts of our sample are quite low ($z < 0.1$) with the exception of one object, which has $z = 0.2$, so we do not expect the correction to be very large. We applied the "Default 1" setting of the calculator with a modification to approximate the age of the starburst population at the observed redshift. Specifically, we modified the formation redshift parameter to be 0.13 for the low redshift objects. The difference in age of the universe between redshift 0.1 and 0.13 is approximately 350 Myr. Most of the objects in our sample were best fit with the 286 Myr model, so this is an appropriate value. For the object at $z = 0.2$, we chose a formation redshift of $z_f = 0.25$. The difference between which is about 500 Myr. As a result of this modification, the passive evolution correction is much stronger than it would be if we assumed the stars

---

[1] http://kcor.sai.msu.ru/

[2] http://www.astro.yale.edu/dokkum/evocalc/

were all formed at $z >> 1$. This determination of the passive evolution correction may be an over-estimation for many of these galaxies. Unfortunately the calculator only provides corrections in redshift steps of 0.1, while the majority of our objects exist at $z < 0.1$.

In Fig. 2.13 we show σ_* plotted against the AB absolute magnitude of the galaxy. The left panel shows the σ_* values measured from the young population while the right panel shows those measured from the old population. Measurements of σ_* from the Balmer, Mg Ib, and Ca T regions are plotted in blue diamonds, orange asterisk, and red squares, respectively. Dotted lines represent the g band and r band magnitude-dependent Faber-Jackson relations as measured by Nigoche-Netro et al. (2010). The solid line represents the overall fit to the relation for all magnitude bins. The magnitude-dependent relations have scatter on the order of 0.25 dex, while the overall relation has scatter on the order of 0.6 dex. Given the uncertainty in our measurements, the majority of points are consistent with the fitted Faber-Jackson relations, regardless of the population.

Figure 2.14 is similar to Fig. 2.13, but examines the r band magnitudes. In addition to the relations determined by Nigoche-Netro et al. (2010), we also plot a quadratic fit (thick black line with shaded region depicting scatter in the relation) to the Faber-Jackson relation determined by Desroches et al. (2007). If we only compare our measurements to the relation determined by Nigoche-Netro *et al.*, then we see a similar result to what was seen the g band. However, if we instead compare our measurements with the Desroches *et al.* relation, we see a different picture. The old population σ_* measurements tend to be more consistent between wavelength regions the young population σ_*, and only one galaxy seems to fall significantly below the relation from Desroches et al. (2007). However, the young population σ_* from the Balmer region (blue points) have 4/9 points just below the relation, all at lower galaxy luminosity. Norton et al. (2001) found a similar result, but for the old population, not the young population.

To further investigate the dependency of the velocity dispersions on the galaxy magnitudes, we measured the luminosities of the young and old components individually. To measure the absolute magnitudes for the individual components, we first calculated the scaling factor between our total fitted model from the Balmer region and the absolute photometry calculated from the SDSS data. Applying the scale to the individual model components we then obtained absolute photometry of the components by integrating the SDSS transmission curves over our spectra. The general result is that the magnitudes of the individual components are the fractional contribution to the total magnitude of the objects. Consequently, the magnitudes are fainter than the total magnitude.

We plot the young component magnitudes in Fig. 2.15 along with young component σ_* values. In the g band, the objects now appear above the Nigoche-Netro et al. (2010) relation, but they fall within the scatter. In the r band, the measurements are still within the scatter determined by Nigoche-Netro *et al.*. However, those that at first appeared below the relation now are in alignment with it.

We plot the older component magnitudes in Fig. 2.16 along with the older component σ_* values. In the g band, it appears that the objects have migrated systematically above the relation determined by Nigoche-Netro et al. (2010). In the r band, the measurements are still consistent within the determined uncertainties. However, the brighter objects may be offset to higher σ_* values. The uncertainties are fairly large on the older population σ_*, so it is difficult to discern how real the observed migrations really are.

2.5. A Case Study of $2337-1058$

We serendipitously observed this galaxy with the slit oriented very close to the major axis of the galaxy (see Fig. 2.1). This provides an opportunity to study the internal kinematics of the two populations and to determine if the observed ellipticity of the galaxy is due to rotational flattening or if the galaxy is largely pressure supported. From the SDSS imaging, it is clear that this object is actively undergoing a merger event. A companion galaxy can be seen just to the North of the main galaxy, and a tidal tail extends to the SW. Our slit was oriented roughly NE-SW along the major axis. The object lies at $z = 0.0783$, providing an angular scale of 1.462 kpc arcsec^{-1}.

We measured the ellipticity of the galaxy by fitting a Sérsic profile to the main galaxy using the SDSS g band image. Since we were only interested in the ellipticity, we did not perform a detailed fit. We used a star located on the same image frame as the PSF to be convolved with the Sérsic profile. The best-fit function left residuals extending between the tidal tail and the companion galaxy. We measured an axis ratio of $b/a = 0.43$, corresponding to an ellipticity of $\epsilon = 0.90$.

To determine if this ellipticity can be produced by rotational flattening of the galaxy, we measured the line-of-sight velocity, v_{los}, and velocity dispersion, σ, of eleven aperture extractions along the major axis of the galaxy. Each aperture extraction was offset from

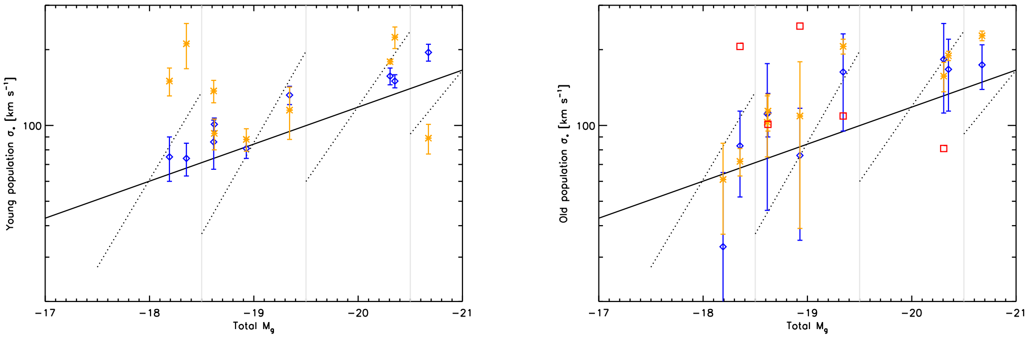

Fig. 2.13.— The Faber-Jackson relation for post-starburst galaxies. *Left*: The velocity dispersion of the young component compared to the total g band absolute magnitude. *Right*: The velocity dispersion of the old component compared to the total g band absolute magnitude. Blue symbols were measured in the Balmer region. Orange symbols were measured in the Mg Ib region. Red symbols were measured in the Ca T region.

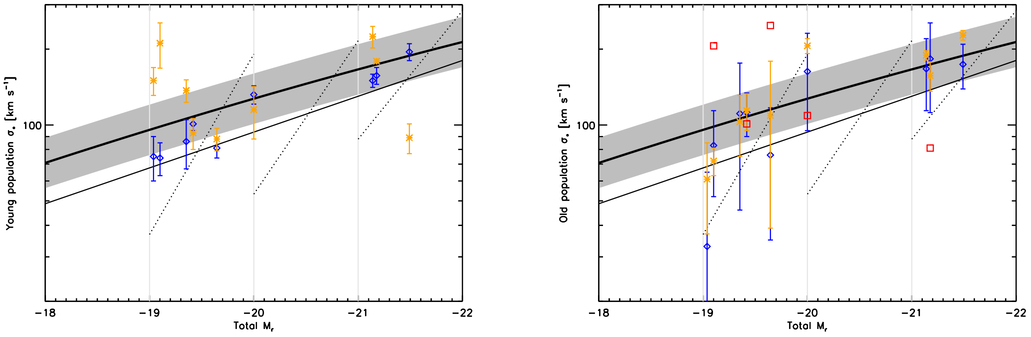

Fig. 2.14.— The Faber-Jackson relation for post-starburst galaxies. *Left*: The velocity dispersion of the young component compared to the total r band absolute magnitude. *Right*: The velocity dispersion of the old component compared to the total r band absolute magnitude. Blue symbols were measured in the Balmer region. Orange symbols were measured in the Mg Ib region. Red symbols were measured in the Ca T region.

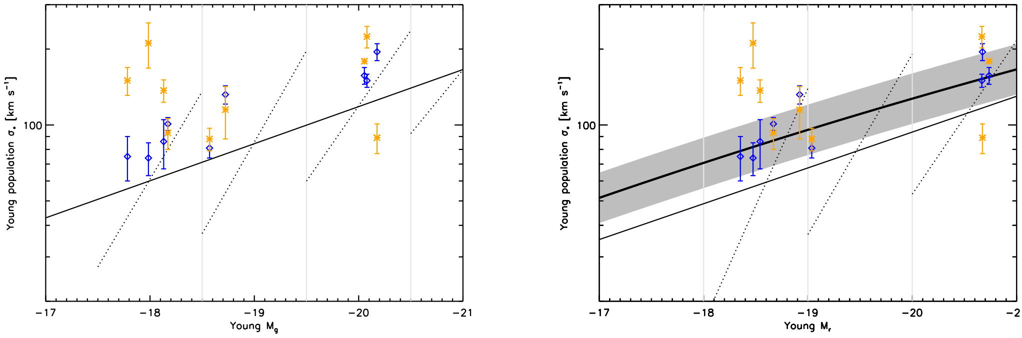

Fig. 2.15.— *Left*: They young stellar population's σ_* compared to its contribution to the host luminosity in the g band. *Right*: the same as the left panel but for the r band.

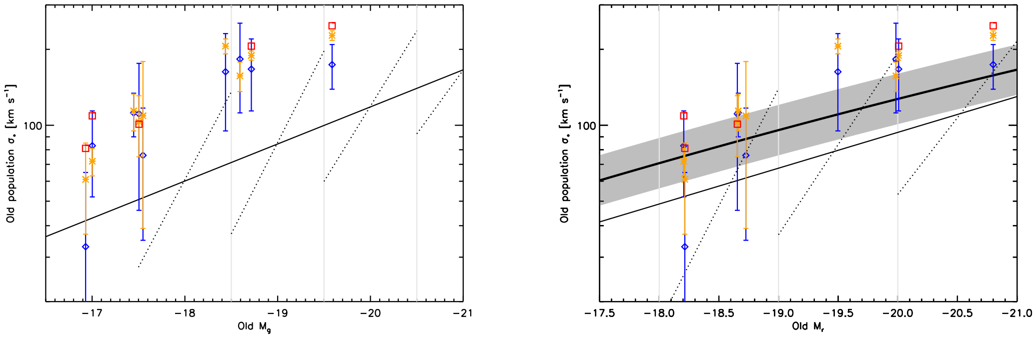

Fig. 2.16.— The same as Fig. 2.15, but for the old stellar population.

its neighboring aperture by $0\farcs6$, the resolution limit of our seeing conditions. This corresponds to a physical separation of 0.877 kpc per aperture at $z = 0.0783$. We performed the same spectral fitting on the Balmer region as described above.

Table 2.5 shows the measured values for both the young and old components of the galaxy using the Balmer region. Figure 2.17 shows the values plotted as a function of position within the galaxy. From the figure it is clear that some rotation is present in the galaxy. Line-of-sight velocities are positive along the NE direction of the slit relative to the central aperture, and negative along the SW direction of the slit. Furthermore, the rotation of the young and old components generally match one another. The σ_* values of the young component have a positive gradient with increasing radius. This result is consistent with models from Bekki et al. (2005). Furthermore, the young component σ_* is smaller than that of the older component in the innermost apertures. Bekki *et al.* also found this offset in both major and unequal-mass merger models, although the magnitude of the effect is much greater in their simulations.

To determine if the observed ellipticity is due to rotational flattening, as might be the case for a galaxy that collapsed from a single primordial gas cloud, we calculate the anisotropy parameter:

$$(v/\sigma)^* = \frac{(v/\bar{\sigma})}{\sqrt{(\epsilon/(1-\epsilon))}} \tag{2.3}$$

where v is the maximum observed line-of-sight velocity (centroid of absorption lines), σ is the velocity dispersion (second moment of absorption lines), $\bar{\sigma}$ is the average of the velocity dispersions within the effective radius and ϵ is the ellipticity of the galaxy (Bender & Nieto 1990; Kormendy 1982). If $(v/\sigma)^* \sim 1$, then the flattening can be due to rotation. That is, during a monolithic collapse, angular momentum is conserved and tends to flatten objects. If, on the other hand, $(v/\sigma)^* << 1$, then the random motion of the stars (σ) are sufficiently high to rule out such a rotational flattening, and the object has an anisotropic σ_*tensor. In the case of $2337-1058$, $(v/\sigma)^* = 0.091$ and 0.086 for the young and old components, respectively.

Judging from the morphology shown in the SDSS image, and the kinematics determined by our analysis, the post-starburst galaxy $2337-1058$ was most-likely created during a merger event. The smaller galaxy has "swung in" and around the larger elliptical. It likely arrived from the SW and is now receding from our line-of-sight (positive v) in the NE. This object is a typical example of how post-starburst galaxies form and evolve into passive pressure-supported ellipticals.

2.6. Discussion

We have measured velocity dispersions of different stellar populations within a sample of nine post-starburst galaxies selected from Goto (2007). The stellar kinematics of post-starburst galaxies can be directly observed by fitting population templates to observed spectra. Furthermore, with sufficiently high signal-to-noise, it is possible to distinguish between young and old populations. While spectra of young populations are dominated by Balmer transitions in the optical, older populations have many less prominent features, of which the Ca H+K lines and G band are strongest.

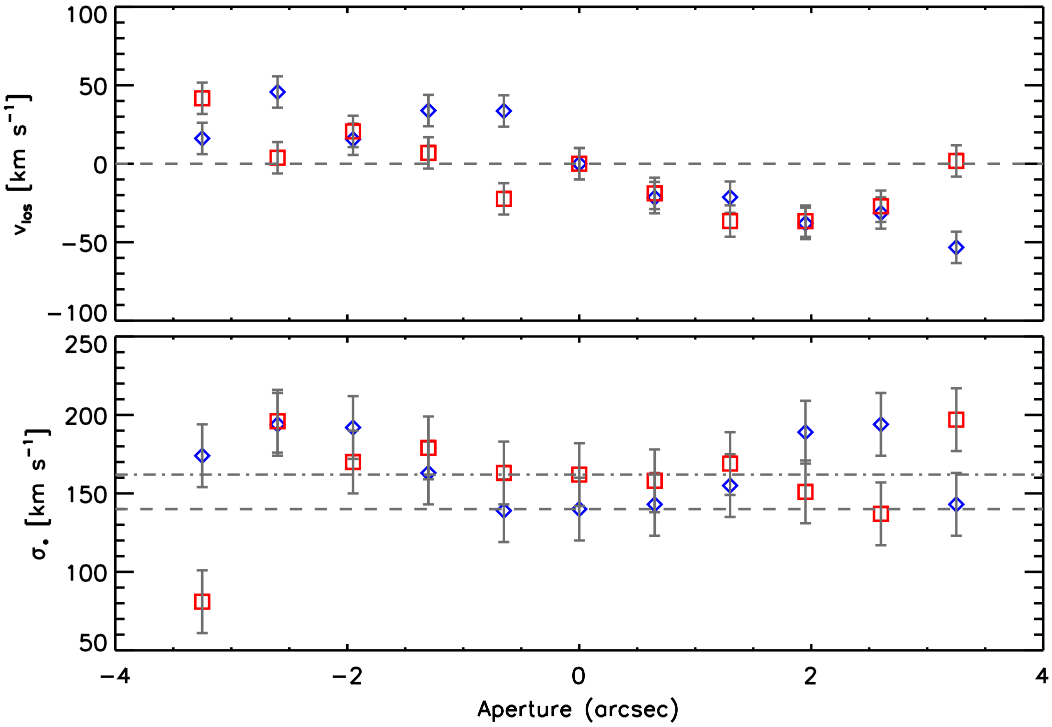

Fig. 2.17.— Kinematics of 2337 − 1058. The young population kinematics are plotted as blue diamonds, and the old population as red squares. *Top*: The line-of-sight velocity is plotted relative to the value from the central aperture. *Bottom*: The velocity dispersion as measured in each aperture. Each aperture is separated by the seeing limit 0.″6. The physical scale is 1.462 kpc arcsec^{-1}.

Measurements of the young population are best constrained in the Balmer region, where there are a multitude of absorption lines attributed to this population. We have shown that using only a single spectral feature (Hβ) to constrain the velocity dispersion is not reliable. Furthermore, it is important to fit the galaxy spectrum with a population model rather than a single A star. Using a single A star systematically over predicts the velocity dispersion of the young component whether measured in the Balmer region or the Mg Ib region.

The older population can be fit simultaneously with the younger population, even in the Balmer region where the luminosity is dominated by young stars. In this region there still exist smaller spectral features (including the G-band) that are prominent in the older population. As long as the spectra are sufficiently high signal-to-noise, these features can constrain the older population parameters reasonably well. In both the Balmer region and the Mg Ib region, the older population is modeled equally well using either a population model or a single K star average. This is likely simply due to the fact that older populations are dominated by the later type stars, which all have similar features. However, the kinematics of the older population are more uncertain than those of the young population due to template mis-match. This is because a degeneracy develops between the old population and the “aged” young population templates where later type stars become more prevalent.

The σ_* values measured from the Ca T region are more closely aligned with old population σ_* from the Mg Ib region than the Balmer region. Even still, 3 of 5 measurements from the Balmer region are consistent with the Ca T measurements within the errors. Interestingly Fig. 2.8 implies that if we were to plot the Young population σ_* against that of the Ca T region, we would find that the young σ_* is smaller, on average, than the old population σ_*.

Overall it appears reasonable that the young and old population kinematics can be measured independently in post-starburst galaxies. Furthermore, when measured with an aperture that spans the effective radius, R_e, the kinematics of the young population are consistent with those of the old population. Measurements from smaller apertures may reveal differences in kinematics within the galaxy effective radius.

The post-starburst galaxies measured here appear to be generally consistent with the Faber-Jackson relation, but this depends on the examined population and the canonical relation used for comparison. When considering the relations determined by Nigoche-Netro et al. (2010), the objects appear consistent. However, the r band relation from Desroches et al. (2007) has smaller scatter, and both the young and old population deviate slightly from the relation at the lower luminosities in the sense that they have smaller σ_* values than the relation would predict. These deviations in the young population are rectified after breaking the luminosity into contributions from the young and old populations. However, this also drives the objects above the relation at high luminosities when considering the older population.

Discerning which population is peculiar with respect to the bulge luminosity may require a more detailed look into the internal kinematics of the different populations. We were able to study the major axis kinematics for the object $2337-1058$. This object is undergoing a merger, and both the young and old populations show some rotation.

However, the populations' velocity dispersions are sufficiently high to indicate that the object is pressure supported. The curve of the young population σ_* with respect to position within the galaxy is consistent with results from simulations of major mergers found by Bekki et al. (2005).

Table 2.5: Kinematics of $2337-1058$

Aperture	Velocity Y	Velocity O	σ Young	σ Old	Young template age
01	1.9	14.9	174	81	718
02	31.5	-23.0	194	196	453
03	1.4	-6.2	192	170	453
04	19.7	-19.9	163	179	286
05	19.4	-49.2	139	163	286
06	-14.2	-26.8	140	162	286
07	-35.8	-45.7	143	158	286
08	-35.5	-63.3	155	169	286
09	-52.2	-63.4	189	151	286
10	-45.6	-53.9	194	137	453
11	-67.5	-25.0	143	197	718

Note. — The stellar population systemic velocities and velocity dispersions as measured from five aperture extractions along the major axis of $2337-1058$. Aperture 06 is the central aperture and the other apertures extend in the NE - SW directions. All velocities are presented in km s^{-1}, and the template ages are in Myr.

Chapter 3

Black Hole - Bulge Relationship of Post-Starburst Quasars at $z \sim 0.3$

3.1. Introduction

The $M_{BH} - \sigma_*$ relation (Ferrarese & Merritt 2000; Gebhardt et al. 2000; Gültekin et al. 2009; Woo et al. 2010) has been extensively studied in both active and inactive galaxies at low redshifts. The existence of this and other black hole - host galaxy scaling relations (Magorrian et al. 1998; McLure & Dunlop 2002) implies that the growth of black holes is intimately connected with that of the host galaxies. However, the mechanism by which this growth is regulated is still an open matter.

One proposed mechanism is through black hole accretion feedback. Di Matteo et al. (2005) show that only a modest amount of the accretion energy is required to shut down star formation in the host galaxy. Their simulations of galaxy mergers reproduce the local $\mathrm{M_{BH}} - \sigma_*$ relation with only $\sim 5\%$ of the AGN luminosity being thermodynamically coupled to the surrounding gas. On the other hand, the need for accretion feedback is not clear. Peng (2007) argues that mergers between galaxies (major and minor) naturally leads to a tight log-linear $\mathrm{M_{BH}}$-$\mathrm{M_{bulge}}$ relation. To investigate the co-evolution of black holes with their hosts, it is necessary to measure the relation at higher redshifts.

Robertson et al. (2006) study the theoretical evolution in the $\mathrm{M_{BH}} - \sigma_*$ relation by simulating galactic mergers and including both supernova and black hole feedback. They predict that the slope of the relation remains roughly constant out to redshift $z = 6$, while the scaling of the relation slightly decreases due to an evolving Faber-Jackson relation. The effect of this would be that σ_* increases for a given $\mathrm{M_{BH}}$ as a function of redshift. Conversely, Croton (2006) predicts that the $\mathrm{M_{BH}}$-$\mathrm{M_{bulge}}$ relation evolves in the opposite sense, *i.e.,* black hole mass increases with redshift for a given bulge mass.

Observational investigations into the evolution of the $\mathrm{M_{BH}} - \sigma_*$ relation face difficulties. The sphere of influence of the black hole cannot be resolved at high redshifts, thus the methods using stellar or gas dynamics (Kormendy & Richstone 1995) to measure $\mathrm{M_{BH}}$ in the local universe are unavailable. Alternatively, one can use the virial method to estimate black hole masses, which invokes AGN broad line widths and the $\mathrm{R_{BLR}}$-$\mathrm{L_{5100}}$ relation (Kaspi et al. 2000; Bentz et al. 2009a). However, in type-1 active galactic nuclei (AGN), the active nucleus often outshines the host, drowning out stellar features in the spectra. Despite this effect, Woo et al. (2006, 2008) studied a sample of Seyfert galaxies and found that black holes at $z = 0.36$ and $z = 0.57$ were over-massive for their given stellar velocity dispersions compared to the local relation. Canalizo et al. (2012) avoid the problem of an over-powering AGN continuum by studying dust-reddened quasars between $0.14 < z < 0.37$, which have spectra that show both active nucleus and host galaxy features. They find a result similar to Woo *et al.* in that reddened quasars fall above the local $\mathrm{M_{BH}} - \sigma_*$ relation. The red quasars of Canalizo *et al.* also fall above the $\mathrm{M_{BH}}-\mathrm{L_{bulge}}$ relation, supporting the notion that the black holes are over-massive compared to their bulges.

Other recent studies have discussed regimes in which the local inactive galaxy relation may not hold. Graham et al. (2011) calibrate the $\mathrm{M_{BH}} - \sigma_*$ relation using elliptical, barred and unbarred galaxies and find that the slope of the $\mathrm{M_{BH}} - \sigma_*$ relation can vary according to morphology. Conversely, Beifiori et al. (2011) and Vika et al. (2011) find no correlation between black hole mass and Sérsic index, n. At the low-mass end of the $\mathrm{M_{BH}} - \sigma_*$ relation, Xiao et al. (2011) find little difference in the relation as defined by barred and unbarred Seyfert 1 galaxies. Xiao *et al.* also state that inclination angle of a galactic disk components may increase the scatter of the $\mathrm{M_{BH}} - \sigma_*$ relation. This is consistent with the results of Bennert et al. (2011), who find that σ_* can be biased to larger or smaller values by the disk component of the galaxy. Recently, McConnell et al. (2011a,b) showed that brightest cluster galaxies have black holes that are significantly more massive than predicted from the $\mathrm{M_{BH}} - \sigma_*$ relation given their velocity dispersions.

In this paper we exhibit the first results of our investigation of the $\mathrm{M_{BH}} - \sigma_*$ relation using a sample of AGN whose host galaxies contain luminous post-starburst stellar populations between redshifts $0.2 < z < 0.4$. Brotherton et al. (2012, (in preparation)) catalog a subset of quasars with strong Balmer absorption series visible in their spectra. These "post-starburst quasars" (PSQs) are a convenient case for the study of the $\mathrm{M_{BH}} - \sigma_*$ relation at higher$-z$, because spectra of these objects simultaneously show the broad emission lines distinctive of an active black hole as well as strong stellar absorption lines indicative of a post-starburst stellar population in the host galaxies. The moniker "post-starburst quasars" is not a definitive classification of the objects' luminosities. While some are luminous enough to be considered quasars, others are not. To be consistent with previous work (Cales et al. 2011; Brotherton et al. 2010), we will continue to refer to the sample as "post-starburst quasars".

In this paper we present the stellar velocity dispersions (σ_*) and black hole masses ($\mathrm{M_{BH}}$) of six post-starburst quasars as measured from spectroscopy performed with the Low Resolution Imaging Spectrograph (LRIS) on Keck I. Each of these PSQs were observed with *HST* ACS F606W as part of a snapshot program (10588, PI Brotherton, M.). These images and a detailed morphological study of the host galaxies are presented in Cales et al. (2011). In our analysis we rely on photometry reported by Cales *et al.*, and we adopt the same cosmology that they use: a flat universe with $\mathrm{H_o} = 73$ km s^{-1}, $\Omega_\mathrm{M} = 0.27$, and $\Omega_\Lambda = 0.73$. The paper is organized as follows: we discuss the sample and observations in section 2, describe our spectral fitting code and σ_* measurements in section 3, and discuss virial black hole mass calculations in section 4. We present our main results and discussion of possible biases in sections 5 and 6, respectively.

3.2. Sample and Observations

We present results for six post-starburst quasars from an overall sample of 609 PSQs selected from the Sloan Digital Sky Survey (SDSS) DR3 (Abazajian et al. 2005) that show both strong Balmer series absorptions and broad emission lines. The full details of the sample selection are described in Brotherton et al. (2012, (in preparation)), but see also Cales et al. (2011) and Brotherton et al. (2010). Briefly: objects in the sample have total Balmer equivalent widths $H_{total} = EW_{H\delta} + EW_{H8} + EW_{H9} > 2$ Å. Hϵ was excluded from this measurement, because it can be blended with Ca II. The Balmer break flux ratio was defined by two 100 Å regions starting at restframe wavelengths 3740 and 3985 Å, and the selection criterion was set at $f_{3985\text{Å}}/f_{3740\text{Å}} > 0.9$. The continuum S/N in the SDSS spectra were > 8 as measured between 4150 and 4250 Å.

We observed six post-starburst quasars of the sample using the Low Resolution Imaging Spectrometer (Oke et al. 1995; Rockosi et al. 2010) at Keck I in September 2010. Conditions were excellent with $\sim 0\farcs6$ seeing. We employed both the red and blue side cameras of LRIS to obtain broad spectral coverage. With this coverage we are able to observe the Balmer series (except for Hα and Hβ) of our science targets. We observed several individual stars to construct host galaxy templates on nights in May 2010 and September 2010 using the same instrumental setup as for our science targets.

We observed all of the sample targets with the same setup with LRIS blue and red sides. On the blue side we used the 600/4000 grism, and on the red side we used the 1200/7500 grating. This setup covers observed frame 3100 Å to 6250 Å. Because of the small dispersion in redshift of our science targets, this resulted in slightly different rest-frame wavelength coverage. With this setup we observed the quasar continuum and Mg II emission line on the blue side and the Balmer series on the red side. For one object, SDSS $0237-0101$, we also observed a second red region out to observed frame 7800 Å. For each target we placed a $1''$ observing slit across the nucleus of the object and oriented it according to the parallactic angle. In Fig. 3.1, we show *HST* ACS F606W images of our sample with the LRIS slit over-plotted (proposal 10588; PI: Brotherton, M.). Table 3.1 shows the redshift, exposure times, SDSS r mag, the aperture size used to extract the spectra, and the morphology of each science target.

We followed standard data reduction procedures using the NOAO package in IRAF. First we removed bias levels using the overscan region and cosmic rays from the 2D spectra using the L.A.Cosmic routine (van Dokkum 2001), and corrected for flat fields. We derived a wavelength solution from Hg, Ne, Ar, Cd, and Zn arc lamps and shifted individual spectra taken throughout the night based on sky lines. We fit sky background with a low-order polynomial and subtracted the fit from the 2D spectra. Based on the measurements of Cales et al. (2011), we extracted each spectrum using an aperture width equal to twice the effective radius of the host's bulge component (*i.e.,* center $\pm\mathrm{R}_{\mathrm{eff}}$). This is consistent with what has been done in previous studies (Gebhardt et al. 2000; Bennert et al. 2011) and avoids added uncertainty from aperture corrections when measuring

Table 3.1: Observations

N	Object	redshift	exp time (s)	r [mag]	ap radius ($''$)	morphology
1	SDSS 003043.59 − 103517.6	0.294	1200	18.41	2.52	bulge+disk[1] , barred-spiral
2	SDSS 005739.19 + 010044.9	0.253	1200	17.91	2.28	bulge+disk[1] , spiral
3	SDSS 023700.31 − 010130.4	0.344	2400	18.19	0.22	bulge+disk, spiral
4	SDSS 210200.42 + 000501.9	0.329	2400	18.66	0.98	elliptical
5	SDSS 211838.12 + 005640.6	0.384	1200	18.36	0.44	elliptical
6	SDSS 230614.18 − 010024.4	0.267	1200	18.76	0.26	bulge+disk[1]

Notes:

[1] Objects are in the face-on orientation.

September 2010 Observations. SDSS 0237-0101 was observed with two setups on the red side of LRIS to obtain broad spectral coverage. The blue side was exposed twice for 1200 seconds each for a total of 2400 seconds on the blue side, and 1200 seconds in each of the red side setups. The sixth column shows the extraction aperture radii in arc seconds. These are the bulge effective radii from Cales et al. (2011). The last column describes the basic morphology of the object.

stellar velocity dispersions. We used three standard stars observed throughout the night at parallactic angle to derive a flux calibration with data from Massey et al. (1988) and Massey & Gronwall (1990). We also corrected for Galactic reddening using the extinction values of Schlegel et al. (1998) calculated at sky positions by the NASA Extragalactic Database extinction calculator. We used the IRAF task *deredden*, which uses the extinction function of Cardelli et al. (1989) with the input extinction values to correct the spectra.

We recovered the spectral region from 3100 to 7250 Å with the 600 line mm^{-1} grism and 1200 line mm^{-1} grating blazed at 7500 Å for each template star. The S/N of the template stars spectra was $\geq$1000. Table 3.2 lists the stars and their spectral types used to create host galaxy templates in this project. We conducted the same data reduction procedures on the observed template stars as on the post-starburst quasars with the additional step of correcting for observed radial velocities.

The blue and red sides of LRIS have different spectral resolutions. The Balmer series fell on the blue side of LRIS for the template stars, but was shifted to longer wavelengths for the quasars in the sample. Before combining our spectra and fitting, we convolved the red side of the quasar spectra with a Gaussian to match the resolution of the blue side. We achieved an intrinsic resolution of $\sigma = 90$ km s^{-1} for the lowest redshift object (SDSS 0030 $-$ 1035; z=0.253) at rest-frame 3839 Å. We achieved resolution of σ= 82 km s^{-1} for the highest redshift object (SDSS 2118$+$0056; z=0.384) at rest-frame 3475 Å.

Table 3.2: Template Stars

Star	Sp Type
HD 93700	A0
HD 94980	A3
BD +182402	A5
HD 95002	F0
BD +182401	F5
HD 95958	F8
HD 97127	G0
HD 95676	G5
HD 184850	G8
HD 95437	K0
HD 230519	K2
HD 347822	K2
HD 347838	K5
HD 96761	K5
HD 347857	K7
BD +212255	M0
GSC 01562 − 00224	M8

Note. — In the cases where the same spectral type is repeated we used an average of the two stars for the host galaxy templates.

3.3. Stellar Velocity Dispersion

3.3.1. Fitting Code

To measure the stellar velocity dispersion of each host galaxy, we follow a direct fitting method that has been used extensively in previous studies. Barth et al. (2003) use the direct fitting method to fit the spectra of BL Lac objects. More recently it was employed by Xiao et al. (2011) to fit a sample of Seyfert 1 host galaxies, and by Greene et al. (2010b) to fit the spectra of H_2O megamasers. Canalizo et al. (2012) use the method to fit the host galaxies of dust-reddened quasars.

We model the spectra with contributions from both the host galaxy and the active nucleus. The host template is constructed with a composite of stellar spectra taken with the same instrumental setup (see § 3.2 for details) and broadened with a Gaussian in order to simulate the stellar velocity dispersion of the host galaxy. We include a power-law continuum attributed to the intrinsic active nucleus spectrum. We also include a Legendre polynomial that characterizes non-stellar emission in the spectra, including Fe emission and reddening effects. The polynomial makes no assumption regarding the reddening law (*e.g.,* SMC). Thus, the full model function used in the fitting takes the form:

$$M(x) = \{[T(x) \otimes G(x)] + C(x)\} \times P(x) \tag{3.1}$$

where T(x) is the host galaxy stellar template, G(x) is a Gaussian, C(x) is a power-law continuum ($\log(f) = c_1 + c_2 * \log(\lambda)$), and P(x) is a third order Legendre polynomial.

The fitting is performed in velocity space (logλ). There are a total of nine free parameters: the Gaussian velocity dispersion, an offset velocity between the model and the data, the power-law continuum scaling and slope, the four coefficients of the Legendre polynomial, and the relative flux contribution of an "old" and "young" host galaxy population. The "young" population template represents the post-starburst component separate from the older population of the host galaxy (see below).

The fitting code uses the amoeba routine from Numerical Recipes (written for IDL by W. Thompson) to minimize the χ^2 function. The inputs of the amoeba routine are the observed galaxy, the template model to fit, and the error for each datum in the observed galaxy spectrum. We created artificial errors to weight our data, focusing the fitting region on the Balmer series. To block emission lines from the fit, we set the pixel errors to a value several orders of magnitude larger than the error on the unblocked regions. Thus these emission lines do not contribute to χ^2, and are ignored during the minimization.

3.3.2. Templates

We must be careful in defining a host galaxy template that correctly matches the stellar population of the galaxies. A template mis-match from the stellar population of the host galaxy may cause an incorrect measure of the velocity dispersion. Mismatch between the host stellar population and the template composition can be a source of error in the direct fitting method (Greene & Ho 2006; Barth et al. 2002). Furthermore, the Balmer lines of early type stars are intrinsically broadened by the combined effects of turbulence in the stellar atmosphere, axial rotation, and pressure broadening of the energy levels within the hydrogen atoms. This intrinsic broadening may bias our measured σ_* if we were to use a host template that did not include early type stars. As long as the templates used in the direct fitting include early type stars with luminosity weighted proportions that mimic the galaxy stellar population, then the broadening function simulates the kinematics of the host galaxy, not the intrinsic line widths.

We set out to create host galaxy templates that matched the stellar populations in the host galaxies, including the early-type stars. To do this we collected spectra of a set of stars ranging across 15 spectral types from A0 through M8. The spectral range covers $3100 - 7200$ Å.

We simulate single-epoch starburst models by determining the luminosity weighted proportions of each spectral type that contribute to individual models. We produced a series of templates to compare to the instantaneous burst models of Charlot & Bruzual (private communication, see also Bruzual 2007). The series begins with weights favoring early type stars to simulate a young stellar population, then progresses by removing the earliest spectral types and weighting the rest of the stars accordingly. When compared with the starburst models of Charlot & Bruzual, this simulates a range of starburst ages by "evolving" early type stars out of the template.

We compared the Charlot & Bruzual models to each template produced in the series as well as to the individual stars that were included in the templates. Using the χ^2 statistic as an indicator of the goodness-of-fit, we identified nine unique matchings between the Charlot & Bruzual models and our templates. We note that we only calculated χ^2 across the spectral fitting region 3600 - 4800 Å in order to obtain the best match in the region of interest, but the templates generally matched the Charlot & Bruzual models well at longer wavelengths as well.

Thus, we produced spectral templates that match stellar populations of ages 321 Myr, 404 Myr, 570 Myr, 640 Myr, 718 Myr, 904 Myr, 4.0 Gyr, 6.0 Gyr and 9.0 Gyr. The 321 Myr model was best matched with a single A0 star. The 404 Myr model was best matched with a single F0 star. The 6 Gyr and 9 Gyr models were best matched by G5 and G8 stars, respectively. The remaining models were best fit by templates that included all spectral types from our library with proportions weighted by luminosity toward early type stars.

3.3.3. Fitting Procedure

While the host galaxies show a strong post-starburst component, they also contain an older stellar population. The observed line widths can be fitted using the Gaussian function, but the line strengths, ratios, and continuum shape will be determined by the age of the post-starburst population and its relative contribution to the overall flux. For this reason, we adopt a procedure that tests each of the templates that we created and by doing so determine an approximate age of the starburst population. The best fitting templates were combinations of the 9 Gyr template (a single G8 star) with templates that were $<$ 1 Gyr old. We allowed the relative contribution of the "old" and "young" populations to be a free parameter. The final values of the parameters can be sensitive to their initial values. This is because the χ^2 value can converge on a local minimum within the parameter space. To ensure we obtain a robust result that converges on the global minimum, we re-fit the spectra after perturbing the input parameters. We present the measured velocity dispersions (σ_*), luminosity-weighted fraction of the starburst component, 95% confidence interval of σ_*, and the age of the younger starburst template in Table 3.3.

To determine the 95% confidence interval of our σ_* measurements, we re-fit the spectra holding σ_* constant across the range ± 30 km s^{-1} from the best fit σ_* in intervals of 5 km s^{-1}. We inspected the resulting χ^2 versus σ_* plot to ensure that the measured σ_* was indeed the value that minimized χ^2, and we fit a parabola through the values in order to define more precisely the confidence interval. The 95% confidence interval is defined as the range in σ_* that increases the χ^2 value by 4 (Press et al. 2007).

Figure 3.2 shows the best fits obtained for our targets. The observed spectra are plotted in black. The best fit model is over-plotted in red, and the residuals are plotted in blue.

We obtained an additional longer wavelength spectrum that extends to rest frame 5800 Å for the object SDSS $0237-0101$. We fit the spectral region around Mg Ib with the expectation that features from the underlying older stellar population would be dominant in this region. The exact region was from $5020-5550$ Å with one emission line at 5198 Å blocked from the fit. Fitting this region can be complicated due to [Mg/Fe] correlation with velocity dispersion (Jørgensen et al. 1999; Wold et al. 2007). However, we found identical results between fits conducted with and without the Mg Ib absorption blocked from the fit. Despite some effort in matching the templates to the

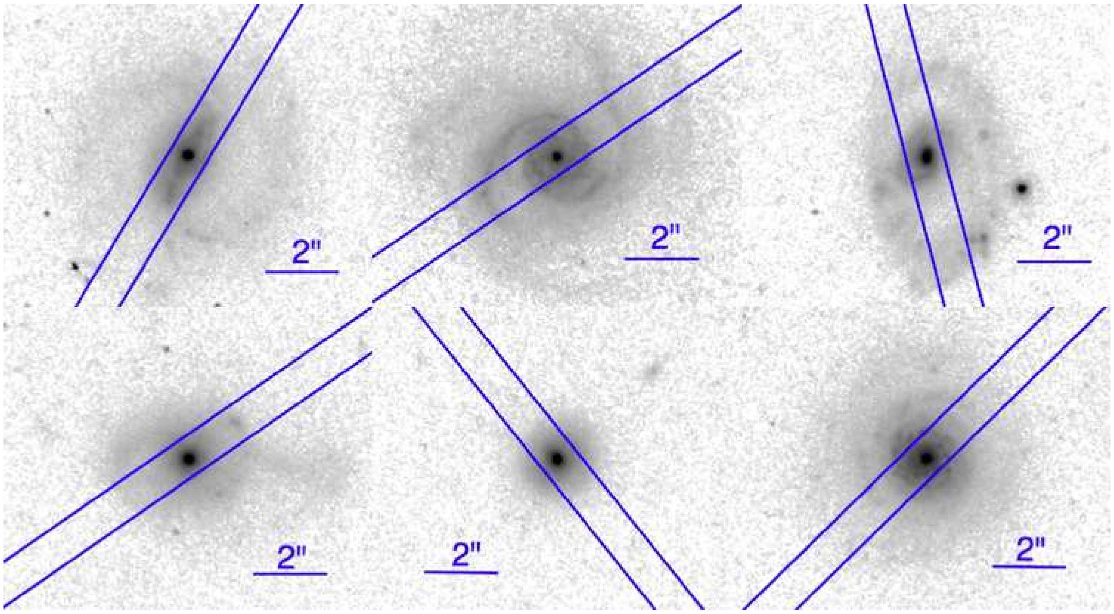

Fig. 3.1.— HST ACS F606W images of our sample (Proposal ID 10588; PI: Brotherton, M.). North is up and East is to the left in each of the images. The LRIS slit was placed at parallactic angle with a 1″ width. *Top*: 0030 − 1035, 0057 + 0100, and 0237 − 0101. *Bottom*: 2102 + 0005, 2118 + 0056, and 2306 − 0100.

Table 3.3: Best Fit Parameters

N	Object	σ_*	SB	95% low-high	younger population age
1	SDSS 003043.59 − 103517.6	73	99	44 − 79	718 Myr
2	SDSS 005739.19 + 010044.9	134	33	126 − 146	321 Myr
3	SDSS 023700.31 − 010130.4	214	79	209 − 233	640 Myr
4	SDSS 210200.42 + 000501.9	162	86	154 − 166	404 Myr
5	SDSS 211838.12 + 005640.6	134	63	118 − 137	404 Myr
6	SDSS 230614.18 − 010024.4	54	86	34 − 61	570 Myr

Note. — The velocity dispersions are shown under the column labeled σ_* and have units km s^{-1}. Velocity dispersions reported here have not been corrected for the aperture. The column labeled SB are the fractional contribution of the star-burst component to the total flux shown as percentages. The lower and upper limits of the 95% confidence interval is shown with units km s^{-1}. In the last column we report the age of the template used to represent the young stellar population.

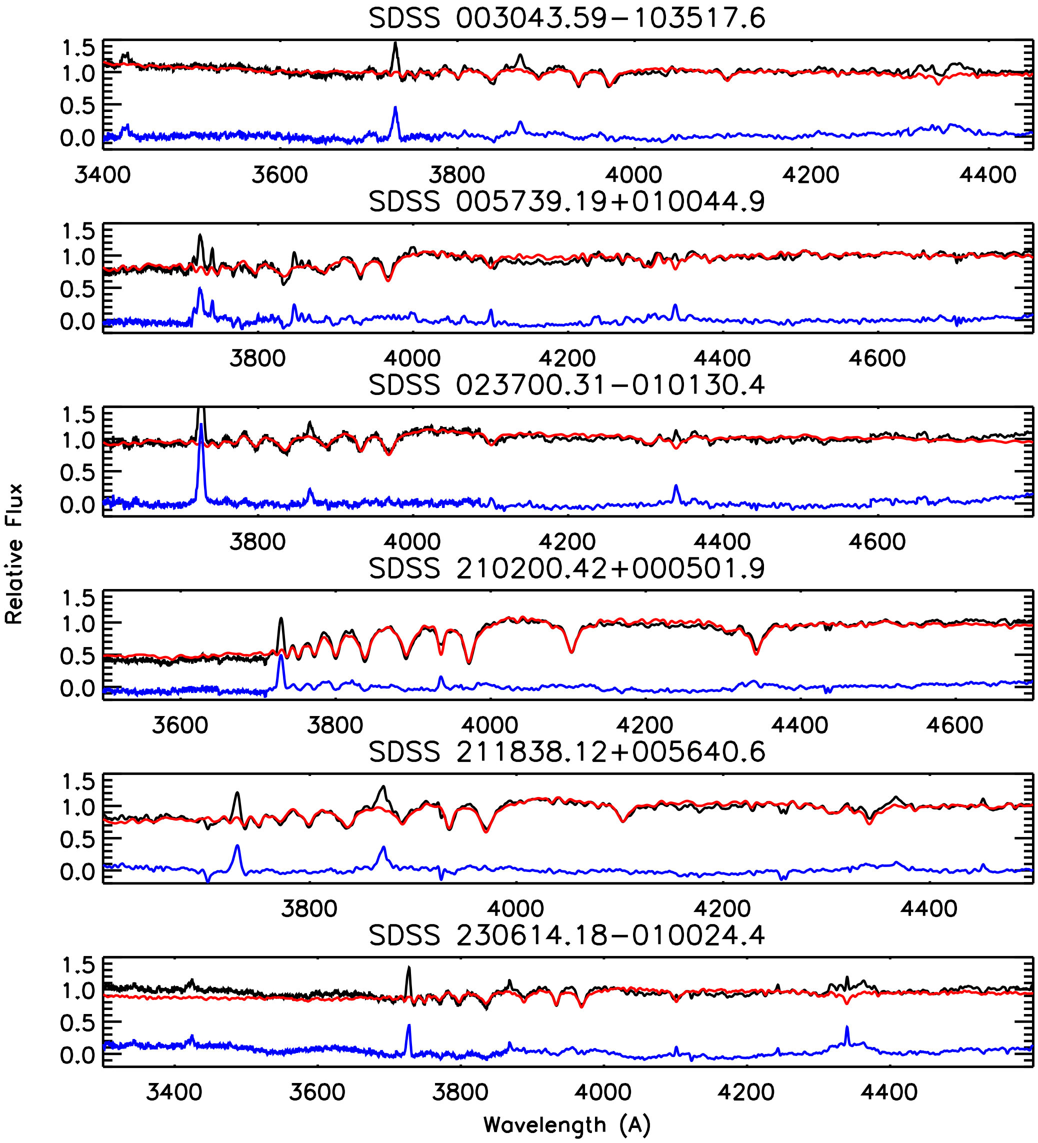

Fig. 3.2.— Spectral fitting results. The data are plotted in black, the best fit model in red, and the residual is plotted in blue. Each spectrum is plotted in the rest frame.

host galaxy and using various weighting schemes, we were unable to derive a robust measure of σ_* from this region. The best fit dispersion using this region was 155 (+19, −18) km s^{-1}, which is smaller than the dispersion measured from the Balmer region, i.e., 214 (+19, −5) km s^{-1}). However, we were able to fit σ_* values that ranged from $\sim 145 \sim 210$ km s^{-1} while still maintaining visually similar fits. In Figure 3.3, we show example fits for this region using σ_* values of 145 km s^{-1}, 175 km s^{-1}, and 210 km s^{-1}. As in Figure 3.2, the data are plotted in black, and the models are plotted in red. The residuals for the three fits shown are similar to one another. These fits indicate that there are likely model degeneracies that are affecting the determination of σ_* in this region.

3.4. Black Hole Mass

Black hole masses can be estimated using the virial method under the assumption that the broad line region (BLR) gas is virialized. To calculate the virial parameter, we require measurements of the gas velocity and orbital radius. The velocity is, in principle, easily measured from broad line widths (*e.g.,* Mg II, Hβ, Hα). Furthermore, reverberation mapping studies have shown a correlation between the radius of the BLR ($R_{\rm BLR}$) and the continuum luminosity of the active nucleus (Kaspi et al. 2000; Bentz et al. 2009a). Thus, the observables to employ the virial method are the line width and continuum luminosity.

To convert the virial parameter ($VP = R_{\rm BLR}\Delta v^2/G$) to a black hole mass, one must include an additional *f*-factor, which accounts for unknown geometries in the broad line

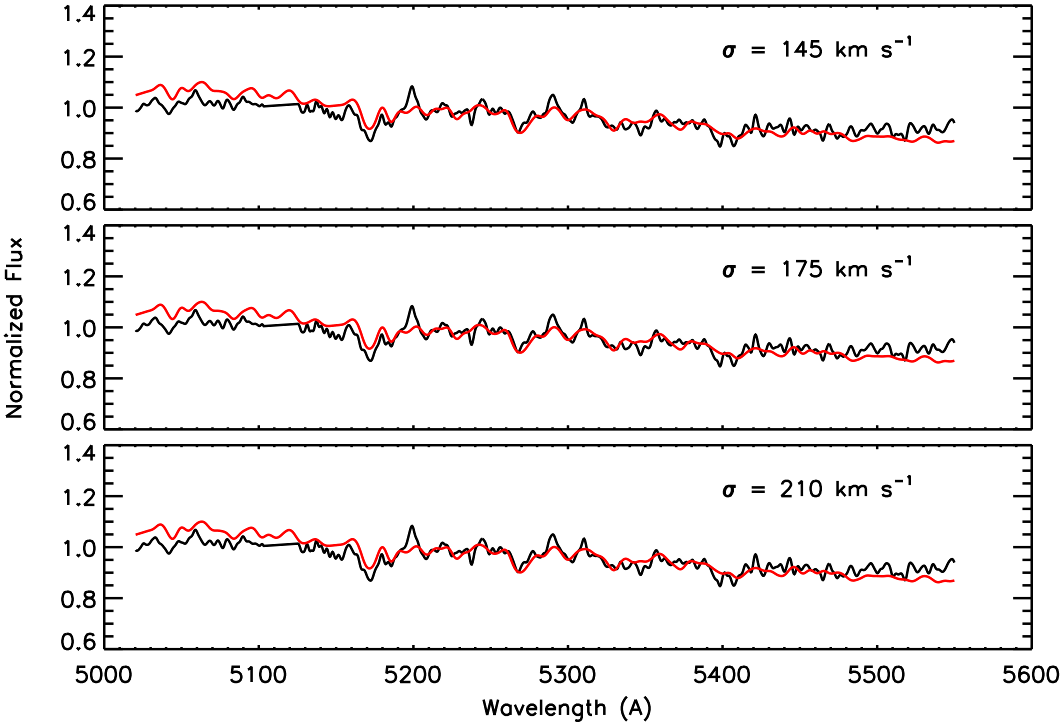

Fig. 3.3.— Spectral fitting results for the Mg Ib region of SDSS 0237 − 0101. We have plotted the best fits for three values of σ_*: 145, 175, and 210 km $^{-1}$. The data are plotted in black, the best fit model in red.

region. Woo et al. (2010) have measured this factor by scaling the virial parameter of reverberation mapped AGN to match the $M_{BH} - \sigma_*$ relation, and found $f = 5.2$. This is consistent with values found by previous authors (Onken et al. 2004) that are about 1.8 times higher than an f-factor assuming an isotropic BLR velocity field.

In the following sections we describe how we measured the broad line widths and continuum luminosities used in the virial black hole mass calculation. We measure the Hα FWHM, and the Mg II $\lambda\lambda 2796, 2803$ FWHM to use as BLR gas velocities. We measure the 5100 Å AGN continuum luminosity to use as a proxy for the BLR radius. In the following we will refer to λL_λ as L_{3000} or L_{5100} for $\lambda = 3000$ Å and $\lambda = 5100$ Å, respectively. Table 3.4 displays the relevant measurements. Table 3.5 shows the mass estimates and Eddington ratios.

3.4.1. Hα

The Hβ broad emission line is often used to calculate black hole masses in single-epoch spectra of AGN. However, in our sample, the absorption-line spectrum of the host galaxy can significantly contaminate the Hβ emission line. Often the broad Hβ line is completely unobserved, so Hβ emission is not suitable for measuring M_{BH}. On the other hand, Hα is much less affected by the stellar absorption line than Hβ, and broad Hα is always observed in the spectra of the targets.

To calculate black hole masses we adopt the relation from Greene et al. (2010a):

$$\mathrm{M_{BH}} = (9.7 \pm 0.5)\text{x}10^{6}(\frac{\mathrm{L_{5100}}}{10^{44}\ \mathrm{erg\ s^{-1}}})^{0.519\pm0.07}$$

$$\text{x}(\frac{\mathrm{FWHM_{H\alpha}}}{10^{3}\ \mathrm{km\ s^{-1}}})^{2.06\pm0.06}\ \mathrm{M_{\odot}} \tag{3.2}$$

Greene *et al.* use a virial coefficient from Onken et al. (2004) (*f*= 5.5), which is 1.8 times higher than the assumption of isotropic random motions. Their equation was originally determined by Greene & Ho (2005), who derive a conversion between Hα and Hβ FWHM. Thus, the above equation converts the Hα FWHM to that of Hβ, and uses an *f*-factor appropriate for Hβ.

Woo et al. (2010) measure the $\mathrm{M_{BH}} - \sigma_*$ relation for the reverberation mapped sample of the Lick AGN Monitoring Project (Walsh et al. 2009; Bentz et al. 2009b, 2010). Woo *et al.* determine the geometric factor for *f*= $5.2^{+1.2}_{-1.3}$ by scaling the determined Hβ virial products to the local $\mathrm{M_{BH}} - \sigma_*$ relation for inactive galaxies determined by Gültekin et al. (2009). Because the relation from Greene et al. (2010a) uses the same virial coefficient as found by Woo *et al.*, any differences we find between our sample and that of Woo *et al.* will not be due to differences between *f*-factors.

To measure the widths of the Hα broad emission line we used the task *specfit* in the STSDAS package of IRAF (Kriss 1994). Our LRIS spectroscopy does not cover the Hα region, so we measure the width from the SDSS spectra (DR7; Abazajian et al. 2009). The task *specfit* minimizes the χ^2 using a simplex method and returns the central wavelength, integrated flux, FWHM, and skew of each line. We fit the region from 6400 - 6700 Å using five components: a power law continuum, three Gaussians for the narrow line components of [N II] λ6548, Hα, and [N II] λ6583, and an additional Gaussian for the Hα broad emission line. We held the relative positions of the [N II] lines constant for the fitting procedure, and constrained all the Gaussians to be symmetric. We fit a narrow line model using [O III] 5007 on objects where the line was visible and scaled the model to the [N II] and Hα narrow lines. The *specfit* task also returns errors on the fitted parameters, which are generally large due to the resolution and S/N of the SDSS spectra. We show the fits of the Hα region for all objects in Fig. 3.4.

The stellar Hα absorption line from the host galaxy is small compared to each of these components, and significantly more narrow than the broad emission line of the active nucleus. Using spectra and host galaxy fits for PSQs from Cales et al. (2012, (in preparation)) that cover Hα, we determined that the host galaxy absorption component does not affect the measurement of the broad line FWHM.

The data of Cales et al. (2012, (in preparation)) cover the Hα region for the object SDSS $0057 + 0100$, and have higher resolution and S/N ($\sim$28 pix^{-1} on the continuum) than the SDSS spectrum (S/N$\sim$10 pix^{-1} on the continuum). Following the same procedure, the FWHM measured using these data agrees within the errors of the FWHM measured from the SDSS spectrum. We adopt the width measured with the data from Cales *et al.*, because the S/N is an improvement over the SDSS spectrum.

3.4.2. Mg II

As with the Hα emission line, there are several prescriptions for calculating black hole masses from the Mg II $\lambda\lambda 2796, 2803$ broad emission doublet (McLure & Jarvis

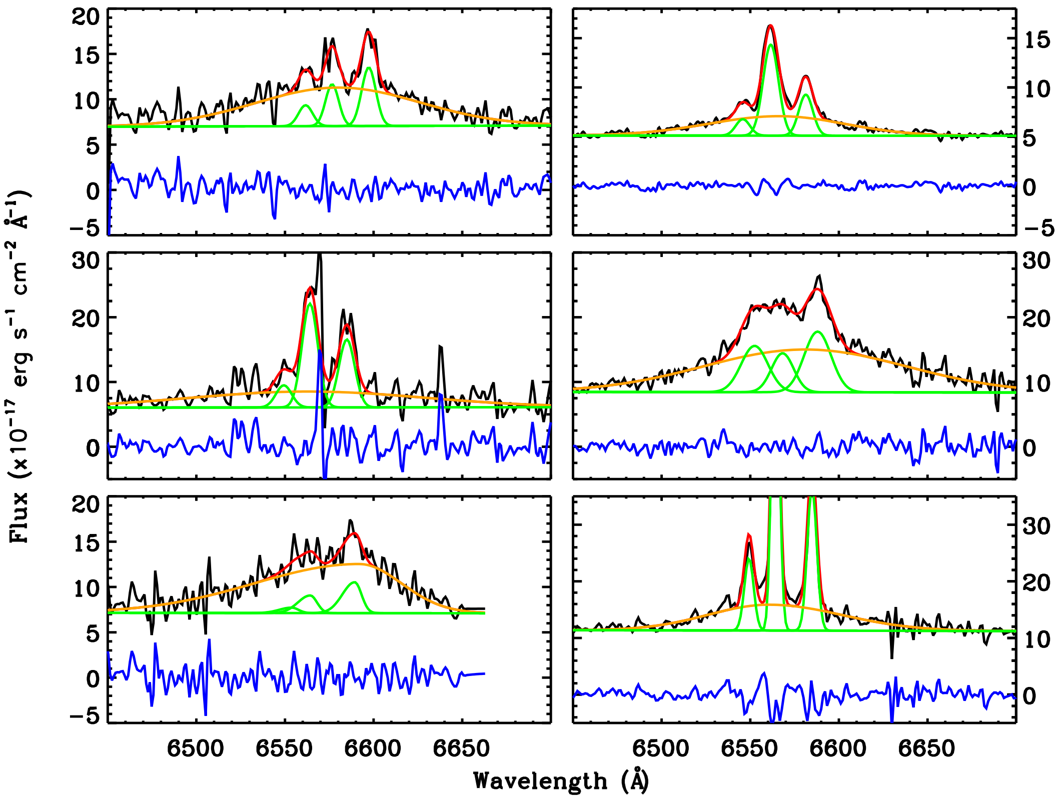

Fig. 3.4.— Broad- and narrow-line decompositions of the Hα region. The SDSS DR7 spectra are plotted in the restframe in black. The models of the narrow emission lines and continuum are plotted in green, and the Hα broad emission line component is plotted in orange. The overall fit is plotted in red. The residuals are plotted in blue. The objects in the left column from top to bottom are $0030 - 1035$, $0237 - 0101$, and $2118 + 0056$. The objects on the right are $0057 + 0100$, $2102 + 0005$, and $2306 - 0100$.

2002; McGill et al. 2008; Rafiee & Hall 2011; Vestergaard & Osmer 2009). Of these, the calibration from Vestergaard & Osmer (2009) is based on the largest number of objects and is calibrated with L_{5100} in addition to other continuum luminosities. As described in the next section, we consider the 5100 Å continuum luminosity to be better constrained than the 3000 Å luminosity, which is typically used in conjunction with the Mg II emission to calculate black hole masses. The formulation that we adopt from Vestergaard & Osmer is:

$$\mathrm{M_{BH}} = 10^{6.96}(\frac{\mathrm{FWHM_{MgII}}}{1000\mathrm{kms^{-1}}})^2(\frac{\mathrm{L_{5100}}}{10^{44}\mathrm{ergs^{-1}}})^{0.5}\ \mathrm{M_\odot} \tag{3.3}$$

According to Vestergaard & Osmer, the uncertainty in the zero point of this relation is 0.55 dex. This is the dominant factor in the uncertainty on the black hole mass calculated from the Mg II emission.

To measure the Mg II width, we first fitted and subtracted an Fe II emission template from the spectrum. Iron emission can contaminate the flux surrounding the Mg II emission and affect the measurement of the broad line width. We used the template from Vestergaard & Wilkes (2001), who derived the template from the observed spectrum of the narrow-line Seyfert 1 galaxy I Zw 1.

The template by Vestergaard & Wilkes (2001) only includes Fe emission that may contaminate the wings of the Mg II profile. To account for Fe emission that may contaminate the core of the line, Fine et al. (2008) and Kurk et al. (2007) add a constant flux under the Mg II core equal to 20% of the average Fe flux at $2930 - 2970$ Å. This is based on the theoretical Fe emission models of Sigut & Pradhan (2003). To determine if the theoretical flux may have affected our Mg II width measurements, we subtracted the additional flux from the fit of SDSS $0237-0101$ and re-measured the width of the Mg II emission. There was no difference measured between the two methods, so we do not believe this small amount of theoretical flux has affected the measurements of Mg II widths.

We used a fitting routine similar to the one that we used to determine stellar velocity dispersions to scale and broaden the Fe template before subtraction. The main differences between the way that we modeled the Balmer region and the Mg II region are that we replaced the host galaxy stellar template with the Fe template from Vestergaard & Wilkes (2001) and the fitted continuum includes contributions from both the active nucleus and host galaxy at these wavelengths. We adopted a power law to fit the continuum, as we expect that the host galaxy contribution to the flux at these wavelengths is comparatively small. We fit a total of five parameters: normalization and slope for a power law continuum, and the scaling constant, velocity dispersion (σ_{Fe}), and velocity offset for the Fe template.

We first estimated the continuum from a region relatively uncontaminated by Fe emission: $3010-3026$ Å. The result was used as the continuum initial estimate for the main fitting routine. The Fe template does not include the Mg II emission line, so we blocked the feature from contributing to the χ^2 during the minimization. This region varied in size for each object depending on the strength of the emission. We allowed σ_{Fe} to vary up to 2000 km s^{-1}, but each fit produced a value smaller than 1000 km s^{-1}.

The best fit model was then subtracted from the spectrum leaving a residual spectrum. We show Fe template fits to all objects in Fig. 3.5.

Objects SDSS $0057 + 0100$ and SDSS $2102 + 0005$ were peculiar, and were not fit well by the Fe template (first and second object on the right side of Fig. 3.5). The spectrum of SDSS $0057 + 0100$ shows some signs of absorption to the blue side of Mg II. However, the noise significantly increases at the edge of the spectrum, making the continuum level difficult to determine. It is possible that SDSS 0057+0100 is a low-ionization broad absorption line (LoBAL) quasar, but without a clear determination of the continuum level at shorter wavelengths, we hesitate to classify it as such. In order to fit the Fe template to this object, we blocked the wavelength region shortward of and including the Mg II emission (< 2840 Å) from the fit, allowing the overall fit to be determined by the longer wavelengths. Then we subtracted the entire fitted spectrum from the region before measuring the Mg II width. The spectrum of SDSS $2102 + 0005$ has better S/N on the blue side of Mg II than that of SDSS $0057 + 0100$, and the profile of Mg II makes it clear that the object is a LoBAL. Because the spectrum shows strong absorption over the blue wing of the Mg II line, we were unable to reliably measure a Mg II line width. We do not report a Mg II width measurement for SDSS $2102 + 0005$, but do include one for SDSS $0057 + 0100$.

3.4.3. Continuum Luminosities

The continuum luminosity is used as a proxy for the BLR radius in the virial method to measure black hole mass. We measure the continuum luminosity from the power-law

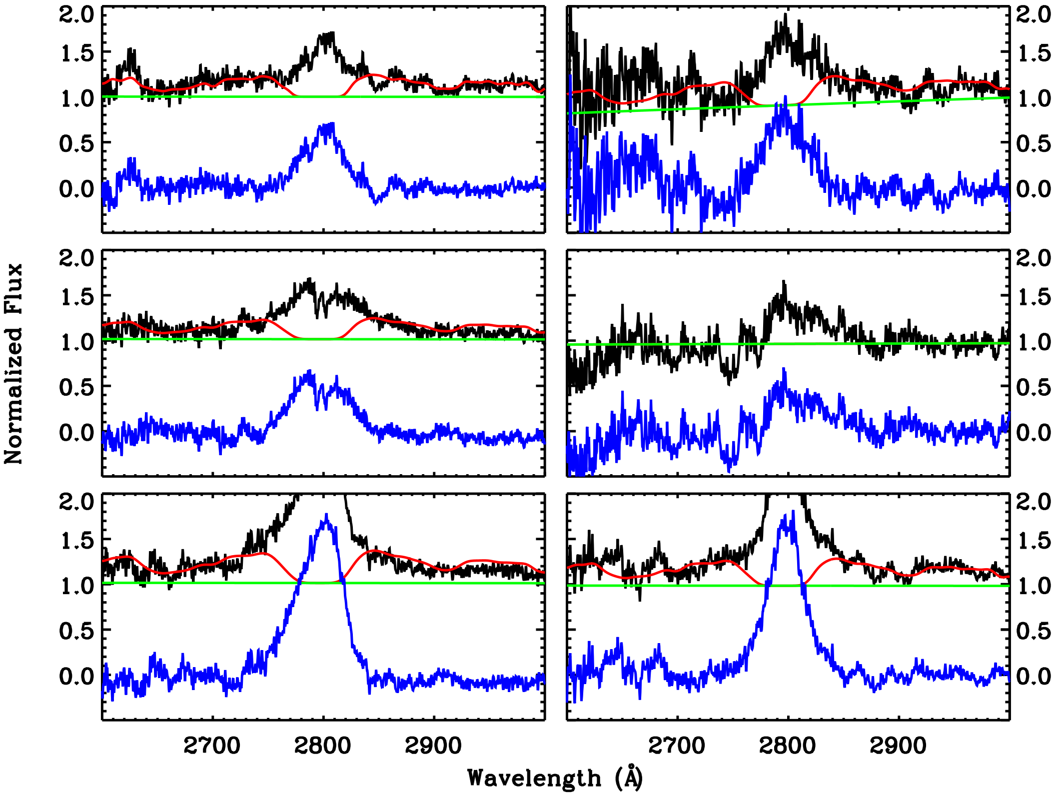

Fig. 3.5.— Fe template fitting in the Mg II region. The LRIS data are plotted in black. The overall fitted Fe template is plotted in red, and the continuum is plotted in green. The residual spectrum (data - model) is plotted in blue. The objects are in the same order as Fig. 3.4

continuum of our model. The power-law is multiplied by a Legendre polynomial to simulate reddening effects and non-stellar emission, and the product of the continuum and Legendre polynomial represents the reddened nucleus free of host contamination. In order to obtain the intrinsic continuum luminosities we follow a two step process: First, we calculate a scaling factor between the product of the continuum and Legendre polynomial fitted by our spectral code and the *HST* F606W photometry of the nucleus, which has been deconvolved from the host galaxy (Cales et al. 2011). The scale factor effectively flux calibrates our fitted spectrum to the *HST* photometry. Then we apply the scaling factor to the fitted underlying power law continuum (without the Legendre polynomial).

We measure the monochromatic luminosities from the scaled power law. It is important to note that both 3000 Å and 5100 Å fall outside the spectral region that we modeled. Thus, the luminosites are extrapolations from our fitted quasar power-law continuum. We define uncertainty on the continuum luminosities by varying the slope of our intrinsic continuum by ±0.1, which is the scatter in the average quasar spectral slope (Vanden Berk et al. 2001). The emission at 3000 Å has contributions from the active nucleus, the host galaxy, and iron. While we have a template that models the iron emission (Vestergaard & Wilkes 2001), attempting to separate the three components would include many free parameters and model degeneracies may become a significant issue. Furthermore, the photometry that we use to scale the fitted active nucleus spectrum is in the observed *HST* F606W filter. Because 5100 Å is much closer to both our spectral fitting region and the F606W photometry, we consider L_{5100} to be much better constrained than L_{3000}. We present both measured luminosities and their formal uncertainties in Table 3.4. The true uncertainty for the L_{3000} measurement is larger than the formal uncertainty that we have reported for the reasons noted above.

3.5. Results

In the previous sections we have presented our σ_* and M_{BH} measurements of six PSQs. We now examine the relationship between the black holes and their host bulges through the $M_{BH} - \sigma_*$ and M_{BH}–L_{bulge} relations. We further examine the properties of the host galaxy bulges with the Faber-Jackson relation to determine if the bulges are dynamically peculiar compared to evolved systems in the local universe. By examining these three relations, we can determine if any observed offset is primarily due to over/under-massive BHs or dynamically perturbed bulges.

Using the Hα and Mg II emission line widths, we calculated masses of the black holes in six post-starburst quasars and present the values in Table 3.5. In five of the six objects, we measure larger masses based on the Hα broad line than the Mg II broad line. We were unable to measure the M_{BH} based on the Mg II broad line for SDSS $2102 + 0005$, because the line profile for this object is affected by an absorption trough on the blue wing, as described above.

The relations from Greene et al. (2010a) and Vestergaard & Osmer (2009) are each calibrated to Hβ. In principle they should give consistent results, because the two prescriptions are measuring the same black hole mass, and both Hα and Mg II should be reliable indicators of the BLR gas dynamics and M_{BH}. That is, according to

Greene & Ho (2005), the correlation between the Hα FWHM and the Hβ FWHM has a scatter on the order of ~ 0.1 dex. Furthermore, Vestergaard & Osmer (2009) report their calibration produces Mg II-based masses that are consistent with the Hβ and C IV-based masses within ~ 0.1 dex. However, the 1σ scatter on the zero point of the Vestergaard & Osmer relation is 0.55 dex. If we consider this large error associated with the Mg II-based calculation, then our calculated Hα and Mg II masses are consistent. The discrepancy could arise if, at least for PSQs, the geometric *f*-factor were different between the emission line gas species. This is not unlikely, as magnesium has a lower ionization potential than hydrogen, and may arise from a different location within the BLR.

3.5.1. The $\mathrm{M_{BH}} - \sigma_*$ Relation

We have plotted the objects studied here on the $\mathrm{M_{BH}} - \sigma_*$ diagram (Fig. 3.6). For comparison we present the relation measured by McConnell et al. (2011a), who update the plot with compiled measurements from the literature. We also include reverberation mapped AGN from Woo et al. (2010). The best fit from McConnell *et al.* is plotted as a dot-dashed line, and the fit from Woo *et al.* is plotted as the dashed line. We plot the Hα based black hole masses in red triangles. The scatter reported by both McConnell *et al.* and Woo *et al.* is ~ 0.43 dex, and the Hα based $\mathrm{M_{BH}}$ all fall within or above this scatter with respect to either relation. Three of the black hole masses that were based on the Mg II measurement are consistent with this scatter.

Table 3.4: Line Widths and Monochromatic Luminosities

N	Object	Hα FWHM	σ_{intr}	Mg II FWHM$_{intr}$	L$_{3000}$ 3000 Å	L$_{5100}$ 5100 Å
1	SDSS 003043.59 − 103517.6	4981 ± 428	1563	3066	$4.7^{+1.7}_{-1.2}$	$1.5^{+0.6}_{-0.4}$
2	SDSS 005739.19 + 010044.9	4300 ± 210	1871	3464	$0.36^{+0.07}_{-0.06}$	$0.30^{+0.08}_{-0.06}$
3	SDSS 023700.31 − 010130.4	7125 ± 770	2357	4855	$0.39^{+0.2}_{-0.1}$	$0.41^{+0.2}_{-0.1}$
4	SDSS 210200.42 + 000501.9	6132 ± 315	···	···	$0.58^{+0.08}_{-0.07}$	$0.79^{+0.06}_{-0.06}$
5	SDSS 211838.12 + 005640.6	6303 ± 501	2278	2913	$1.4^{+0.4}_{-0.3}$	$1.7^{+0.3}_{-0.5}$
6	SDSS 230614.18 − 010024.4	3704 ± 719	1857	2468	$1.1^{+0.7}_{-0.4}$	$1.2^{+1.2}_{-0.4}$

Note. — Widths are presented with units km s^{-1}, and luminosities are presented with units x10^{44} erg s^{-1}. The Hα FWHM have been corrected for the instrumental resolution of the SDSS using R= 2000. The Mg II widths have been corrected for the instrumental resolution of LRIS. Instrumental resolution had a small effect on the widths compared to the errors. Errors on the luminosities were determined by varying the fitted slope by ±0.1.

Table 3.5: Black Hole Masses

N	Object	M$_{\rm BH}$ Hα	M$_{\rm BH}$ Mg II	L$_{bol}$/L$_{Edd}$ 5100 Å	L$_{bol}$/L$_{Edd}$ [O III]
1	SDSS 003043.59 − 103517.6	$3.25^{+3.0}_{-1.5}$	1.1	0.037	0.019
2	SDSS 005739.19 + 010044.9	$1.06^{+1.1}_{-0.5}$	0.60	0.023	0.076
3	SDSS 023700.31 − 010130.4	$3.49^{+4.0}_{-1.8}$	1.4	0.009	0.057
4	SDSS 210200.42 + 000501.9	$3.59^{+3.2}_{-1.7}$	···	0.018	0.013
5	SDSS 211838.12 + 005640.6	$5.70^{+5.0}_{-2.6}$	1.0	0.024	0.027
6	SDSS 230614.18 − 010024.4	$1.56^{+1.9}_{-0.8}$	0.60	0.060	0.062

Note. — Units of the black hole masses are x10^{8} M$_{\odot}$ and were calculated from the equations of Greene et al. (2010a) and Vestergaard & Osmer (2009). Errors on the Mg II-based black hole masses are dominated by the calibration zero point error ($\sim$ 0.55 dex). Eddington ratios assume bolometric correction factors of 10 for the 5100 Å luminosities (Woo & Urry 2002), and 3500 for the [O III]λ5007 luminosities, respectively.

The objects SDSS 0030−1035 and SDSS 2306−0100 appear significantly offset from the $\mathrm{M_{BH}} - \sigma_*$ relation. Both of these galaxies were classified by Cales et al. (2012) as face-on disks. The face-on disk presents a dynamically cold stellar component with small line-of-sight velocity dispersion, and Bennert et al. (2011) showed that this orientation can bias the measured velocity dispersion toward smaller values. The sample of Woo et al. (2006) contains four face-on disks, and the objects do have lower σ_* values than the remainder of their sample. However, the magnitude of the bias for their objects is only $\sim 30 - 50$ km s^{-1} ($\Delta\sigma_* \sim 0.1$ dex), whereas the two objects here have offsets on the order of ~ 140 km s^{-1} ($\Delta\sigma_* \sim 0.6$ dex). Furthermore, as we show below, one of these objects is consistent with the Faber-Jackson relation.

One other object in our sample was classified by Cales et al. (2012) as a face-on disk (SDSS $0057 + 0100$), but it falls within the scatter of the $\mathrm{M_{BH}} - \sigma_*$ relation. SDSS $0237 - 0101$ also has a bulge+disk morphology, but is not face-on and falls within the scatter of the $\mathrm{M_{BH}} - \sigma_*$ relation. The last two objects (SDSS $2102 + 0005$ and SDSS $2118 + 0056$) are dominated by bulges and fall outside the defined 1σ scatter of the $\mathrm{M_{BH}} - \sigma_*$ relation.

In Fig. 3.7 we show the offset of $\mathrm{M_{BH}}$ (*top panel*) and the offset of σ_* (*bottom panel*) from the relation defined by Woo et al. (2010) as a function of z. Previous studies have found an offset from the local $\mathrm{M_{BH}} - \sigma_*$ relation, including Woo et al. (2006, 2008) and Canalizo et al. (2012). The objects in our sample span a redshift range that overlaps with the samples of Canalizo *et al.* and Woo *et al.*. Furthermore, the trends seen by

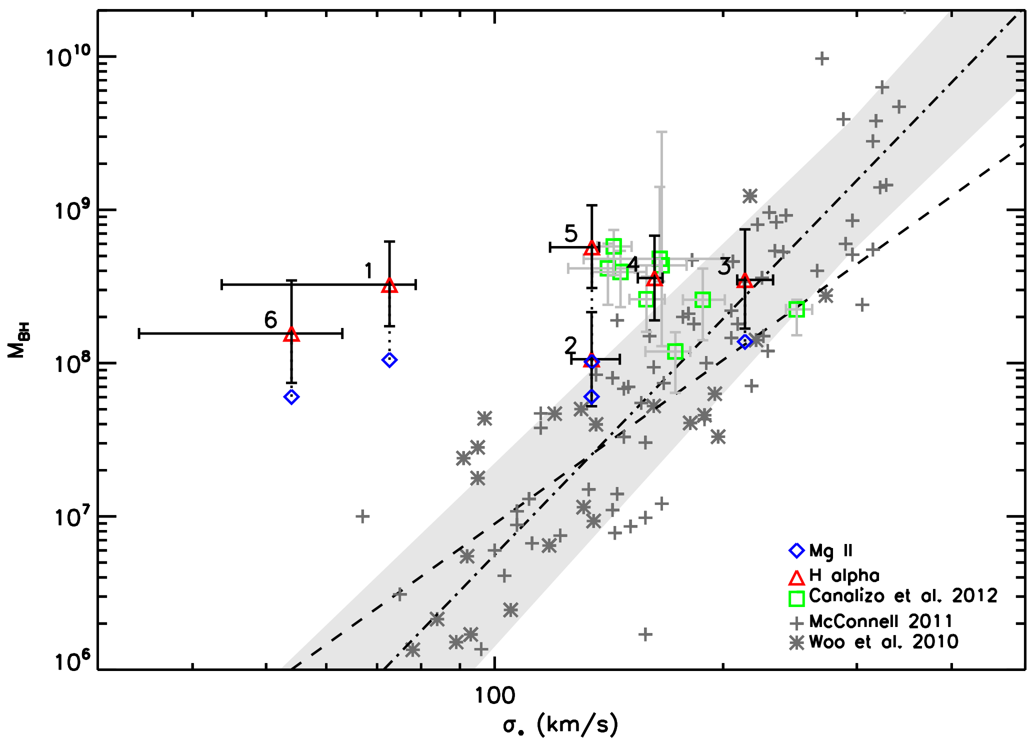

Fig. 3.6.— Plot of our objects compared to the locally-defined $M_{BH} - \sigma_*$ relation. The relation by McConnell et al. (2011a) is plotted as a dot-dashed line and grey plus symbols. The scatter is shown as a shaded grey region.The relation of reverberation mapped active galaxies by Woo et al. (2010) is plotted as a dashed line with grey asterisks. We plot the red quasars from Canalizo et al. (2012) in green squares. The black hole masses of the PSQs based on Hα and Mg II are plotted as red triangles and blue diamonds, respectively.

them appear to continue in our objects. As discussed by Canalizo *et al.*, at first glance this implies very recent evolution in the $\mathrm{M_{BH}} - \sigma_*$ relation.

The average $\mathrm{M_{BH}}$ offset for the sample of all six quasars with respect to the relation by Woo et al. (2010) is 1.25 dex when determined from the Hα broad line. If we exclude the object that does not conform to the Faber-Jackson relation (SDSS $2306-0100$, see below), then the average offset in $\mathrm{M_{BH}}$ becomes 1.06 dex. This result is significantly higher than the scatter in the local $\mathrm{M_{BH}} - \sigma_*$ relation, which is ~ 0.43 according to both Woo et al. (2010) and McConnell et al. (2011a). The offset we measure is slightly larger than the average offsets of red quasars found by Canalizo et al. (2012) and of non-local Sy 1s from Woo et al. (2006, 2008). Note also that the Mg II-based black hole masses are systematically lower than the Hα based masses. The average $\mathrm{M_{BH}}$ offset, again excluding SDSS $2306-0100$, based on the Mg II measurements is only 0.64 dex. The small number of objects in our sample preclude us from claiming whether the entire sample of PSQs is on average offset from the local $\mathrm{M_{BH}} - \sigma_*$ relation. To determine that, we will need to study more objects from the parent sample of PSQs. Furthermore, it is not unreasonable that for these six objects we will find some that fall above the 1σ scatter of the local relation, but it is curious that all of the offsets are on the same side of the relation.

The issue is complicated by the matter of the discrepancy between black hole masses measured with the Mg II and with the Hα emission lines. We used the SDSS data to measure the Hα emission for all but one object, and the SDSS spectroscopy has low S/N (< 10 pix^{-1}). Denney et al. (2009) show that using a Gauss-Hermite polynomial to fit low S/N data may overestimate the FWHM of the Hβ line. In the one object for which we have high S/N LRIS spectroscopy (SDSS 0057+0100) of the Hα region, we measured a lower FWHM of the Hα broad line compared to the SDSS spectrum. The difference was ~ 400 km s^{-1} ($\sim 8\%$). The black hole mass for SDSS $0057 + 0100$ using the larger width is only a factor of 1.2 greater than using the smaller width, which is within our defined errors. Smaller Hα widths would bring the Hα-based mass measurements closer to the Mg II-based measurements. However, this small effect is unlikely to reconcile the two measurements. As an alternative explanation, it is possible there is a systematic difference in BLR gas dynamics between the Hα and Mg II-emitting gas.

3.5.2. The $\mathbf{M_{BH}}-\mathbf{L_{bulge}}$ Relation

We plot the $\mathrm{M_{BH}}-\mathrm{L_{bulge}}$ relation in Fig. 3.8. This serves as a test of the bulge properties of the host. If the objects follow this relation, then the black holes of these galaxies may be "normal" for their bulges, while the velocity dispersions cause the offset seen in the $\mathrm{M_{BH}} - \sigma_*$ relation. In order to compare the bulge luminosities that we have measured here to measurements of systems in the local universe, we need to account for the change in luminosity associated with the evolution of stellar populations.

We measured the bulge luminosities in a procedure that is similar to the measurement of the AGN continuum luminosities. For each object, we scaled our fitted host galaxy template to the measured bulge photometry of Cales et al. (2011) in the *HST* F606W filter. We then measure V band photometry from the scaled host spectrum. Photometry from Cales *et al.* has already been k-corrected, but we also apply a passive

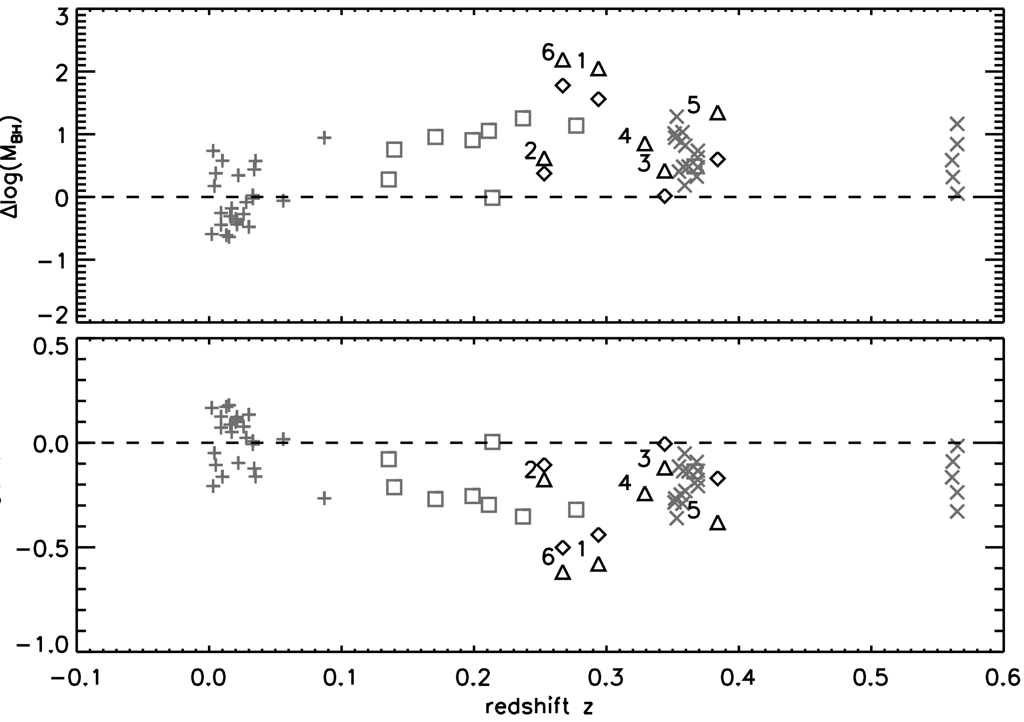

Fig. 3.7.— The offset from the local $M_{BH} - \sigma_*$ relation (Woo et al. 2010) is plotted against the redshift of the objects. The PSQs from our sample are plotted twice with triangles representing the Hα-based M_{BH} measurement and the diamonds the Mg II-based measurement (same as Fig. 3.6). The red quasars of Canalizo et al. (2012) are plotted as squares, and the Seyfert 1 galaxies from Woo et al. (2006) and Woo et al. (2008) are plotted as X symbols. The objects that define the local relation from Woo et al. (2010) are plotted as plus symbols.

evolution correction using the online calculator[1] of van Dokkum & Franx (2001). We applied the "Default 1: single stellar population" setting using the calculator, which uses a burst of star formation that passively evolves. This setting approximates the starburst event of our PSQs, which have luminosities dominated by the young population (see Table 3.3).

The "Default 1" setting of the passive evolution calculator assumes that the stars were formed at redshift $z >> 1$. However, the PSQs clearly have had a recent starburst within the past ≤ 1 Gyr. Thus, we adjusted this parameter to more closely match the star formation history of our targets. The difference in redshift from 0.3 (the average of the sample) to 0.4 corresponds to roughly 840 Myr. This is appropriate for all of our targets except SDSS $2118 + 0056$, which has a redshift closer to 0.4 than 0.3. For this target we adopt the passive evolution correction assuming a formation redshift of 0.5 (a 740 Myr stellar population). As expected, this produced a larger correction than assuming all stars formed at $z >> 1$, and applying this correction shifts the objects to smaller V band luminosities. We adopt an error on the bulge luminosities that assumes 0.1 mag error from the fits of Cales *et al.* and an additional 10% error on the spectral host-AGN decomposition.

In Fig. 3.8, the solid line shows the best fit relation from McConnell et al. (2011a), who compile measurements of individual galaxies from the literature, including brightest cluster galaxies. The two dotted lines show fits defined by the uncertainty in their scaling and slope, while the grey shaded region shows the intrinsic scatter they measured. Two

---

[1] www.astro.yale.edu/dokkum/evocalc/

of the Hα-based black hole mass measurements (triangles) fall above the scatter in the relation, while the remaining objects are consistent with the relation. However, if we consider the Mg II-based black hole masses (diamonds), all of the objects fall on the relation. We also note that the scatter from McConnell *et al.* (0.5 dex) is somewhat greater than that of Gültekin et al. (2009), who found 0.38 dex. If we were to consider the fit from Gultekin *et al.*, four of the Hα-based black hole masses would fall above the relation. Thus, to some degree, the interpretation of the offset from the relation depends on the relation's true intrinsic scatter.

The result is quite similar to that from the $M_{BH} - \sigma_*$ relation. That is: PSQs fall within the scatter or above the $M_{BH} - L_{bulge}$ relation if we consider the black hole masses measured from Hα. Whereas, if we consider the M_{BH} measured from Mg II, the PSQs are consistent with the relation. From this we can surmise that if the offset is to be believed, the black holes really are over-massive for their bulges.

3.5.3. The Faber-Jackson Relation

Figure 3.9 shows the location of our sample on the Faber-Jackson relation (Faber & Jackson 1976). If the σ_* values that we measured are causing the offset seen from the $M_{BH} - \sigma_*$ relation, we expect the objects to fall below this relation. That is, the objects should have velocity dispersions that are too small for their bulge luminosities. This is the case for one object, but the remaining five are generally consistent with the relation.

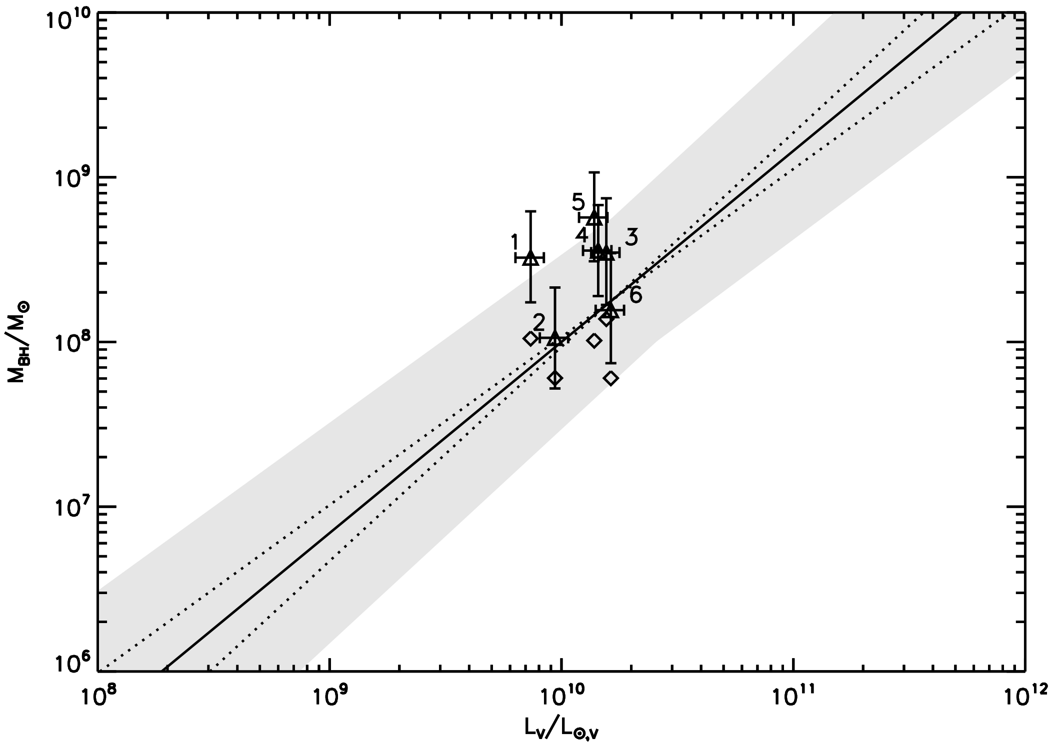

Fig. 3.8.— The $M_{BH}-L_{bulge}$relation. The solid line is the relation from McConnell et al. (2011a). The dotted lines show the relations defined by the uncertainty in the fitted scale and slope with scatter shown as the grey shaded region (±0.5 dex). Hα based black hole masses of the PSQs are plotted as triangles, and the Mg II based masses of the same objects are plotted as diamonds.

The left and right panels show the SDSS g band and r band absolute AB magnitude, respectively. The g and r photometry were measured with the same method that we used to measure the V band luminosity (see previous section) with the additional step of converting luminosities into SDSS AB magnitudes for ease of comparison. This also required transforming the passive evolution corrections from B and V to g and r corrections, for which we used the relations from Jester et al. (2005). Nigoche-Netro et al. (2010) calculate the Faber-Jackson relation in discrete magnitude bins of width 1 magnitude. Considering the g absolute magnitudes (*left panel*), the PSQs appear to follow the relations defined by Nigoche-Netro *et al.*. The dashed line represents the relation appropriate for objects with magnitudes between -19.5 and -20.5. Two objects fall in the magnitude bin -18.5 to -19.5 and are consistent with that relation. The only object that falls significantly offset is SDSS 2306-0100, which is one of the face-on disk galaxies. Considering the r magnitudes (*right panel*), all objects fall in the magnitude bin $-20 > M_r > -21$. Five objects are consistent with the relation, while SDSS 2306-0100 is again significantly offset. In both panels we have plotted the overall relation using the entire sample of Nigoche-Netro *et al.*. The fit for their overall sample has an intrinsic dispersion of 0.6 dex.

Desroches et al. (2007) have also studied the luminosity dependence of the Faber-Jackson relation. They derive a quadratic fit to to the relation in the SDSS r band using data from the NYU Value Added Galaxy Catalog (Blanton et al. 2005). While Nigoche-Netro et al. (2010) use only galaxies that are well fit by a de Vaucouleurs profile and the corresponding magnitudes, Desroches et al. (2007) select objects with a range of Sérsic indices and calculate a “Sérsic-like” magnitude from a Petrosian magnitude. As Desroches *et al.* explain, the Sérsic index is correlated with the galaxy luminosity and therefore may bias the slope of the relation if not accounted for. We have plotted the quadratic fit from Desroches *et al.* $\log \sigma_* = -1.79 + 0.674(\log \mathrm{L}) - 0.0234(\log \mathrm{L})^2$; $\mathrm{M} = -2.5(\log \mathrm{L})$) with 0.1 dex scatter in the right panel of Fig. 3.9 (solid line and dark grey shading) along with the fit from Nigoche-Netro et al. (2010). Three of our objects fall on the relation derived by Desroches *et al.*. One object falls above the relation (within 2σ), while two fall significantly below the relation. The two objects that are significantly offset are also the most offset from the $\mathrm{M_{BH}} - \sigma_*$ relation, suggesting that at least part of the offset is due to peculiar dynamics of the stellar population.

Norton et al. (2001) studied the velocity dispersions of quiescent E+A galaxies. To separate the post-starburst population from the underlying older population of stars they simultaneously fit the 4100 - 5250 Å region with K, G, and A star templates. They find that the post-starburst population does not show a significant correlation between its velocity dispersions and the overall host luminosities. However, the distribution of dispersions for their sample is consistent with the Faber-Jackson relation using data from Faber et al. (1989) and Jorgensen & Franx (1994). The older stellar population σ_* does show correlation with host luminosity, but the objects fall on average $\sim$0.6 mag brighter than the elliptical galaxies of similar dispersion. We do not separate the post-starburst population from the older population with unique measures of σ_* as Norton *et al.* do, so the value of σ_* that we measure has influence from both populations.

3.6. Discussion

We have measured $\mathrm{M_{BH}}$ and σ_* in six AGN that are hosted by galaxies showing post-starburst stellar populations ("post-starburst quasars"). These objects fall on or above the locally defined $\mathrm{M_{BH}} - \sigma_*$ and $\mathrm{M_{BH}} - \mathrm{L_{bulge}}$ relations. The location of the PSQs on the $\mathrm{M_{BH}} - \sigma_*$ diagram is consistent with other studies of objects at $z > 0.1$ (Canalizo et al. 2012; Woo et al. 2008, 2006).

We have used the Balmer region, which includes the Balmer series, Ca lines, the G band, and other stellar features to estimate the stellar velocity dispersions. While we have used host galaxy templates that approximate the stellar population of the host galaxies, it is possible that the young and old populations have different velocity dispersions. The kinematics of the young population are influenced by the mechanism that triggered the starburst. In a theoretical work, Bekki et al. (2005) describe various models of galaxy interactions (major/minor mergers, strong tidal interactions, etc.) that lead to E+A spectral signatures. They find a range of morphologies, velocity dispersions, and starburst mass fractions resulting from the merger event depending on the specific model used. The kinematic properties of the resulting post-starburst population depend on the initial parameters of the galaxy-galaxy interaction that induces the starburst.

The morphologies presented by Cales et al. (2011) for our sample indicate that these objects have only minorly disturbed features, if any, that could indicate a recent merger event. Four objects of our sample are described by Cales *et al.* as containing a disk component. However, the overall sample of PSQs display a range of morphologies, and Cales *et al.* found that half of the observed sample appear to be post-merger remnants.

The variety of morphologies seen in the parent sample is consistent with the simulations conducted by Bekki et al. (2005), indicating a range of possible galaxy-galaxy interactions that trigger the starburst event (*e.g.,* tidal interactions, minor/major mergers). Regardless of the triggering mechanism, the PSQs, at least in this subsample, have M_{BH} and σ_* that are generally consistent with previously studied $z > 0.1$ galaxies.

The origin of the velocity dispersion (pressure supported versus rotational) should influence whether the objects fall on the $M_{BH} - \sigma_*$ relation, which is best defined for pressure supported bulges. Observationally, Norton et al. (2001) studied the young and old populations independently in E+A galaxies and found them to be largely pressure supported, with the younger post-starburst population having higher σ_* than the old population. However, Bekki et al. (2005) had trouble reproducing this result with their models. By contrast, Pracy et al. (2009) found rotation to play a dominant role in their studied E+As.

We do not separate the young and old populations in our analysis, so the kinematical differences between the post-starburst population and older population in PSQs remains a question. In principle, we could adopt an additional free parameter in our model to measure the velocity dispersion of the old population separately from the young population. However, this would introduce degeneracies that would be difficult to disentangle, especially with the presence of the active nucleus. We are currently conducting an investigation into the kinematic differences between young and old populations in quiescent E+A galaxies that lack the active nucleus continuum contamination (Hiner & Canalizo 2012, in preparation). This analysis will be similar to that of Norton *et al.*, but we will include multiple wavelength regions. By including longer wavelength regions, such as the Mg Ib and Ca II triplet regions, we will be able to further distinguish between the young and old stellar populations.

We have also measured the bulge luminosities of the host galaxies. After plotting the $M_{BH}-L_{bulge}$ and Faber-Jackson relations, we find a scenario which rules out σ_* bias as the source of the offset from the $M_{BH} - \sigma_*$ relation for three of the six objects we measured. Two objects (SDSS $0030-1035$ and SDSS $2306-0100$) are significantly offset from the $M_{BH} - \sigma_*$ relation. SDSS $2306-0100$ is additionally offset from the Faber-Jackson relation, indicating that the measured σ_* may be significantly influenced by the face-on disk of the host galaxy. SDSS $0030-1035$ is consistent with the relation as defined by Nigoche-Netro et al. (2010), but it falls significantly below that of Desroches et al. (2007), so it may also be influenced by the face-on disk. While SDSS $0237-0101$ falls above the Desroches *et al.* Faber-Jackson relation by less than 2σ, it is also the object that falls closest to the best fit $M_{BH} - \sigma_*$ relation. A reduction of ~ 50 km s^{-1} in σ_* would bring it in line with the Desroches *et al.* fit, but drive the object left of the $M_{BH} - \sigma_*$ relation (consistent with the other offsets). Peculiar dynamics can clearly influence the measured velocity dispersion, and with a more statistically significant sample, the general trends will become more apparent.

The offset from the $M_{BH} - \sigma_*$ relation is consistent with that found by Canalizo et al. (2012). Similar to their sample and the samples of Woo et al. (2006) and Woo et al. (2008), the black holes measured here all have masses $\geq 10^8$ $M_\odot$. This brings up the question of sample selection at high-z ($z > 0.1$). Lauer et al. (2007) describe a potential bias that selects for high-mass black holes at higher-z, which is a product of a steep luminosity function and cosmic scatter in both the $\mathrm{M_{BH}} - \sigma_*$ and $\mathrm{M_{BH}}{-}\mathrm{L_{bulge}}$ relations. Canalizo et al. (2012) also show that highly luminous AGN ($\log(\mathrm{L_{5100}}/\mathrm{erg\ s^{-1}}) > 43.6$) are offset from the $\mathrm{M_{BH}} - \sigma_*$ relation regardless of their redshifts. All but one of the PSQs in our sample have luminosities in this range.

We have presented six objects of a larger class of post-starburst quasars (Brotherton et al. 2012, in preparation). This is clearly not statistically significant and we may have by chance chosen objects that all fall above the $\mathrm{M_{BH}} - \sigma_*$ relation. To discuss PSQs as a whole, we require measurements of more objects that define a statistically significant sample. We have obtained data for additional PSQs from the same parent sample that will be exhibited in a future work (Hiner et al. 2012a, in preparation). In addition, it will be important to disentangle the kinematics of the younger post-starburst population from the underlying older stellar population. For this purpose, we have obtained spectroscopy of quiescent E+A galaxies. We will probe possible differences in σ_* kinematics between the populations using both the Balmer series and longer wavelength regions (*e.g.,* Mg Ib, CaT).

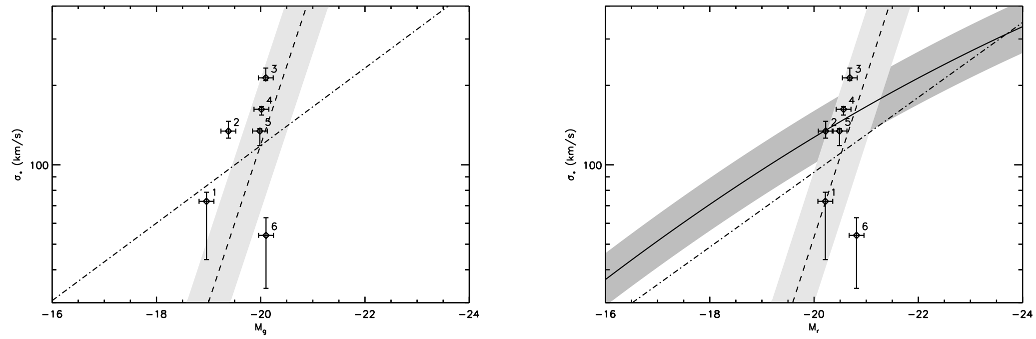

Fig. 3.9.— The Faber-Jackson relation. *Left*: The SDSS g band absolute AB magnitudes. The dashed line is the best fit from Nigoche-Netro et al. (2010) for the magnitude bin -19.5 $>$ g $>$ -20.5. *Right*: The SDSS r band absolute AB magnitudes. The dashed line is the best fit from Nigoche-Netro et al. (2010) for the magnitude bin -20 $>$ r $>$ -21. The solid line and dark grey region show the quadratic fit and scatter to the Faber-Jackson relation from Desroches et al. (2007). For both panels the the light grey shaded region shows the scatter in the fit from Nigoche-Netro et al. (±0.25 dex, 2010), and the dot-dashed line shows the best fit for the overall sample of Nigoche-Netro *et al.*.

Chapter 4

Red Quasars

4.1. Introduction

Red quasars are a unique sample of type-1 AGN where the nucleus has been subjected to the effects of moderate extinction. Dust extinction is wavelength dependent, and decreases in strength with increasing wavelength. The magnitude of the extinction in red quasars is in a “Goldilocks-zone”: it is just strong enough to dim the nuclear light at short wavelengths while not being so strong as to block the Hα broad emission line at longer wavelengths. The net result is that the host galaxy and the reddened active nucleus spectrum are simultaneously observable.

We performed an investigation of nine dust-reddened type-1 AGN located at $0.14 < z < 0.37$ in order to measure both host galaxy and black hole (BH) properties (Canalizo et al. 2012). Marble et al. (2003) observed a set of 29 red QSOs with the Hubble Space Telescope (*HST*) taken from the compilation of 2MASS QSOs by (Cutri et al. 2002).

The sample has $\mathrm{M_K} < -25$ and $J - K_s > 2.0$. The color criterion ensures a reddened slope, and the magnitude criterion ensures quasars luminosities. The main goal of our program was to measure the $\mathrm{M_{BH}} - \sigma_*$ relation for objects in the non-local universe, much like our intention for the study of post-starburst quasars (Chapter 3).

We obtained spectroscopy of the targets with the Echellette Spectrograph and Imager (ESI) on Keck II. The data reduction and analysis are described by Canalizo et al. (2012). These spectra were fit with a modeling routine similar to the one described in chapter 3, from which we determined stellar velocity dispersions, σ_*.

Measuring BH masses in these objects is not as straight forward as in the case of the post-starburst quasars, because the nucleus is heavily extincted. To apply the virial technique, one requires both the broad line width and intrinsic continuum luminosity. We estimated the reddening by fitting the observed spectral slope measured from the fitting routine with a composite quasar spectrum and SMC reddening law. With a measure of the reddening in hand, all we need to obtain the intrinsic nuclear luminosity is a measure of the absolute reddened luminosity, deconvolved from the host galaxy.

The host-to-nucleus ratio can be measured using high resolution imaging, such as that from *HST*. A deconvolution of high resolution imaging provides photometry on the active nucleus and the host galaxy. Additionally, we can measure the sizes of the host and classify their morphologies: whether they are bulge/disk dominated or if they show signs of merger activity. In the following sections I will describe the measurements of Hα and the morphological deconvolution of the red quasars and their hosts. These results were submitted for publication in the Astrophysical Journal by Canalizo et al. (2012).

4.2. Measuring the FWHM$_{H\alpha}$

Hα is flanked by N II $\lambda\lambda$ 6548, 6583, and, therefore, a detailed decomposition is required to measure the Hα broad line width. We follow the method outlined by Glikman et al. (2007) and Greene & Ho (2004). We performed all our line fits using the *specfit* task (Kriss 1994) in the IRAF STSDAS package.

First, we created a narrow line model by fitting the S II $\lambda\lambda$6716, 6731 doublet. Often we found blue wings in the line profile. We fit this using two Gaussians per line, one of which was allowed to have skew (or asymmetry), although, we found skew was not needed in all cases. The continuum was fit simultaneously with a power law function. To ensure the same model fit for both lines, and to avoid unrealistic degeneracies, we constrained the model for each line of the doublet to be the same. This was done by matching the widths of each component and the relative positions of the doublet. Because we used a two-Gaussian model, an extra constraint on the flux ratio was necessary to ensure the same total model for each line. Garstang (1952) calculates the transition probability and intensity ratio of the doublet ^{4}S - ^{2}D transition in S II. He finds it can range from 0.5 to 0.8 depending on the parameters used in the calculation. However, he also cites a reasonable observed value of 0.74 based on NGC 7662. We adopted this observed value for our S II fits, as it produced the most reasonable fit of the range.

In some cases the S II doublet was contaminated by the Hα broad emission or telluric absorption. In these cases we fit the [O III] $\lambda\lambda$4959, 5007 doublet to create a narrow line model. Similar techniques as with the S II doublet were used to fit the [O III] doublet. In this case the doublet flux ratio was constrained to 2.87 (Osterbrock & Ferland 2006), which fit our data fairly well.

We then fit the region around Hα using the narrow line model for N II λ6548 and N II λ6583. We constrained the relative position of the N II lines using the laboratory wavelengths for these lines. While Glikman et al. (2007) constrained the N II flux ratio to a theoretical value of 2.96, we found better fits when we let the flux of each N II line be freely fit. This often resulted in a flux ratio greater than 2.96. In addition, we included a narrow line component of Hα using the fitted model and we used a power law to characterize the continuum. Finally, we included a broad Gaussian (with initial width of 5000 km s^{-1}) to model the broad line Hα component. We first fixed the broad Hα line to be symmetric, then added skew after its centroid position had been located by the fitting routine.

Specfit uses a simplex method to minimize χ^2. We adjusted input parameters and initial step sizes iteratively to probe different local χ^2 minima and thus found the global χ^2 minimum.

The errors in the FWHM$_{H\alpha}$ resulting from the fit are typically ~15 km s^{-1}. The true uncertainties, however, are much larger since they are dominated by the uncertainties in the modeling of the narrow component and the decomposition of the broad and narrow components. In order to estimate conservative errors, we found the lowest and highest values of $\mathrm{FWHM}_{H\alpha}$ for which it was no longer possible to obtain a fit to the region, regardless of the values given to any of the other parameters.

The final values for $\mathrm{FWHM}_{H\alpha}$ and their uncertainties are listed in Table 4.1. The $\mathrm{FWHM}_{H\alpha}$ we measure for 225902.5+124646 is highly uncertain because Hα has a very asymmetric profile, with very extended emission on the blue side of the line. This is likely indicative of an outflow, so that the M_{BH} we derive from it may not be reliable. We attempted a variety of ways to separate the core of the line from the outflow, by fitting the latter with multiple Gaussians blueshifted with respect to the core. In order to ensure that we obtain a conservative measure of M_{BH}, we chose the smallest value of $\mathrm{FWHM}_{H\alpha}$ that would fit the line.

We show the fits of the Hα region in Fig. 4.1. The ESI data are plotted in black, the overall model in red, the narrow emission line models in blue, and the broad emission line models in green. The data and overall model have had the continuum subtracted.

4.3. Galaxy Morphologies

We analyzed the *HST* imaging data with the two-dimensional modeling program GALFIT (Peng et al. 2002) to achieve three primary goals: (1) to obtain photometry of the nucleus to be used in the measurement of M_{BH}, (2) to determine the size and characteristics of the bulge component if present, and (3) to search for signs of interaction in order to properly interpret our results.

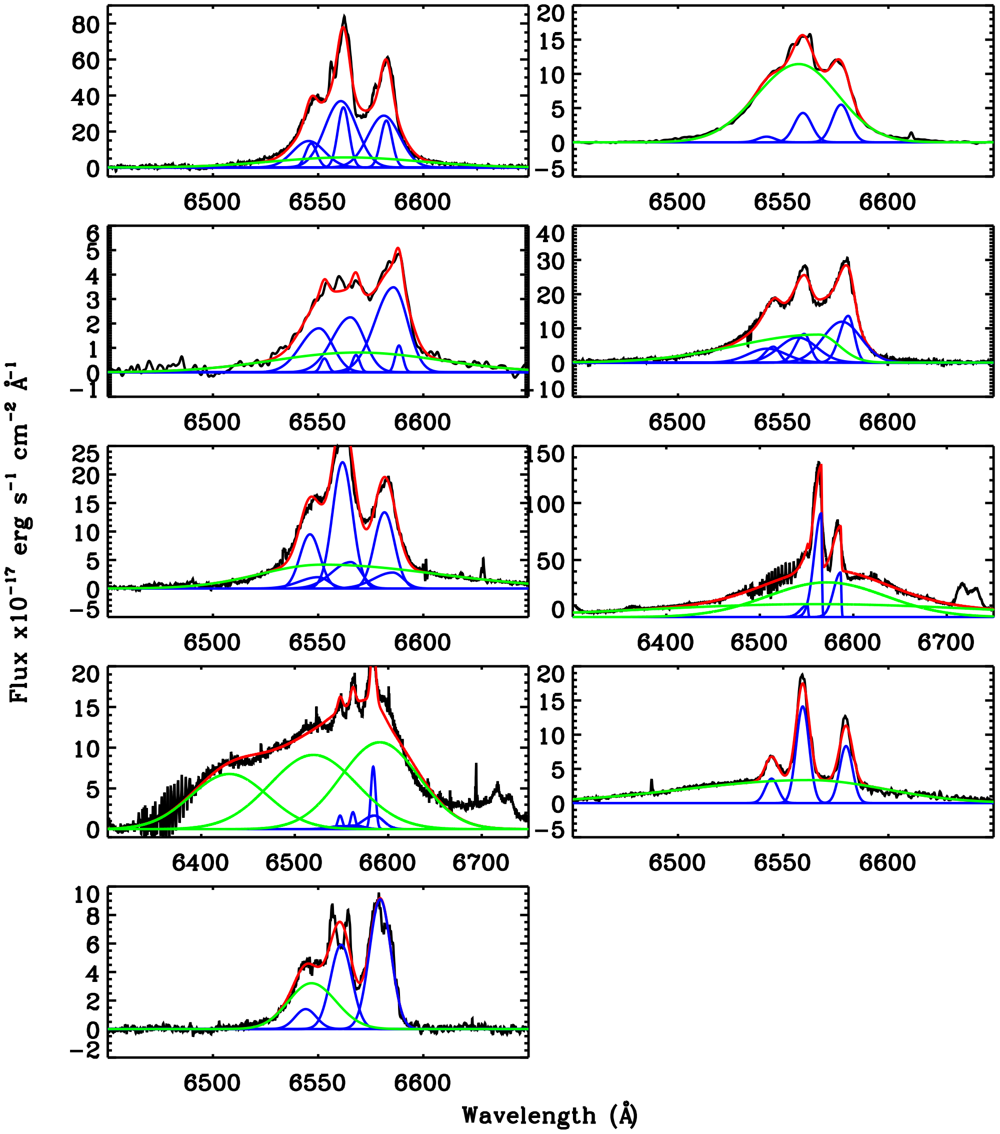

Fig. 4.1.— The ESI data are plotted in black, the overall model in red, the narrow emission line models in blue, and the broad emission line models in green. The data and overall model have had the continuum subtracted.

It is imperative that the appropriate PSF is used when modeling galaxy morphologies. Empirical PSFs are ideal for this purpose, as they reflect the same instrumental conditions that were used for the observations. We searched the *HST* archive for high signal-to-noise stars (typical peak counts were ~ 2100) that were observed with the same instrument and filter and that fell near the same CCD position as the QSOs. The input PSF image must be large enough to encompass the wings of the function, so we chose a large region and interpolated across extra sources within the cut. Since the PSF is under-sampled in the PC image, we broadened it with a Gaussian of $\sigma = 0.8$ pixels. This increased the full-width at half-maximum (FWHM) of the PSF to be greater than 2 pixels, while preserving the encompassed flux.

The science images need to be large enough to accurately estimate the background sky level. This is especially important, because the edges of galaxy profiles are sensitive to the background sky level, and can affect, for example, the Sérsic index, n, of the profile fit to the galaxy. We cut each image to 15".75 by 15".75 (350 pixels x 0.045 arcsec pix^{-1}) centered on the science target, which is several times the size of the targets themselves. This large region sometimes included other objects, which we either masked from the fit or fit with an extra component. To match the resolution of the PSF, we also broadened the science images with the same Gaussian used on the PSF.

We followed an iterative process while fitting the morphologies of the galaxies. Each fit included the point source (a scaled PSF) and background sky level estimated by GALFIT. We began with simple models of single bulge or disk components for the host galaxies and added complexity as necessary. All but one of the galaxies required two or more components to model the host. Where the image showed multiple objects in the field, the secondary object was fit with its own component or masked from the fit. We generally used free index Sérsic profiles to model the bulges, but in many cases, GALFIT did not converge on a reasonable Sérsic index. To fit these hosts, we ran several iterations of GALFIT holding the index constant at values $n = 1$, 2, 3, and 4. In each case the $n = 4$ fit the image the best. We adopted the best-fit models based on the χ^2 values and residuals of the model subtracted image.

We report magnitudes for the best fits of each of the targets. Visual inspection of the residual images indicate that the point source and PSF were slightly mismatched. In order to estimate the uncertainty in the magnitudes, we also performed a direct PSF subtraction and determined the upper and lower limits for which the PSF was clearly over- and under-subtracted, respectively. The magnitudes measured by direct subtraction were, in each case, within 0.1 mag of the value obtained from the GALFIT fits, except for 005055.7+293328, for which the difference was 0.36 mag. Our measured magnitudes are systematically fainter than those reported by Marble et al. (2003), with the differences ranging from less than 0.1 mag to 1.1 mag in the most extreme case (165939.7+183436). The differences likely arise from the fact that we fit simultaneously a PSF with the different components of the host galaxy (e.g., bulge and disk), so the nuclear fluxes that we measure are less likely to be contaminated by light from the host galaxy. Another reason for the differences in magnitudes may be the choice of PSFs: Whereas we selected empirical PSFs from the *HST* archive, Marble et al. (2003) used one of the QSOs in their sample as the PSF to subtract from all the other QSOs.

They chose 222202.2+195231 since it did not show significant extended emission after subtracting an artificial PSF created with the software package Tiny Tim (Krist & Hook 2001).

In Table 4.2 we list the magnitudes of the PSF and Sérsic components used to fit each object. The magnitudes are apparent *HST* F814W magnitudes, not corrected for Galactic extinction nor K-corrected, to allow for direct comparison with results published by Marble et al. (2003). Every object appears to have a clear bulge component. In Figs. 4.2, 4.3 and 4.4 we show the image, the best fit model, and the residuals after subtraction of each of the targets.

The object 005055.7+293328 is hosted by a spiral galaxy and has a prominent dust lane in the central region. In order to obtain the best estimate for the nuclear flux we fit the host galaxy with multiple components so as to minimize the residuals after subtraction. The best fit included the spiral arms, disk, bulge, and an additional narrow Sérsic profile (not included in Table 4.2) to account for the asymmetric light distribution due to the dust lane. While fitting all these components allows us to obtain a good fit for the PSF, it is likely that we are underestimating the flux and the effective radius of the bulge, since we are splitting it into two components.

4.4. Discussion

We measured BH masses using the virial technique. This involved conducting a detailed spectral deconvolution of the Hα spectral region, and a morphological deconvolution using high resolution *HST* imaging data.

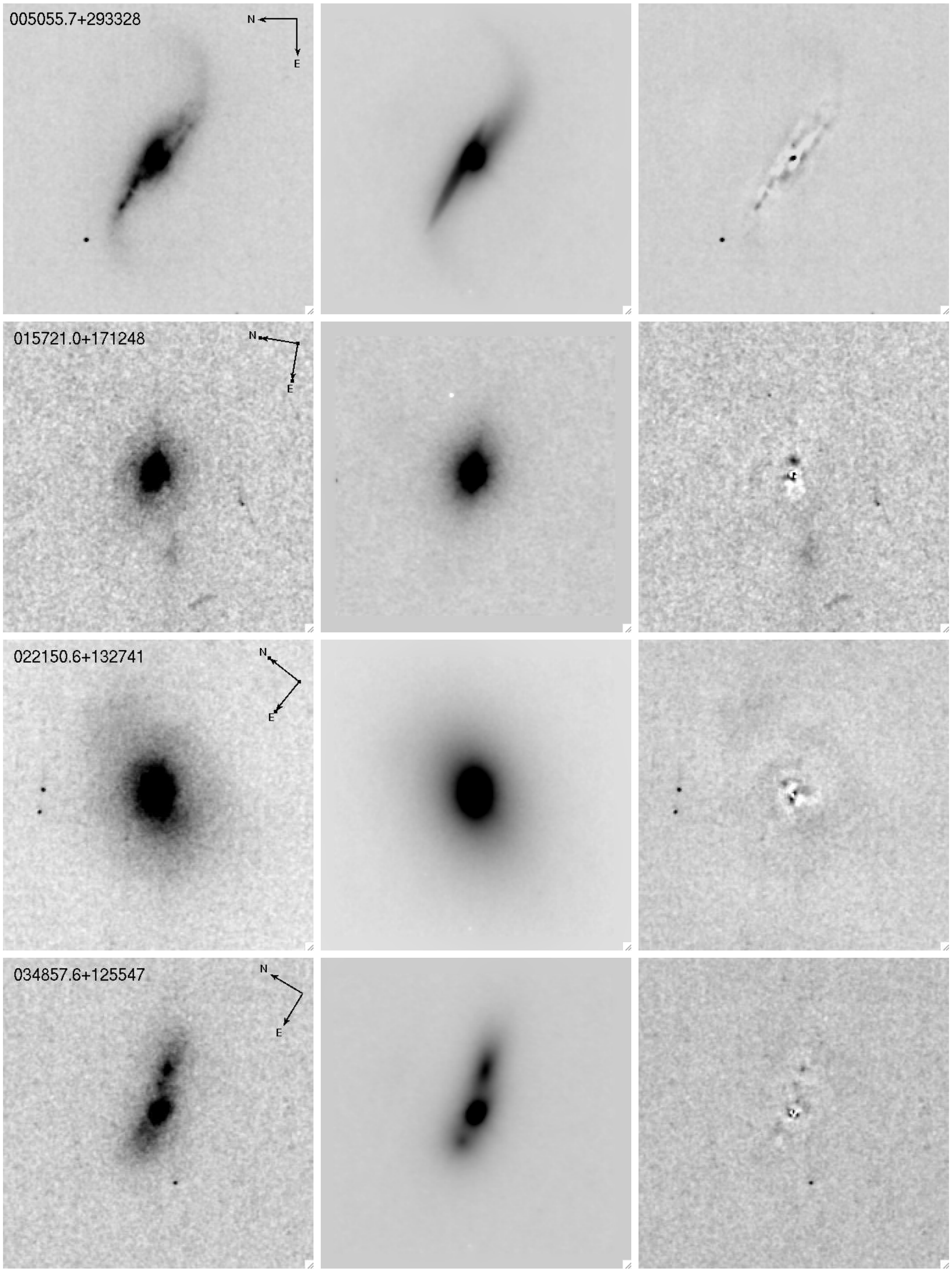

Fig. 4.2.— *HST* images of the red quasars. *Left*: the F606W data. *Center*: the best fit model created with GALFIT. *Right*: The residual image (data - model).

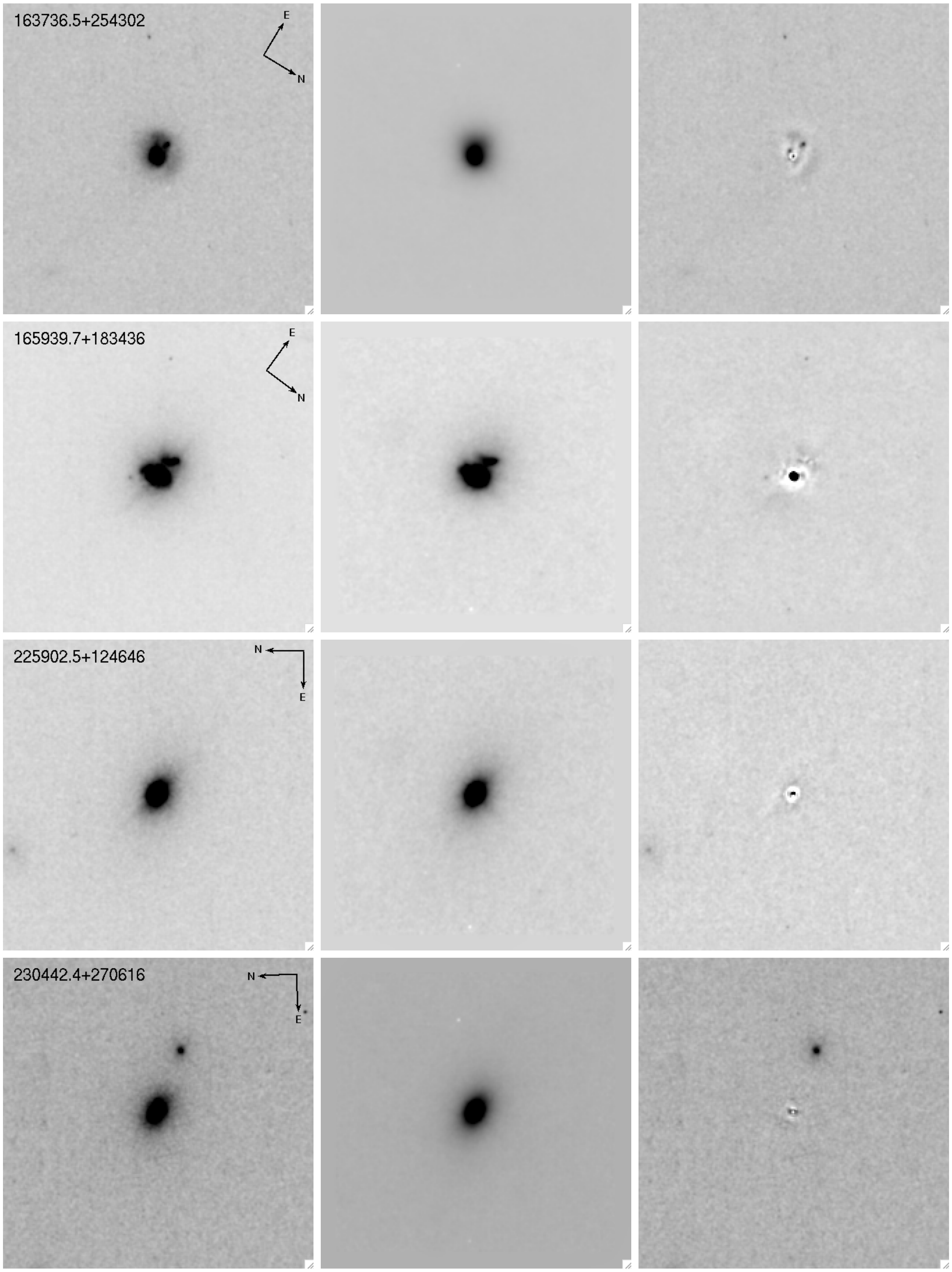

Fig. 4.3.— Same as Fig. 4.2

Table 4.1: Hα FWHM measurements

Object	FWHM	σ_{up}	σ_{down}
005055.7 + 293328	2679	227	175
015721.3 + 171248	2196	27	32
022150.6 + 132741	4279	421	492
034857.6 + 125547	4213	355	342
163736.5 + 254302	3178	371	248
165939.7 + 183436	6742	3640	142
225902.5 + 124646	4457	5543	100
230442.4 + 270616	6349	251	265
232745.6 + 162434	2341	416	161

Note. — FWHM and associated errors are presented in km s^{-1}.

Fig. 4.4.— Same as Fig. 4.2

Table 4.2: Results of Modeling the QSO Host Galaxies Using GALFIT

QSO (2MASSi J) (1)	Component (2)	$m_{\rm F814W}$ (mag)[a] (3)	$r_{\rm eff}$ ($''$) (4)	$r_{\rm eff}$ (kpc) (5)	Sérsic Index (6)
005055.7+293328	PSF	20.50	···	···	···
	bulge	19.27	0.22	0.52	4 (fixed)
	disk?	19.42	3.46	8.22	0.15
	arms	18.56	1.89	4.50	0.63
015721.0+171248	PSF	20.45	···	···	···
	bulge	20.67	0.19	0.67	4 (fixed)
	disk	19.86	0.72	2.50	1 (fixed)
022150.6+132741	PSF	21.17	···	···	···
	bulge	17.93	2.89	7.04	4 (fixed)
	disk	18.88	2.13	5.19	0.5
034857.6+125547	PSF	21.57	···	···	···
	bulge	19.80	0.79	2.70	5.8
	disk	20.88	0.44	1.51	1 (fixed)
	disk	20.08	0.70	2.40	1 (fixed)
163736.5+254302	PSF	21.37	···	···	···
	bulge	19.88	0.22	0.92	4.7
	disk	19.87	0.49	2.04	0.6
165939.7+183436	PSF	19.11	···	···	···
	bulge	18.21	0.26	0.76	4 (fixed)
225902.5+124646	PSF	19.40	···	···	···
	bulge	18.82	0.41	1.33	3.7
	disk	19.51	1.20	3.89	1 (fixed)
230442.4+270616	PSF	20.70	···	···	···
	bulge	19.23	0.98	3.65	4 (fixed)
	disk	21.50	0.32	1.18	1 (fixed)
232745.6+162434	PSF	22.12	···	···	···
	bulge	19.20	1.30	6.56	4 (fixed)
	disk	20.07	1.03	5.22	1 (fixed)

---

[a] F814W magnitudes not corrected for Galactic reddening or for intrinsic reddening.

In some cases the Hα profiles were best fit with multiple Gaussian components or with significant skew. The complex kinematics in these cases point to a BLR that is not necessarily dynamically settled or virialized. This is consistent with the results from the image analysis. We found that many of the objects showed signs of interactions or major merger scenarios. Only one galaxy can be classified as a late-type barred spiral galaxy.

The red quasars of our sample are associated with merging galaxies, and fit well with the merger-driven AGN model. Furthermore, the objects fall on or above the local $\mathrm{M}_{\mathrm{BH}} - \sigma_*$ relation, indicating that the BHs are over-massive compared to their hosts. This could be a result of feeding the BH before the merger remnant has settled.

Chapter 5

An Infrared Comparison of Type-1 and Type-2 Quasars

5.1. Introduction

The study of various types of AGN can provide insight into their origin and evolution. AGN are classified according to their optical emission lines as type-1 or type-2. Type-1 AGN have an “unobscured” view of the hot accretion disk and broad emission lines originating from fast moving clouds that surround a supermassive black hole. Type-2 objects are known as “obscured” AGN, because no broad lines or continuum emission from the accretion disk are observed, yet the spectra still show narrow emission lines similar to those of the type-1 objects.

The interpretation of the differences between type-1 and type-2 quasars (the most luminous AGN) remains an open issue. The orientation-based unification scheme proposes the two types of objects are intrinsically the same, but appear different observationally due to the presence of an obscuring torus of dust close to the central power source (see Antonucci 1993). Type-1 objects are seen from an orientation which allows an unobscured view of the central source. This allows the broad line region of the quasar to be observed. However, type-2 objects are seen through the dusty torus material, which hides the central continuum source and broad-line region. Evidence that this model is at least partly correct comes from observations of polarized broad-line emission in galaxies classified as type-2 quasars (*e.g.,* Zakamska et al. 2005). But this model does not provide insight into the origin of quasar activity.

An alternative model proposes that quasar activity is triggered by galactic mergers and evolves through an obscured stage (Sanders et al. 1988). As the galaxies merge, gas and dust are stirred up, triggering quasar activity and star formation. Initially the quasar would be obscured by the dust, but over time will become unobscured as dust and gas are blown away from the nuclear region by quasar and/or supernovae driven winds and radiation pressure. Indeed, several host galaxy studies have been made which show that luminous AGN are hosted by massive, mainly spheroid-dominated galaxies, with a significant fraction, but not all, showing signs of a relatively recent merger and associated star formation (*e.g.,* Dunlop et al. 2003; Canalizo et al. 2007; Bennert et al. 2008). Thus the evolution model predicts that the host galaxies of type-2 quasars should have more recent star forming activity than those of type-1s. Although the discovery of polarized broad lines is a powerful argument in favor of the orientation-based model, it does not rule out an evolutionary link.

The obscuring dust in a host galaxy would be apparent in its observed SED. Dust close to the AGN would be heated by the central power source and would thermally re-radiate in the mid-IR (100 - 1000K), dominating the rest-frame SED from $\sim$2 - 40 μm. This high temperature dust emission makes the mid-IR SEDs of both optically-obscured and optically-unobscured AGN quite distinct from those of either normal or starburst galaxies, whose dust temperatures are always $\leq$ 100K. By modeling the various components of the SEDs, we can compare the relative amounts of "cool", "warm", and "hot" dust emission present in the host galaxies. This will give us some idea of what mechanism dominates the heating of the dust (star formation or AGN), and how much of a role orientation might play in the observed SEDs.

In this paper, we present modeled fits to the SEDs of a sample of type-1 and type-2 quasars of similar redshift and luminosity. Lacy et al. (2007) presented preliminary fits to the type-2 quasars in this paper. We also measure the objects' far-IR luminosities, PAH luminosities, and estimate their star formation rates. We then compare the results with starburst galaxies. We describe the sample selection in §2, and the observations and reductions in §3. In §4 we present the analysis and results including our modeling procedure and resultant spectra, a color-color diagram, and star formation rate (SFR) calculations. Finally, we summarize our results in §5. Throughout this paper we adopt the cosmological parameters of H_0=71 km s^{-1} Mpc^{-1}, Ω_M=0.27 and Ω_Λ=0.73.

5.2. Sample Selection

Quasar surveys are now highly effective at finding quasars on the basis of their optical colors, provided they are not reddened or only lightly reddened by dust. With surveys such as the Sloan Digital Sky Survey (SDSS) (Schneider et al. 2003), 2dF (Croom et al. 2004), and Combo-17 (Wolf et al. 2003), a census of such objects across the full range of quasar luminosities and redshifts out to z $\sim$ 6 is largely complete. Only recently have radio-quiet type-2 quasars been found in substantial numbers. However, there is still no consensus on how the dust-obscured quasars are related to the unobscured population. In particular, it is difficult to select matched samples of type-1 and type-2 objects with which to perform such studies. By using *Spitzer* data from the extragalactic First Look Survey (XFLS), we have been able to construct samples of type-1 and type-2 quasars matched in mid-IR luminosity and redshift.

Lacy et al. (2004) showed that quasars occupy a distinct "sequence" of a *Spitzer* IRAC color-color plot (their Fig. 1). Follow-up spectroscopy of a sample of mid-IR selected AGN and quasar candidates showed that about 2/3 of AGN selected in this manner may be sufficiently obscured by dust in the optical to be missing from optically-selected quasar samples (Lacy et al. 2007). We selected six type-2 quasars and six type-1 quasars (see Table 5.1) from the 1 mJy 8 μm flux-limited sample of Lacy et al. (2004), with similar mid-IR colors and 5.8 μm luminosities. These objects are approximately matched in mid-IR luminosity. Our modeling (see §5.4.1) shows they have mid-IR power-law luminosities within a factor of five from each other. Furthermore, the observed frame 24 μm luminosities of the type-1 and type-2 quasars are not statistically different from each other. It is important that the sample be matched in luminosity, since the quasar luminosity will affect the rate at which dust and gas is removed from the nuclear region.

5.3. Observations and Data Reduction

We supplement data from the *Spitzer* Extragalactic First Look Survey (xFLS) (Fadda et al. 2006; Frayer et al. 2006) with targeted observations in the 70 μm and 160 μm using the Multiband Imaging Photometer for *Spitzer* (MIPS). Each of our targets was detected at the 24 μm wavelength in the *Spitzer* xFLS. Five of our targets were detected in the 70 μm xFLS mosaic, and we measured the 70 μm fluxes for two other targets directly from the xFLS mosaic image. The remaining five targets of our sample were not detected in the 70 μm xFLS mosaic and so required targeted observations. We observed each of these targets for 500 seconds. All of the targets were observed with the MIPS 160 μm band for 2000 seconds each.

The photometric data were reduced through the standard *Spitzer* MIPS pipeline. We used the post basic calibrated (post-BCD) filtered mosaic images to measure the flux of each target. The pixel scales of the post-BCD MIPS images are 4 arcsec pixel^{-1} at 70 μm and 8 arcsec pixel^{-1} at 160 μm .

We also observed each target using the short-low and long-low resolution modes with the *Spitzer* infrared spectrograph (IRS). The spectra were reduced through the standard *Spitzer* pipeline. We manually masked the bad pixels in the background subtracted spectra (difference between nodded exposure positions) using the IDL program

IRSCLEAN[1]. We then extracted the spectra using the standard point source extraction in the *Spitzer* SPICE[2] software tool, and combined the individual spectra to create a continuous mid-IR spectrum for each target. Lastly we included photometry measured from our MIPS data (Table 5.1) and data available for our targets from SDSS, 2MASS and *Spitzer* IRAC observations (Table 5.2) to produce an observed frame SED that ranges from optical through the infrared.

5.3.1. Photometry

We used the DAOPHOT package in IRAF to measure the 70 μm and 160 μm fluxes of our targets. For the 70 μm measurements we examined each image individually and determined the best aperture and sky annulus that maximized the signal-to-noise ratio. We then applied aperture corrections from the *Spitzer* Space Telescope MIPS Data Handbook[3], and compared the measured flux to a 3σ limit obtained by measuring the noise in the image.

Each of our 12 targets was observed in the 160 μm MIPS band, though many of our targets were not detected at this wavelength. We chose an example image with a strong detection and determined the aperture and sky annulus sizes that maximized the signal-to-noise ratio. We used those parameters while measuring the other images with bright detections. The same procedure was used for the images with targets that were

---

[1] http://ssc.spitzer.caltech.edu/archanaly/contributed/irsclean

[2] http://ssc.spitzer.caltech.edu/postbcd/spice.html

[3] http://ssc.sptizer.caltech.edu/mips/apercorr/

not detected. We then compared the measured fluxes of each of the targets to the 3σ limit determined from the noise in the image. Five of the 12 targets have fluxes less than the 2σ noise limit, and we count them as non-detections. Five other targets have fluxes $>2\sigma$, and only one has 160 μm flux $>3\sigma$. The remaining target is discussed following.

The target SDSS 1711+5855 required special attention, because there was a bright object near the target. We fit a PSF using several other bright objects in the image, then subtracted sources from the image leaving only our target. We then measured the flux of SDSS 1711+5855 from the subtracted image. This procedure was successful at 70 μm, but our attempts at removing the extra source at 160 μm resulted in an image with significant residuals. Therefore, we only report an upper limit measured from the combined flux of the objects at 160 μm. This upper limit was not used in our modeling procedure and analysis.

Table 5.1 shows the results of our MIPS flux measurements combined with data from the xFLS.

5.3.2. Spectra

We present the *Spitzer* IRS spectra for our sample in Fig. 5.1. The spectra show distinct differences. The spectra of the type-1 quasars tend to have fewer features and are more homogeneous than those of the type-2s. The type-1 objects show significant continuum emission near 3 μm, little PAH emission, and no significant silicate absorption. The type-2 spectra are more heterogenous, showing a variety of silicate absorption depths and PAH strengths, consistent with previous observations of AGN (*e.g.,* Hao et al. 2007; Spoon et al. 2007; Zakamska et al. 2008) as well as starburst galaxies, ULIRGs and sub-mm galaxies (*e.g.,* Brandl et al. 2006; Sajina et al. 2007; Lutz et al. 2008; Menéndez-Delmestre et al. 2009). The type-2 quasars have on average double the PAH luminosity of the type-1 quasars (see Table 5.3).

Spoon et al. (2007) classify spectra based on their 6.2 μm PAH equivalent width and 9.7 μm silicate absorption strength. Our type-2 spectra are similar to their 1B, 1C and 2B classifications. These classifications are dominated by Seyferts, starbursts, and ULIRGs, respectively. Our type-1 quasars have spectra most similar to the 1A classification of galaxies by Spoon *et al.*

The variation of silicate absorption strengths in the type-2 spectra of our sample is also consistent with that seen by Zakamska et al. (2008), who study a sample of optically selected type-2 quasars from the SDSS. Zakamska *et al.* find silicate absorption similar to some of our sample, including two objects that have more significant absorption than our sample (see Lacy et al. 2007). Four of their objects appear to have no silicate absorption, including one that may show silicate emission, consistent with our mid-IR selected type-1 quasars. They also address the correlation of silicate absorption with axial ratio found by Lacy et al. (2007). Lacy *et al.* interpreted this correlation to indicate that the silicate dust resides in the host galaxy, and not the nuclear region. The objects of Zakamska et al. (2008) show no correlation, and they propose this could be a difference in samples due to selection biases based on luminosity.

Table 5.1: Targets and their Fluxes in mJy

Target	Type	z	f_{24}	σ_{24}	f_{70}	σ_{70}	f_{160}	σ_{160}
SDSS 171117.66 + 584123.8	1	0.617	5.77	0.07	34.9	6.3	30.4	13.4
SDSS 171126.94 + 585544.2	1	0.537	3.45	0.07	12.7	6.6	<102.1	···
SDSS 171334.03 + 595028.3	1	0.615	5.38	0.07	7.5	1.6	<11.1	3.7
SDSS 171736.91 + 593011.5	1	0.599	6.38	0.05	12.9	2.5	<15.9	5.3
SDSS 171748.43 + 594820.6	1	0.763	3.04	0.04	9.7	4.1	<9.6	3.2
SDSS 171818.14 + 584905.2	1	0.634	4.06	0.06	35.0	6.1	28.9	13.9
SST 171106.8 + 590436	2	0.462	3.65	0.06	26.3	4.9	<19.5	6.5
SST 171147.4 + 585839	2	0.800	4.84	0.07	18.8	5.7	31.9	13.7
SST 171324.1 + 585549	2	0.609	4.94	0.07	16.1	1.5	33.8	10.7
SST 171831.7 + 595317	2	0.700	8.27	0.04	27.1	4.4	31.2	12.8
SST 172123.1 + 601214	2	0.325	13.34	0.07	12.0	6.2	<9.3	3.1
SST 172458.3 + 591545	2	0.494	2.60	0.06	24.6	4.9	38.1	15.0

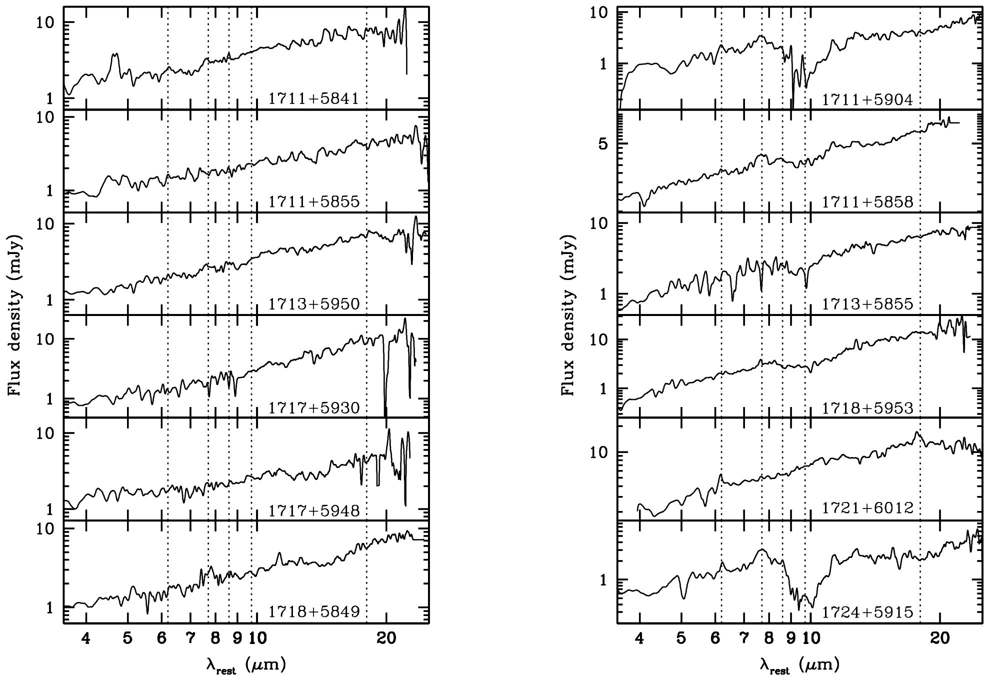

Fig. 5.1.— *Left*: IRS spectra for our type-1 quasar sample. *Right*: IRS spectra for our type-2 quasar sample. The spectra have been smoothed with a gaussian with sigma of five pixels. Vertical dotted lines indicate the wavelengths for 6.2, 7.7 and 8.6 μm PAH features, and 9.7 and 18 μm silicate features.

5.4. Analysis and Results

5.4.1. Modeling

We modeled the SEDs of our sample from the optical out to the far-IR. We used available SDSS and 2MASS photometry, IRAC bands 1 and 2 (3.6 μm and 4.5 μm, respectively) photometry (Lacy et al. 2005) and our *Spitzer* IRS mid-IR spectra and MIPS photometry. This additional photometry used in the modeling procedure is presented in Table 5.2. The modeling code is described by Sajina et al. (2006). Modifications to the code to enable modeling of the type-2 objects in our sample were briefly described by Lacy et al. (2007). Here we provide a fuller description of the modeling, and the additional modifications required to fit the type-1 objects. The modeling is phenomenological in nature due to the current lack of a good physical understanding of the nature and geometry of the dust emitting regions, particularly in the mid-IR, thus many of the parameters do not have a direct physical interpretation. Nevertheless, we considered the effort worthwhile as it allows an empirical breakdown of the contributions of starlight, hot dust emission from the AGN, and cooler dust emission.

The type-2 SEDs were modeled using the following components. (1) A single stellar population from Bruzual & Charlot (2003) with an age of 5 Gyr to represent the evolved stellar population. (2) A power-law component for the mid-IR emission, with an exponential cutoff at short wavelengths to represent dust sublimation, and a Fermi function cutoff at long wavelengths designed to match the SED shape of the least star-forming object in the sample of type-2s, SST 1721+6012. The functional form used was:

$$L_{\rm AGN} = \frac{L^0_{\rm AGN}\nu^{1-\alpha}e^{h\nu/k_BT_{\rm sub}}}{e^{(\nu-\nu_{\rm hcut})/w}+1} \tag{5.1}$$

where the normalization, $L^0_{\rm AGN}$, power-law index α and $T_{\rm sub}$ (a proxy for the sublimation temperature) are allowed to vary, and $\nu_{\rm hcut}$ and w were fixed at 0.11×10^{14}Hz and 0.017×10^{14}Hz, respectively (h and $k_{\rm B}$ are the Planck and Boltzman constants, respectively). The Galactic Center extinction curve of Chiar & Tielens (2006) was then applied to this continuum to fit any silicate absorption feature. (3) A warm dust component to represent the small grain emission from HII regions, represented by a power-law with fixed high and low frequency cutoffs:

$$L_{\rm SG} = L^0_{\rm SG}\nu^{1-\gamma}e^{-\nu/\nu_{\rm sgl}}e^{-\nu_{\rm sgh}/\nu} \tag{5.2}$$

This component is poorly constrained in most of the fits, so γ was fixed at a typical value of two (*e.g.,* Sajina et al. 2006). The high and low frequency cutoffs, $\nu_{\rm sgl}$ and $\nu_{\rm sgh}$ were set to 0.062×10^{14}Hz and 0.17×10^{14}Hz, respectively. (4) a thermal modified blackbody model for the far-infrared emission:

$$L_{\rm FIR} = \frac{L^0_{\rm FIR}\nu^{3+\beta}}{e^{h\nu/k_{\rm B}T}-1} \tag{5.3}$$

For most objects, we fixed the temperature of this component, T, to 45K, because of the uncertainty in our 160 μm photometry. β was fixed at 1.5. In addition, the PAH model described in Lacy et al. (2007) was added when evidence of PAH emission was seen, and SST 1721+6012 had a silicate emission profile added, whose shape was approximated by that of the extinction curve.

For the type-1 quasars, component (1) was replaced by an SDSS composite quasar spectrum. As the composite of Vanden Berk et al. (2001) suffers from noticeable host galaxy contamination at the long wavelength end, we constructed a new composite by subtracting the continuum from the composite of Vanden Berk et al., and adding the residual emission line composite to a new continuum constructed using line-free SED points from the composite of Richards et al. (2006).

Most type-1 objects also required an extra near-infrared component to match the SEDs. This "very hot" component was modeled as a 1000 K modified blackbody (Eq. 5.3 with $T = 1000$). The physical origin of this component is unclear, but it is most likely due to hot dust close to the sublimation radius (*e.g.,* Netzer et al. 2007). Gallagher et al. (2007) show that the strength of this component correlates with quasar luminosity. We do not find this to be true for our sample, but note that Gallagher et al. (2007) have a much larger sample size spread over a range of luminosities.

The modeling results for the type-1 objects are presented in Fig. 5.2, and the results for the type-2 objects are presented in Fig. 5.3. Several differences between the type-1 sample and the type-2 sample are immediately apparent from the fitting results. The type-1 objects have a strong optical quasar component that can extend significantly into the mid-IR. The 1000 K component is significant in all six type-1s and also contributes to the mid-IR. Three of the six type-1 object SEDs showed no evidence of the warm small grain dust power-law emission. The type-2 object SEDs are dominated in the mid-IR

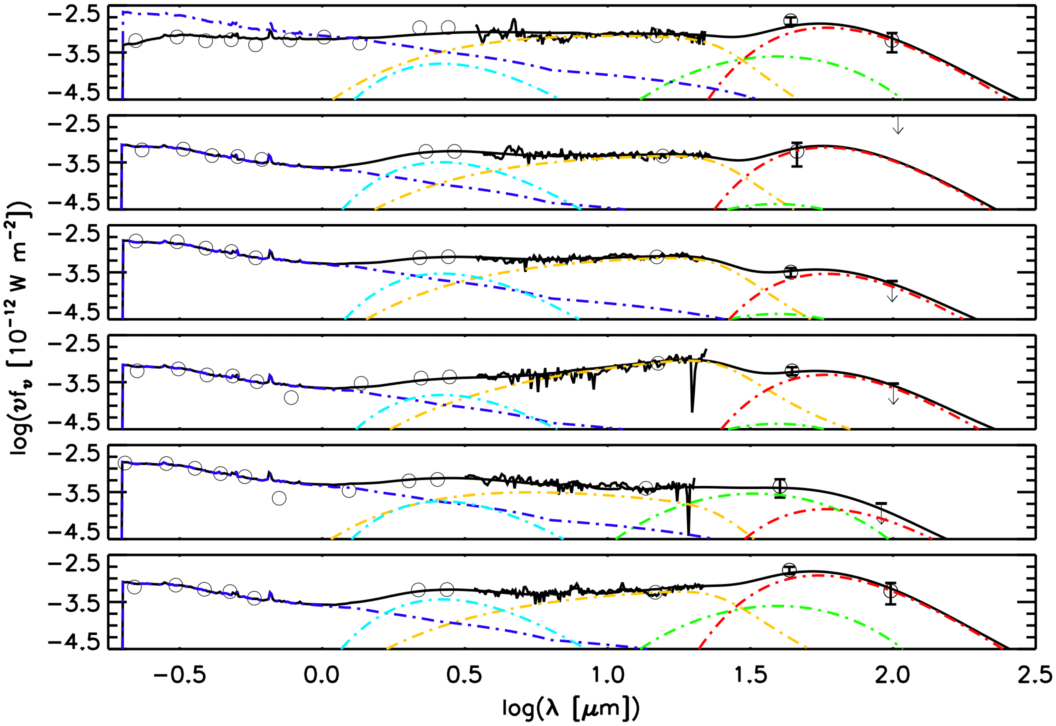

Fig. 5.2.— The type-1 sample. The spectra are presented in their rest frame. From top to bottom are SDSS 1711+5841, 1711+5855, 1713+5950, 1717+5930, 1717+5948, and 1718+5849. The photometry measurements are plotted as circles and the IRS data are plotted as a solid line. We show error bars for the MIPS 70 μm and 160 μm photometry. Error bars on other photometry measurements are smaller than the plotting symbol. The individual components of the model are plotted as dot-dashed lines and the overall fit as the solid black line. The blue line represents the quasar composite component, the cyan line the 1000 K component, the orange line the mid-IR power-law, the green line the warm small grain dust power-law, and the red line the cool 45 K modified blackbody.

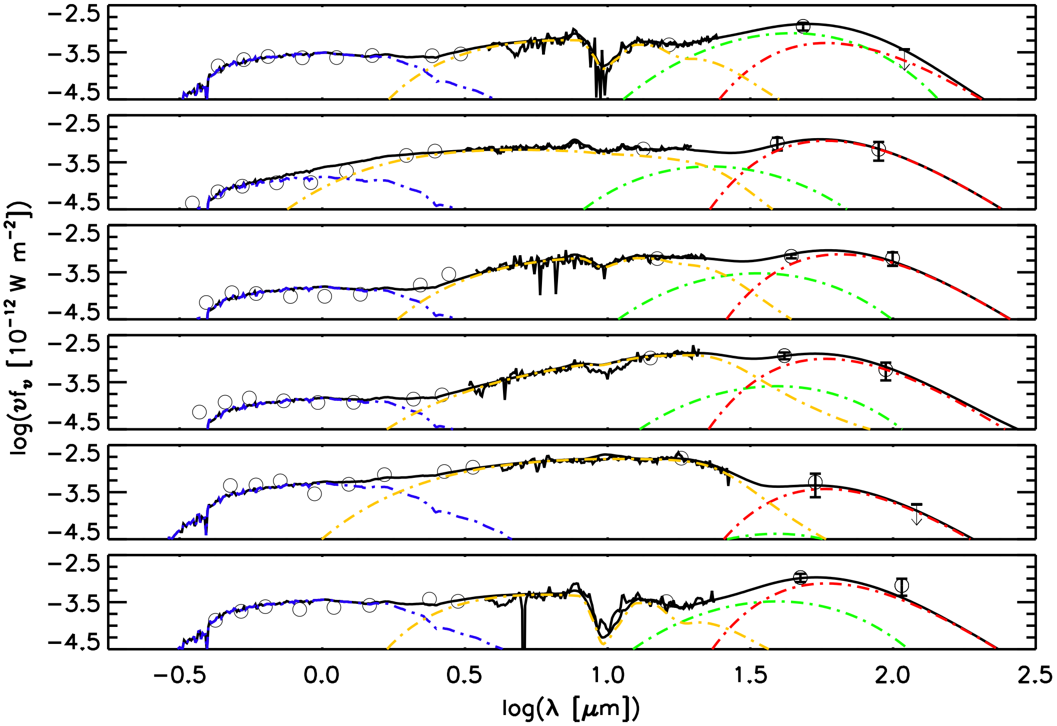

Fig. 5.3.— The type-2 sample. The spectra are presented in their rest frame. From top to bottom are SST 1711+5904, 1711+5858, 1713+5855, 1718+5953, 1721+6012, 1724+5915. The plotted symbols are the same as in Fig. 5.2. The photometry measurements are plotted as circles and the IRS data are plotted as a solid line. We show error bars for the MIPS 70 μm and 160 μm photometry. Error bars on other photometry measurements are smaller than the plotting symbol. The individual components of the model are plotted as dot-dashed lines and the overall fit as the solid black line. The blue line represents the host galaxy stellar component, the orange line the mid-IR power-law, the green line the warm small grain dust power-law, and the red line the cool 45 K modified blackbody.

by hot dust with no contribution from the optical stellar light and no evidence for the 1000 K component. Also present in the mid-IR portion of the type-2 objects is a variety of PAH emission and silicate absorption. Five of the six type-2 objects have significant contributions to the mid and far-IR from the warm small grain dust power-law. SST 1721+6012 was the only type-2 not fit well with this component.

We note that the results of the fitting procedure for the object SST 1724+5915 underestimate both the observed amount of PAH emission and the far-IR emission. This is likely due to the large amount of silicate absorption also present in the spectrum of the object. In particular the 9.7 μm absorption feature can affect the shape of the 7.7 μm PAH feature, making it difficult to fit with an empirical template. We include the data in our subsequent analysis, but note that star formation rates derived from the far-IR emission and the PAH emission likely underestimate the true star formation of this object (see §5.4.2).

We averaged the modeled type-1 SEDs and type-2 SEDs to highlight the differences between the two samples. We first normalized the SED of each target at 24 μm to ensure each object had equal weight. By choosing to normalize at 24 μm we can compare the relative amounts of hot and cool dust in the averaged SEDs. Though at 24 μm, extinction is still present, it is significantly reduced compared to shorter wavelengths. It is clear from Fig. 5.4 that on average type-2 objects show more PAH emission, more silicate absorption and more far-IR emission than type-1 objects. In addition, while the very hot 3 μm bump is clear in the type-1 spectrum, no bump is seen in the type-2 spectrum. We note the caveat that the type-1 and type-2 objects could have equivalent amounts of

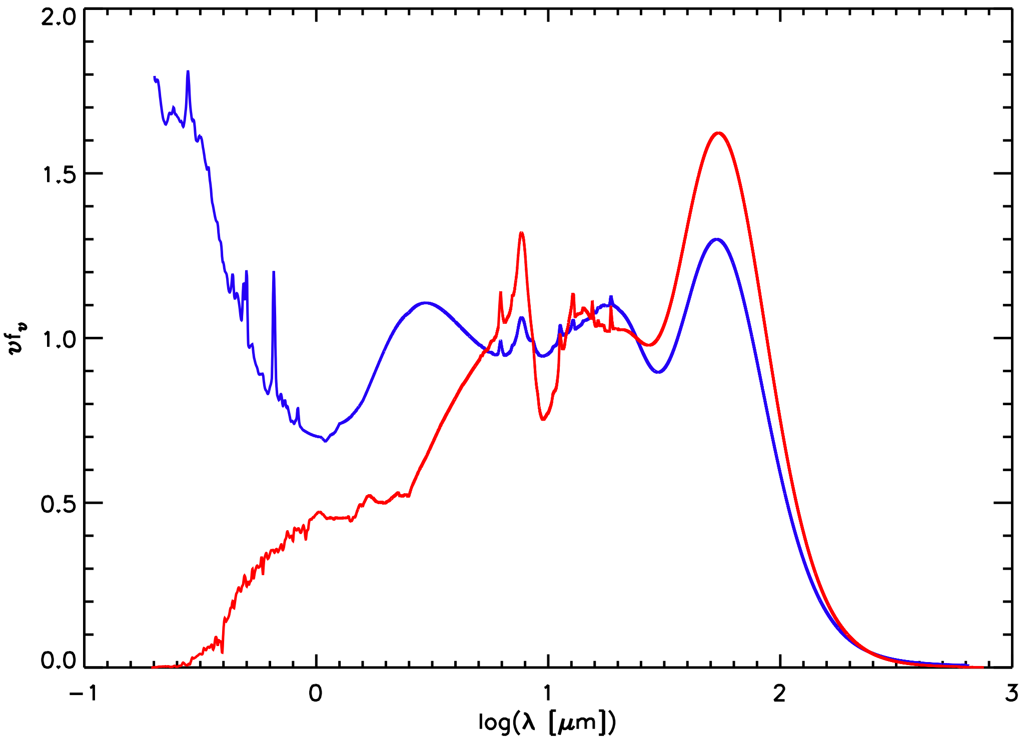

Fig. 5.4.— Averaged modeled SEDs of type-1 (blue) and type-2 (red) quasars. The spectra are normalized at 24 μm. We plot νf_ν to highlight the differences between the two.

PAH emission if that emission were significantly diluted by a strong mid-IR continuum in type-1 objects.

The important question is if these observed differences could arise solely due to orientation effects. In that scenario the optical through mid-IR light is absorbed and re-radiated in the far-IR. To test this, we integrated the optical through far-IR fluxes of the normalized and averaged spectra and found them to be identical. These results are consistent with the orientation hypothesis, though the geometry and distribution of the obscuring dust cannot be proved from this simple test.

Furthermore, under the orientation hypothesis, the dust tori of the type-1 and type-2 quasars should have the same intrinsic luminosities. Our modeling results show that the tori of the type-2 quasars are slightly more luminous than the tori of the type-1 quasars, though the difference is not statistically significant. This may be a result of our mid-IR selection technique, as those wavelengths are still somewhat affected by extinction. In the next section we examine the PAH emission and the star formation contribution to the far-IR emission to gain more insight into whether the far-IR emission is different between the two objects.

5.4.2. Star Formation Rates

We characterized and compared the star formation rates of the quasar host galaxies by comparing the PAH emission with the far-IR luminosity of our sample (Fig. 5.5). We measured the far-IR luminosity from only the modeled warm (Eq. 5.2) and cold dust (Eq. 5.3) contributions to the SEDs (hereafter L'_{FIR}), excluding dust heated by the

Table 5.2: Additional Photometry Used in Modeling Procedure

Target	u	g	r	i	z	J	H	K	$S_{3.6}$	$S_{4.5}$
SDSS 171117.66 + 584123.8	19.23	18.70	18.61	18.33	18.37	17.04	16.10	15.63	1.26	1.61
SDSS 171126.94 + 585544.2	19.27	18.86	18.94	18.75	18.70	···	···	···	0.64	0.81
SDSS 171334.03 + 595028.3	18.24	17.95	18.04	17.98	18.14	···	···	···	0.76	1.02
SDSS 171736.91 + 593011.5	19.36	18.85	18.92	18.72	18.82	18.53	···	16.19	0.46	0.61
SDSS 171748.43 + 594820.6	18.42	18.06	18.07	18.14	18.09	18.04	···	16.05	0.65	0.90
SDSS 171818.14 + 584905.2	19.17	18.70	18.70	18.57	18.70	···	···	···	0.68	0.87
SST 171106.8 + 590436	22.30	21.52	20.07	19.51	19.15	18.0	17.2	16.3	0.32	0.44
SST 171147.4 + 585839	22.94	22.30	21.61	20.80	20.31	18.8	18.0	16.6	0.52	0.82
SST 171324.1 + 585549	22.82	21.83	20.95	20.21	20.06	19.0	18.2	17.3	0.20	0.43
SST 171831.7 + 595317	22.93	21.91	20.93	20.18	19.78	18.7	18.0	17.2	0.16	0.26
SST 172123.1 + 601214	21.69	20.28	18.99	18.74	18.33	17.8	16.5	15.2	1.03	1.60
SST 172458.3 + 591545	21.94	21.69	20.31	19.61	19.17	18.1	17.2	16.3	0.43	0.49

Notes: Additional photometry for the modeling procedure was retrieved from NASA Extragalactic Database (NED). SDSS u, g, r, i, and z magnitudes are listed in the AB system (Oke 1990). The u and g photometry were not used in the fitting of the type-2 targets. 2MASS J, H and K_s magnitudes are presented in Vega system. IRAC bands 1 and 2 (3.6 μm and 4.5 μm) are listed in mJy.

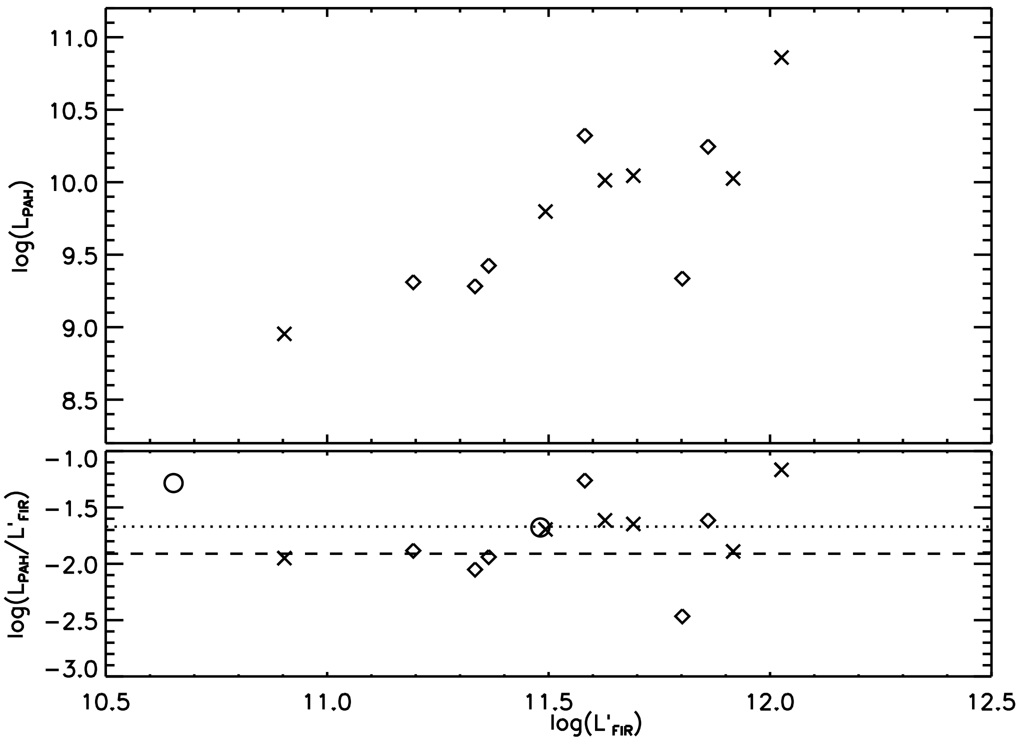

Fig. 5.5.— *Top*: Integrated PAH luminosity as measured from our scaled template is plotted against far-IR luminosity. *Bottom*: Relative amount of PAH emission compared to the far-IR dust emission. In both plots, L'_{FIR} was measured from the warm and cold far-IR components of the model only. L_{PAH} and L'_{FIR} are in $L_{\odot}$ units. Type-1 quasars are plotted as diamonds, and type-2 quasars are plotted as Xs. The starburst galaxies NGC 7714 and NGC 2623 are plotted as circles (Marshall et al. 2007). The dashed line indicates the median ratio of the type-1 objects of our sample, and the dotted line indicates the median ratio of the type-2 objects.

central AGN and emitting in the mid-IR. This definition of L'_{FIR} specifically excludes dust heated by the AGN while still measuring dust heated in star forming regions, even if the two emit at similar or overlapping wavelengths. This is in contrast to using a defined wavelength cutoff, which would measure dust heated by either source. However, it is still important to note that the far-IR emitting dust could also be heated by the AGN if that dust were at large enough distances from the nucleus. It is important to consider this potential AGN contribution to the far-IR emission when calculating SFRs.

The PAH emission is an independent indicator of the star formation activity in the host galaxy. UV and X-ray emission from the AGN destroy PAHs (Voit 1992), but soft UV emission from star formation excites PAHs into emission. In Fig. 5.5 we find a correlation between PAH emission and far-IR emission similar to previous works (*e.g.,* Schweitzer et al. 2006; Menéndez-Delmestre et al. 2009). We also normalized the PAH emission to the far-IR emission, so we can compare the relative contribution of star formation to the far-IR emission. We measured the PAH luminosities by integrating our scaled templates, including the full profiles of each individual PAH feature in the template. This is different from many previous works (*e.g.,* Schweitzer et al. 2006; Menéndez-Delmestre et al. 2009), where only individual PAH features are measured, and definite wavelength cutoffs are applied. We find that the quasars as a whole have a fairly constant ratio across a range of far-IR luminosities. The median L_{PAH}/L'_{FIR} ratio for the type-1 objects of our sample is 0.012, and the median for the type-2 objects is 0.021. We note that the difference between the type-1 objects and type-2 objects is not significant considering the scatter in the sample. The median of our overall sample is 0.017. In comparison, Marshall et al. (2007) measure PAH luminosity using a similar method to ours and find that the starburst galaxies NGC 7714 and NGC 2623 have L_{PAH}/L_{FIR} ratios of 0.052 and 0.021, respectively. We cannot draw strong conclusions based on measurements of two objects, and note that many objects of our sample have ratios consistent with these objects. However, the average L_{PAH}/L_{FIR} from Marshall *et al.* is 0.037, higher than the median value of our sample. If taken at face value, these numbers indicate that some of the cool far-IR emitting dust is heated by AGN emission instead of stellar emission.

In Table 5.3 we present the integrated mid- to far-IR emission (8−1000 μm, hereafter L_{IR}). We find that nearly all of our targets have $\log(L_{IR}/L_{\odot}) \geq 11.75$. SST 1721+6012 is the only object with $\log(L_{IR}/L_{\odot}) \leq 11.75$. We also list the star formation rates (SFR) of our sample in Table 5.3. We calculated SFRs in two different ways. First, we converted the integrated warm and cold dust components of our model into SFRs using the Kennicutt (1998) calibration for starburst galaxies:

$$SFR\ [M_{\odot}\ yr^{-1}] = 4.5 \times 10^{-44} L'_{FIR}\ [erg\ s^{-1}] \tag{5.4}$$

Although our objects have IR luminosities similar to those of ULIRGs, their SFRs are lower than those of typical ULIRGs. This is because some of the IR luminosity of our objects is due to AGN-heated dust, and we explicitly exclude this component when calculating SFRs. The SFRs of our sample are instead typical of LIRGs, which can range from 20 − 200 $M_{\odot}$ yr^{-1} (*e.g.,* Sanders et al. 2003). We find that the type-2 objects show higher SFRs on average (92 $M_\odot$ yr^{-1}) than the type-1 objects (67 $M_\odot$ yr^{-1}). However, the scatter is large, and the object with the lowest SFR is a type-2, SST 1721+6012. We also independently calculated the SFR from the PAH emission. This can be done by predicting a far-IR luminosity based on the PAH luminosity. We integrated our scaled PAH template to measure the PAH luminosity of each object in our sample. We adopt an average ratio of $L_{PAH}/L_{FIR} \sim 0.037$ based on the results of Marshall et al. (2007). Subsequently, for all objects in our sample except two, the SFR predicted from the PAH luminosity is lower than the SFR predicted by integrating the warm and cold dust components of the far-IR (L'_{FIR}). Again we found that the average type-2 quasar has a higher SFR (87 $M_\odot$ yr^{-1}) than the average type-1 quasar (37 $M_\odot$ yr^{-1}).

5.5. Summary and Discussion

We obtained mid-IR spectra and far-IR photometry for six type-1 and six type-2 mid-IR selected quasars. We modeled the SEDs of our sample from the optical to the far-IR using available SDSS, 2MASS and IRAC photometry, in addition to our IRS spectra and MIPS photometry. We compared the modeled SEDs of the quasars and calculated SFRs based on PAH and far-IR emission. Our main results are:

(1) The type-1 quasar mid-IR spectra show a featureless continuum with significant 3 μm emission. The full optical through far-IR SEDs are typically fit well with an optical quasar component, a 1000 K modified blackbody, a mid-IR power-law ($\sim 3-30\mu$m), and

Table 5.3: Luminosities and Star Formation Rates

Target	$\log(L_{IR}/L_\odot)^1$	$\log(L_{PAH}/L_\odot)^2$	SFR $[M_\odot\ yr^{-1}]^3$	SFR $[M_\odot\ yr^{-1}]^4$
SDSS 171117.66 + 584123.8	12.25	9.3	109	10
SDSS 171126.94 + 585544.2	11.82	9.4	40	12
SDSS 171334.03 + 595028.3	11.95	9.3	27	10
SDSS 171736.91 + 593011.5	12.05	9.3	37	9
SDSS 171748.43 + 594820.6	12.06	10.3	66	98
SDSS 171818.14 + 584905.2	12.26	10.2	125	82
SST 171106.8 + 590436	11.79	10.0	73	48
SST 171147.4 + 585839	12.46	10.9	183	338
SST 171324.1 + 585549	12.13	10.0	85	52
SST 171831.7 + 595317	12.47	10.0	143	50
SST 172123.1 + 601214	11.48	9.0	14	4
SST 172458.3 + 591545[5]	11.77	9.8	54	29

---

[1] The luminostiy L_{IR} corresponds to the integrated modeled SED from 8-1000 μm.

[2] The PAH luminosity is measured from the integrated profiles of all PAH features in the model.

[3] Star formation rates derived from the sum of the warm and cold dust components of the model only. The SFR was calculated using the Kennicutt (1998) relation.

[4] Star formation rates derived from PAH luminosity using the results of Marshall et al. (2007) to convert from L_{PAH} to L_{FIR} and the Kennicutt (1998) relation.

[5] The fit of SST 1724+5915 underestimates the PAH luminosity and far-IR emission, thus also underestimating the SFRs derived from these quantities.

a cool dust far-IR modified blackbody (45 K). Three of the objects also show evidence of warm small grain dust fit with a power-law ($\sim 25-65\mu$m).

(2) The type-2 quasar mid-IR spectra show a variety of PAH emission and silicate absorption strengths. The full optical through far-IR SEDs are fit well using a stellar population in the optical, a mid-IR power-law ($\sim 3-30\mu$m), varying amounts of a PAH emission template and silicate absorption in the mid-IR, warm small grain power-law emission ($\sim 25-65\mu$m) as well as a cool dust modified blackbody (45 K).

(3) Our averaged and normalized modeled spectra show that type-2 quasars exhibit more far-IR emission than type-1 quasars. The excess is roughly equivalent to the deficit in the optical with respect to the type-1 quasars, which is consistent with the orientation hypothesis. In this scenario the increased far-IR emission arises from obscuring dust that is reradiating absorbed light.

(4) We measured L_{PAH} by integrating our scaled template for each object. We compared the typical L_{PAH} to L'_{FIR} ratio of our sample to that of starburst galaxies that have had L_{PAH} measured in a similar manner as the method we used. Within our sample, we found that the type-2 objects have a larger ratio than the type-1 objects. We note that the difference between the two is not significant. Considering our overall sample, we found that the ratio is smaller than for the starburst galaxies (Marshall et al. 2007). This result suggests some far-IR emitting dust can be warmed by the central AGN rather than by young stars. However, a more direct comparison between AGN and starburst galaxies using larger samples would be needed to further quantify the amount of AGN-heated far-IR emitting dust.

(5) We calculated the SFRs of our sample using two methods. First we integrated the warm small grain and cool modified blackbody emission (excluding all other components) of the modeled SEDs and used the Kennicutt (1998) relation to calculate the SFRs. We also converted the L_{PAH} to L_{FIR} (Marshall et al. 2007) to measure the SFRs based on the PAH emission only. In each case the type-2 objects had higher SFR on average than the type-1 objects. However, the difference is not significant given the scatter.

(6) We integrated our modeled SEDs from $8-1000$ μm and found that seven of the 12 can be considered ULIRGs ($\log(L_{IR}/L_\odot) \geq 12$), while four others have $\log(L_{IR}/L_\odot)$ ≥ 11.75. The sole exception is SST 1721+6012, which has $\log(L_{IR}/L_\odot) = 11.48$. While our sample appears to have IR luminosities similar to ULIRGs, the quasars exhibit SFRs more typical of LIRGs. We found the AGN can heat most of the dust in the mid-IR and even some in the far-IR. Thus measuring SFR in quasars from the full $8-1000$ μm SED overestimates the amount of dust warmed by young stars and the true SFR.

(7) The modeling results suggest that type-1 quasars can have mid-IR fluxes that have significant contributions from the optical power-law and 3 μm bump. This 3 μm component is not required for the type-2 SEDs, and the hot dust most likely originates near the sublimation radius of the AGN. If this component is present in the type-2 quasars, it must be at least partially obscured by cooler dust, either a dusty torus or dust in the host galaxy. Lacy et al. (2007) showed that the host galaxies of the type-2 quasars have a range of inclinations. Therefore, the obscuration of the 3 μm bump, if

it is intrinsically present, should be from material close to the nucleus and independent of galaxy orientation.

While our analysis does not distinguish definitively between orientation and evolution based unification schemes, it does directly address the dust content, ongoing star formation in the host galaxies and the AGN contribution to the far-IR emission. Our results are consistent with the orientation hypothesis, but we cannot rule out an evolutionary connection. The star formation based on PAH measurements is a larger contributor to the far-IR luminosity than the AGN for type-2 objects compared to type-1 objects. This difference is only suggestive due to the scatter of both L_{PAH} and L'_{FIR} in our sample and could arise from intrinsic differences in the bolometric luminosities of the objects. The $\mathrm{L}_{PAH}/\mathrm{L}'_{FIR}$ ratio in both type-1 and type-2 quasars is lower than that of starburst galaxies, suggesting that some emission in the far-IR is from dust heated by the AGN and not star formation. This is an area for continued research, as our analysis was based on few objects.

Chapter 6

Conclusions

The growth of black holes and galaxies is not coincidental. It has been known for some time that black hole mass correlates with the host galaxy properties (Ferrarese & Merritt 2000; Gebhardt et al. 2000; Häring & Rix 2004). This has led to research suggesting that black hole and galaxy growth are coeval. Precisely what mechanism links the BH with the host galaxy is presently unknown. It has been suggested that the scaling relations are a natural result of a hierarchical merging (Jahnke & Macciò 2011; Peng 2007). Alternatively, BH feedback might be important in suppressing star formation in the host galaxy. BH feedback has been invoked to explain both the scaling relations and the local galaxy luminosity function (Croton et al. 2006), suppressing the growth of the highest luminosity galaxies.

We have investigated several kinds of galaxies that could illuminate the relationship between BH and host galaxy. Post-starburst quasars simultaneously shows the features of an active nucleus and a post-starburst stellar population. Post-starburst galaxies that lack an active nucleus could at one point have hosted an AGN, given that the AGN lifetime is ~ 100 Myr while the post-starburst signatures last for ~ 1 Gyr. Red quasars are dust obscured objects that allow us to examine the host galaxy during times when the BH is rapidly accreting. Finally, examining canonical type-1 and type-2 quasars at infrared wavelengths provides an alternative measure of star formation in the host galaxies.

Post-starburst galaxies can be created through a range of galaxy-galaxy interactions, from harassment and interaction with IGM in rich cluster environments to major mergers in the non-cluster field. We have shown that it is possible to distinguish between old and young populations in post-starburst galaxies and to measure their kinematics independently. In the galaxies we measured, the two populations tracked each other reasonably well, indicating that the young population is subject to the same potential and dynamics that the old population is. In one galaxy we performed a detailed investigation of the internal kinematics of the two populations. We found evidence for rotation in both young and old populations, but this was not significant compared to the velocity dispersions.

Post-starburst quasars have signatures of young populations, but additionally have an actively accreting black hole. These types of galaxies provide an interesting laboratory to investigate possible black-hole feedback mechanisms. We have shown that post-starburst galaxies can be used to probe the $\mathrm{M_{BH}} - \sigma_*$ relation in the non-local universe, due to their high host-to-nuclear flux ratios. We found six objects with black hole masses that lay on or above the local $\mathrm{M_{BH}} - \sigma_*$ relation. Whether this is due to evolution in the relation or some other effect is currently unknown. By analyzing the additional objects of our sample we will improve the statistics of the $\mathrm{M_{BH}} - \sigma_*$ relation at higher redshifts.

We found an interesting discrepancy between the BH masses calculated based on the Mg II profiles and those calculated based on the Hα profiles. The Hα based $\mathrm{M_{BH}}$ were systematically larger than the Mg II based $\mathrm{M_{BH}}$. This could be due to differences in BLR geometries.

Red quasars are similar to post-starburst quasars in that they have high host-to-nucleus flux ratios. However, in this case it is due to a nucleus that is obscured by dust. The extinction is not significant enough to completely block the Hα emission line. Because of this unique circumstance, we can measure both $\mathrm{M_{BH}}$ and σ_* in these objects. In the work by Canalizo et al. (2012) we found that red quasars at higher redshift are offset from the local $\mathrm{M_{BH}} - \sigma_*$ relation in a manner consistent with other studies at $z > 0.1$ (*e.g.,* Woo et al. 2008), and consistent with our work on post-starburst quasars. The morphologies of red quasars indicate that many are experiencing ongoing mergers.

High $\mathrm{M_{BH}}$ offsets might be explained if during a merger event black hole growth proceeds galaxy growth. It is possible we have caught these objects, both red quasars and post-starburst quasars, at a stage in their evolution between when black hole accretion has peaked and when star formation has peaked. In a large part this depends on the nature of the parent host galaxies before merging or interaction. Mergers, interactions, or disk instabilities will naturally lead to more star formation if the parent galaxy has a large reservoir of cold gas. “Dry mergers”, on the other hand, will lead to less star formation.

Kauffmann & Heckman (2009) propose that BH growth falls into two regimes based on the distribution of Eddington ratios as a function of black hole mass. The find that BHs hosted by star forming galaxies (as measured from the 4000 Å break) show a lognormal distribution, while those hosted by “red and dead” galaxies show a power law distribution. The star forming galaxies have characteristic mass doubling times (M_*/SFR) on the order of the Hubble time. The BHs in these galaxies have a large reservoir of available cold gas from the host. The growth of the BH is self-regulated through feedback heating of the gas within the sphere of influence. On the other hand, in low SFR galaxies, cold gas is rare and cannot be a constant supply of fuel for the BH. In this regime, BH growth is regulated by the evolution of stars which recycles gas into the ISM. The post-starburst galaxies that we have studied show relatively low Eddington ratios and have relatively young stellar populations present in the bulges. Presumably these BHs would fall into the lognormal distribution found by Kauffmann & Heckman (2009) where BH growth is self-regulated. Galaxies with older populations such as the red quasars and the type-2 quasars (with the possible inclusion of the similarly selected type-1 quasars) would fall into the power-law distribution of Eddington ratios. A natural next step would be to investigate the distribution of gas and dust in both post-starburst and red quasars.

We have also investigated the differences between type-1 and type-2 quasars. We compared the infrared SEDs of a sample of six type-1 with those of six type-2 quasars.

Our results showed that type-2 quasars have an excess of IR emission over the type-1 quasars. This is consistent with unification models that describe type-2 AGN as intrinsically similar to type-1 AGN, but obscured in the optical. The dust obscuration reprocesses the optical light and re-emits in the infrared. Whether the differences are strictly due to an orientation effect from a ring of obscuring dust or if the obscuring dust is more cocoon-like is not clear from our results. The type-2 quasars had marginally higher star formation rates, which would be consistent with an evolutionary unification scheme where type-2 quasars are more closely linked to a merger event that drove both BH growth and star formation in the host. We also found that some of the dust that emits in the IR can be warmed by the AGN. This brings into question star formation rates that are solely derived from IR luminosities.

It is not a stretch to envision a scenario where BH and galaxy growth are both driven by galaxy interactions, mergers, and disk instabilities. However, while some minor mergers or galaxy harassment might not increase the host galaxy mass and velocity dispersion by much, minor interactions could still drive growth in the central BH. Black hole growth only requires that gas and dust loose angular momentum and be funneled to the bottom of the potential. The $\mathrm{M_{BH}} - \sigma_*$ relation could be a natural result of galaxy mergers. The BHs that appear over-massive at higher redshift may do so because minor mergers are fairly common, while major mergers are rare. Thus the BH grows quickly during bursts. Meanwhile the galaxy bulge grows more slowly as it encounters other galaxies or accretes cold gas from the IGM. By $z = 0$, many galaxies have experienced a major merger and become aligned with the $\mathrm{M_{BH}} - \sigma_*$ relation. Those that have not are likely to show later type morphologies (*i.e.,* disks), and there is evidence that disk galaxies do not conform with the $\mathrm{M_{BH}} - \sigma_*$ relation or at least are more scattered about it than early type galaxies.

Overall, we have shown that galaxy mergers are a common mechanism by which both black holes and galaxies grow and evolve. Still unresolved is the question of how significant a role BH feedback plays in halting galaxy growth. In the future, more objects will need to be studied at higher redshift. A promising sample lies in narrow-line Seyfert 1 (NLS1) galaxies, which have broad emission lines between 500 and 2000 km s^{-1}. These moderately broad lines imply BH masses that are smaller than those studied in this dissertation. A study of NLS1s with respect to the $\mathrm{M_{BH}} - \sigma_*$ diagram would resolve an open question regarding whether the offset seen in the non-local universe is result of sample selection or if it is real for a range of $\mathrm{M_{BH}}$.

REFERENCES

Abazajian, K., Adelman-McCarthy, J. K., Agüeros, M. A., et al. 2005, AJ, 129, 1755

Abazajian, K. N., Adelman-McCarthy, J. K., Agüeros, M. A., et al. 2009, ApJS, 182, 543

Adelman-McCarthy, J. K., Agüeros, M. A., Allam, S. S., et al. 2007, ApJS, 172, 634

Aihara, H., Allende Prieto, C., An, D., et al. 2011, ApJS, 193, 29

Antonucci, R. 1993, ARA&A, 31, 473

Antonucci, R. R. J., & Miller, J. S. 1985, ApJ, 297, 621

Baldwin, J. A., Phillips, M. M., & Terlevich, R. 1981, PASP, 93, 5

Balogh, M. L., Miller, C., Nichol, R., Zabludoff, A., & Goto, T. 2005, MNRAS, 360, 587

Barth, A. J., Ho, L. C., & Sargent, W. L. W. 2002, AJ, 124, 2607

—. 2003, ApJ, 583, 134

Beifiori, A., Courteau, S., Corsini, E. M., & Zhu, Y. 2011, ArXiv e-prints

Bekki, K., Couch, W. J., Shioya, Y., & Vazdekis, A. 2005, MNRAS, 359, 949

Bender, R., & Nieto, J.-L. 1990, A&A, 239, 97

Bennert, N., Canalizo, G., Jungwiert, B., et al. 2008, ApJ, 677, 846

Bennert, V. N., Auger, M. W., Treu, T., Woo, J.-H., & Malkan, M. A. 2011, ApJ, 726, 59

Bentz, M. C., Peterson, B. M., Netzer, H., Pogge, R. W., & Vestergaard, M. 2009a, ApJ, 697, 160

Bentz, M. C., Walsh, J. L., Barth, A. J., et al. 2009b, ApJ, 705, 199

—. 2010, ApJ, 716, 993

Blandford, R. D., & McKee, C. F. 1982, ApJ, 255, 419

Blanton, M. R., Schlegel, D. J., Strauss, M. A., et al. 2005, AJ, 129, 2562

Brandl, B. R., Bernard-Salas, J., Spoon, H. W. W., et al. 2006, ApJ, 653, 1129

Brotherton, M., Cales, S., Ganguly, R., et al. 2010, in IAU Symposium, Vol. 267, IAU Symposium, 105–105

Brotherton, M., Paul, C., Ganguly, R., et al. 2012, in preparation

Brotherton, M. S., van Breugel, W., Stanford, S. A., et al. 1999, ApJ, 520, L87

Bruzual, G. 2007, in Astronomical Society of the Pacific Conference Series, Vol. 374, From Stars to Galaxies: Building the Pieces to Build Up the Universe, ed. A. Vallenari, R. Tantalo, L. Portinari, & A. Moretti, 303

Bruzual, G., & Charlot, S. 2003, MNRAS, 344, 1000

Cales, S. L., Brotherton, M. S., Shang, Z., et al. 2011, ApJ, 741, 106

—. 2012, in preparation

Canalizo, G., Bennert, N., Jungwiert, B., et al. 2007, ApJ, 669, 801

Canalizo, G., & Stockton, A. 2001, ApJ, 555, 719

Canalizo, G., Wold, M., Hiner, K. D., Lazarova, M., & Lacy, M. 2012, submitted

Cano-Díaz, M., Maiolino, R., Marconi, A., et al. 2012, A&A, 537, L8

Cardelli, J. A., Clayton, G. C., & Mathis, J. S. 1989, ApJ, 345, 245

Charlot, & Bruzual. 2007

Chiar, J. E., & Tielens, A. G. G. M. 2006, ApJ, 637, 774

Chilingarian, I. V., Melchior, A.-L., & Zolotukhin, I. Y. 2010, MNRAS, 405, 1409

Croom, S. M., Smith, R. J., Boyle, B. J., et al. 2004, MNRAS, 349, 1397

Croton, D. J. 2006, MNRAS, 369, 1808

Croton, D. J., Springel, V., White, S. D. M., et al. 2006, MNRAS, 365, 11

Cutri, R. M., Nelson, B. O., Francis, P. J., & Smith, P. S. 2002, in Astronomical Society of the Pacific Conference Series, Vol. 284, IAU Colloq. 184: AGN Surveys, ed. R. F. Green, E. Y. Khachikian, & D. B. Sanders, 127

Denney, K. D., Peterson, B. M., Dietrich, M., Vestergaard, M., & Bentz, M. C. 2009, ApJ, 692, 246

Desroches, L.-B., Quataert, E., Ma, C.-P., & West, A. A. 2007, MNRAS, 377, 402

Di Matteo, T., Springel, V., & Hernquist, L. 2005, Nature, 433, 604

Dressler, A. 1984, ApJ, 286, 97

Dressler, A., & Gunn, J. E. 1983, ApJ, 270, 7

Dunlop, J. S., McLure, R. J., Kukula, M. J., et al. 2003, MNRAS, 340, 1095

Faber, S. M., & Jackson, R. E. 1976, ApJ, 204, 668

Faber, S. M., Wegner, G., Burstein, D., et al. 1989, ApJS, 69, 763

Fadda, D., Marleau, F. R., Storrie-Lombardi, L. J., et al. 2006, AJ, 131, 2859

Ferrarese, L., & Merritt, D. 2000, ApJ, 539, L9

Fine, S., Croom, S. M., Hopkins, P. F., et al. 2008, MNRAS, 390, 1413

Frayer, D. T., Fadda, D., Yan, L., et al. 2006, AJ, 131, 250

Gallagher, S. C., Richards, G. T., Lacy, M., et al. 2007, ApJ, 661, 30

Garstang, R. H. 1952, ApJ, 115, 506

Gebhardt, K., Bender, R., Bower, G., et al. 2000, ApJ, 539, L13

Glikman, E., Helfand, D. J., White, R. L., et al. 2007, ApJ, 667, 673

Goto, T. 2006, MNRAS, 369, 1765

—. 2007, MNRAS, 381, 187

Graham, A. W., Onken, C. A., Athanassoula, E., & Combes, F. 2011, MNRAS, 412, 2211

Greene, J. E., & Ho, L. C. 2004, ApJ, 610, 722

—. 2005, ApJ, 630, 122

—. 2006, ApJ, 641, 117

Greene, J. E., Peng, C. Y., & Ludwig, R. R. 2010a, ApJ, 709, 937

Greene, J. E., Peng, C. Y., Kim, M., et al. 2010b, ArXiv e-prints

Gültekin, K., Richstone, D. O., Gebhardt, K., et al. 2009, ApJ, 698, 198

Hao, L., Weedman, D. W., Spoon, H. W. W., et al. 2007, ApJ, 655, L77

Häring, N., & Rix, H.-W. 2004, ApJ, 604, L89

Hiner, K. D., & Canalizo, G. 2012, in preparation

Hiner, K. D., Canalizo, G., Brotherton, M., Cales, S., & Wold, M. 2012a, in preparation

Hiner, K. D., Canalizo, G., Lacy, M., et al. 2009, ApJ, 706, 508

Hiner, K. D., Canalizo, G., Wold, M., Brotherton, M., & Cales, S. 2012b, accepted for publication in ApJ

Hopkins, P. F., & Quataert, E. 2010, MNRAS, 407, 1529

Jahnke, K., & Macciò, A. V. 2011, ApJ, 734, 92

Jester, S., Schneider, D. P., Richards, G. T., et al. 2005, AJ, 130, 873

Jorgensen, I., & Franx, M. 1994, ApJ, 433, 553

Jørgensen, I., Franx, M., Hjorth, J., & van Dokkum, P. G. 1999, MNRAS, 308, 833

Kaspi, S., Smith, P. S., Netzer, H., et al. 2000, ApJ, 533, 631

Kauffmann, G., & Heckman, T. M. 2009, MNRAS, 397, 135

Kennicutt, Jr., R. C. 1998, ARA&A, 36, 189

Kormendy, J. 1982, in Saas-Fee Advanced Course 12: Morphology and Dynamics of Galaxies, ed. L. Martinet & M. Mayor, 113–288

Kormendy, J., & Richstone, D. 1995, ARA&A, 33, 581

Kriss, G. 1994, Astronomical Data Analysis Software and Systems, 3, 437

Krist, G., & Hook, R. 2001, Space Telescope Science Institute

Kurk, J. D., Walter, F., Fan, X., et al. 2007, ApJ, 669, 32

Lacy, M., Sajina, A., Petric, A. O., et al. 2007, ApJ, 669, L61

Lacy, M., Storrie-Lombardi, L. J., Sajina, A., et al. 2004, ApJS, 154, 166

Lacy, M., Wilson, G., Masci, F., et al. 2005, ApJS, 161, 41

Lauer, T. R., Tremaine, S., Richstone, D., & Faber, S. M. 2007, ApJ, 670, 249

Lutz, D., Sturm, E., Tacconi, L. J., et al. 2008, ApJ, 684, 853

Magorrian, J., Tremaine, S., Richstone, D., et al. 1998, AJ, 115, 2285

Marble, A. R., Hines, D. C., Schmidt, G. D., et al. 2003, ApJ, 590, 707

Marshall, J. A., Herter, T. L., Armus, L., et al. 2007, ApJ, 670, 129

Massey, P., & Gronwall, C. 1990, ApJ, 358, 344

Massey, P., Strobel, K., Barnes, J. V., & Anderson, E. 1988, ApJ, 328, 315

Matthews, T. A., & Sandage, A. R. 1963, ApJ, 138, 30

McConnell, N. J., Ma, C.-P., Gebhardt, K., et al. 2011a, Nature, 480, 215

McConnell, N. J., Ma, C.-P., Graham, J. R., et al. 2011b, ApJ, 728, 100

McGill, K. L., Woo, J.-H., Treu, T., & Malkan, M. A. 2008, ApJ, 673, 703

McLure, R. J., & Dunlop, J. S. 2002, MNRAS, 331, 795

McLure, R. J., & Jarvis, M. J. 2002, MNRAS, 337, 109

Menéndez-Delmestre, K., Blain, A. W., Smail, I., et al. 2009, ApJ, 699, 667

Netzer, H., Lutz, D., Schweitzer, M., et al. 2007, ApJ, 666, 806

Nigoche-Netro, A., Aguerri, J. A. L., Lagos, P., et al. 2010, A&A, 516, A96

Norton, S. A., Gebhardt, K., Zabludoff, A. I., & Zaritsky, D. 2001, ApJ, 557, 150

Oke, J. B. 1990, AJ, 99, 1621

Oke, J. B., Cohen, J. G., Carr, M., et al. 1995, PASP, 107, 375

Onken, C. A., Ferrarese, L., Merritt, D., et al. 2004, ApJ, 615, 645

Osterbrock, D. E., & Ferland, G. J. 2006, Astrophysics of Gaseous Nebulae and Active Galactic Nuclei (University Science Books)

Peng, C. Y. 2007, ApJ, 671, 1098

Peng, C. Y., Ho, L. C., Impey, C. D., & Rix, H. 2002, AJ, 124, 266

Pracy, M. B., Kuntschner, H., Couch, W. J., et al. 2009, MNRAS, 396, 1349

Press, W. H., Teukolsky, S. A., Vetterling, W. T., & Flannery, B. P. 2007, Numerical Recipes 3rd Edition: The Art of Scientific Computing, 3rd edn. (New York, NY, USA: Cambridge University Press)

Rafiee, A., & Hall, P. B. 2011, ApJS, 194, 42

Richards, G. T., Lacy, M., Storrie-Lombardi, L. J., et al. 2006, ApJS, 166, 470

Robertson, B., Hernquist, L., Cox, T. J., et al. 2006, ApJ, 641, 90

Rockosi, C., Stover, R., Kibrick, R., et al. 2010, in Society of Photo-Optical Instrumentation Engineers (SPIE) Conference Series, Vol. 7735, Society of Photo-Optical Instrumentation Engineers (SPIE) Conference Series

Sajina, A., Scott, D., Dennefeld, M., et al. 2006, MNRAS, 369, 939

Sajina, A., Yan, L., Armus, L., et al. 2007, ApJ, 664, 713

Sandage, A. 1965, ApJ, 141, 1560

Sandage, A., & Wyndham, J. D. 1965, ApJ, 141, 328

Sanders, D. B., Mazzarella, J. M., Kim, D.-C., Surace, J. A., & Soifer, B. T. 2003, AJ, 126, 1607

Sanders, D. B., Soifer, B. T., Elias, J. H., et al. 1988, ApJ, 325, 74

Schlegel, D. J., Finkbeiner, D. P., & Davis, M. 1998, ApJ, 500, 525

Schmidt, M. 1963, Nature, 197, 1040

Schneider, D. P., Fan, X., Hall, P. B., et al. 2003, AJ, 126, 2579

Schweitzer, M., Lutz, D., Sturm, E., et al. 2006, ApJ, 649, 79

Seyfert, C. K. 1943, ApJ, 97, 28

Sigut, T. A. A., & Pradhan, A. K. 2003, ApJS, 145, 15

Spoon, H. W. W., Marshall, J. A., Houck, J. R., et al. 2007, ApJ, 654, L49

Stockton, A. 1982, ApJ, 257, 33

Swinbank, A. M., Balogh, M. L., Bower, R. G., et al. 2012, MNRAS, 420, 672

Toomre, A., & Toomre, J. 1972, ApJ, 178, 623

Tremonti, C. A., Moustakas, J., & Diamond-Stanic, A. M. 2007, ApJ, 663, L77

Urrutia, T., Becker, R. H., White, R. L., et al. 2009, ApJ, 698, 1095

van Dokkum, P. G. 2001, PASP, 113, 1420

van Dokkum, P. G., & Franx, M. 2001, ApJ, 553, 90

Vanden Berk, D. E., Richards, G. T., Bauer, A., et al. 2001, AJ, 122, 549

Vestergaard, M., & Osmer, P. S. 2009, ApJ, 699, 800

Vestergaard, M., & Wilkes, B. J. 2001, ApJS, 134, 1

Vika, M., Driver, S. P., Cameron, E., Kelvin, L., & Robotham, A. 2011, ArXiv e-prints

Voit, G. M. 1992, MNRAS, 258, 841

Walsh, J. L., Minezaki, T., Bentz, M. C., et al. 2009, ApJS, 185, 156

Wold, M., Lacy, M., & Armus, L. 2007, A&A, 470, 531

Wolf, C., Wisotzki, L., Borch, A., et al. 2003, A&A, 408, 499

Woo, J., Treu, T., Malkan, M. A., & Blandford, R. D. 2006, ApJ, 645, 900

—. 2008, ApJ, 681, 925

Woo, J.-H., & Urry, C. M. 2002, ApJ, 579, 530

Woo, J.-H., Treu, T., Barth, A. J., et al. 2010, ApJ, 716, 269

Xiao, T., Barth, A. J., Greene, J. E., et al. 2011, ArXiv e-prints

Yang, Y., Tremonti, C. A., Zabludoff, A. I., & Zaritsky, D. 2006, ApJ, 646, L33

Zabludoff, A. I., Zaritsky, D., Lin, H., et al. 1996, ApJ, 466, 104

Zakamska, N. L., Gómez, L., Strauss, M. A., & Krolik, J. H. 2008, AJ, 136, 1607

Zakamska, N. L., Schmidt, G. D., Smith, P. S., et al. 2005, AJ, 129, 1212

This manuscript was prepared with the AAS LaTeX macros v5.2.

Appendix A

Spectra of post-starburst quasars at $z \sim 0.3$

In September 2011 we observed eight additional post-starburst quasars from the same *HST* sample described by Cales et al. (2011). The data were reduced with the same procedures discussed in chapter 3. Figure A.1 shows the spectra in the rest frame from $2500-5500$ Å. The sample shows a variety of spectral slopes and AGN-to-host flux ratios. Some objects show strong Hβ emission, which will provide additional constraints on the $\mathrm{M_{BH}}$ measurement. At least one object has Hβ in absorption. Mg II is also covered in this spectral range and shows a range of strengths. It does not appear that there are any additional LoBAL objects in this sample.

With these eight additional objects, we will be able to determine if the results described above are consistent for the post-starburst quasar sample. This sample more than doubles the sample described above and will provide stronger statistical constraints on any measured offset from the $\mathrm{M_{BH}} - \sigma_*$, and $\mathrm{M_{BH}}-\mathrm{L_{bulge}}$ relations.

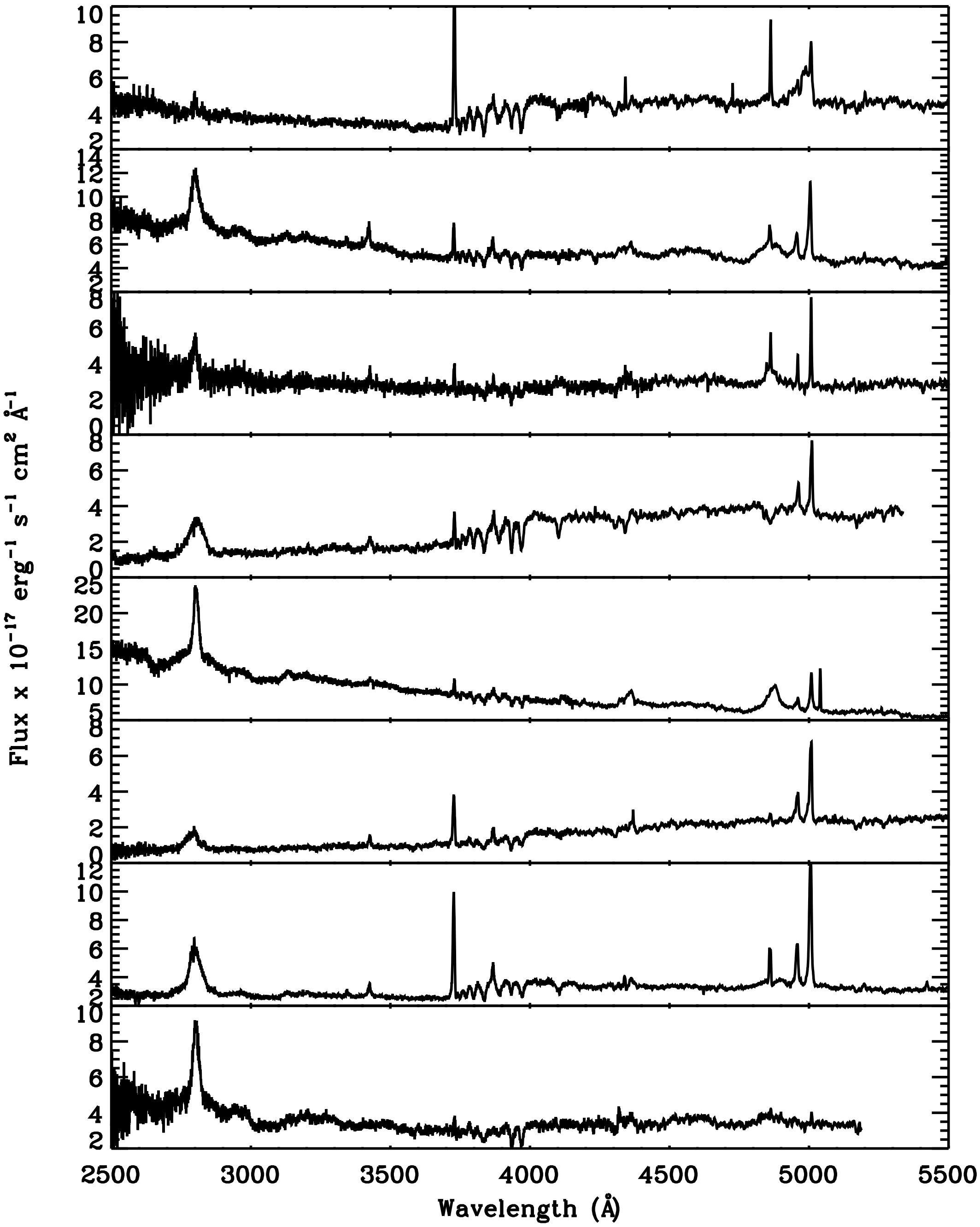

Fig. A.1.— LRIS spectroscopy of additional post-starburst quasars. Objects are plotted in the rest frame. Listed from top to bottom they are SDSS 020258.94 − 002807.5, SDSS 021447.00 − 003250.6, SDSS 040210.90 − 054630.3, SDSS 211343.20 − 075017.6, SDSS 212843.42 + 002435.6, SDSS 231055.50 − 090107.6, SDSS 233430.89 + 140649.8, SDSS 234403.55 + 154214.0

Appendix B

Spectra of red quasars at $z > 0.4$

We obtained spectra of a follow-up sample of red quasars selected from the FIRST-2MASS red quasar catalog (Urrutia et al. 2009), and all have $z > 0.4$. Two objects are near $z \sim 1$. We can perform a similar analysis as we did with the previous low-z sample (Canalizo et al. 2012) in order to measure the $\mathrm{M_{BH}}$ and σ_* values for these systems. This analysis will allow for a unique determination of the evolution of the $\mathrm{M_{BH}} - \sigma_*$ relation. These objects are at the highest redshift for which this analysis has been attempted.

In Fig. B.1 we show the reduced LRIS spectra. The data were obtained during observing runs in May 2010 and September 2010 and reduced with procedures similar to those used in the previous chapters.

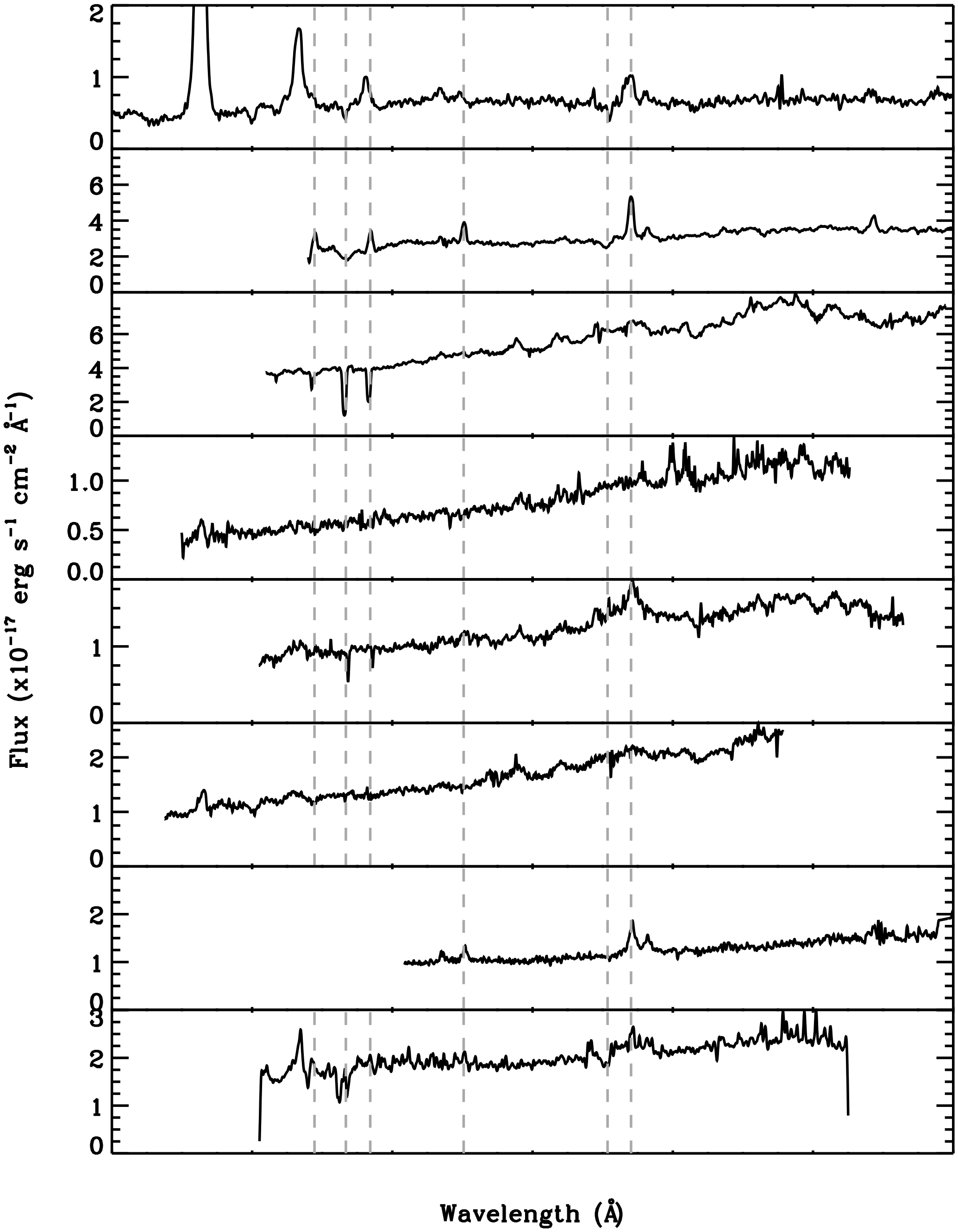

Fig. B.1.— The Ca H+K region for the reddened quasars observed with LRIS during May and September 2010. Objects from top to bottom are: 003659.85 − 011332.3, 161809.72 + 350208.53, 233903.84 − 091221.0, 172027.58 + 615657.63, 14340462 + 580611.41, 125615.29 − 020023.58, 215214.08 − 002832.6, 101230.49 + 282527.15